1990

Flaw reconstruction in NDE using a limited number of x-ray radiographic projections

Richard Miles Wallingford
Iowa State University

Order Number 9110577

Flaw reconstruction in NDE using a limited number of x-ray radiographic projections

Wallingford, Richard Miles, Ph.D.

Iowa State University, 1990

U·M·I
300 N. Zeeb Rd.
Ann Arbor, MI 48106

Flaw reconstruction in NDE using a limited number of x-ray radiographic projections

by

Richard Miles Wallingford

A Dissertation Submitted to the

Graduate Faculty in Partial Fulfillment of the

Requirements for the Degree of

DOCTOR OF PHILOSOPHY

Department: Electrical Engineering and Computer Engineering
Major: Electrical Engineering

Approved:

Signature was redacted for privacy.

In Charge of Major Work

Signature was redacted for privacy.

For the Major Department

Signature was redacted for privacy.

For the Graduate College

Iowa State University
Ames, Iowa
1990

TABLE OF CONTENTS

LIST OF FIGURES

LIST OF TABLES

ACKNOWLEDGEMENTS

The author would like to thank the following people for their assistance during this research: John Basart, Joe Gray, Don Thompson, Hsien-Sen Hung, Noel Cressie, Steve Russell, T.V. Ramabadran. The author also thanks Dave Utrata of the AAR for arranging the test frog radiography and for his continuous interest in this work.

1. INTRODUCTION

Nondestructive evaluation (NDE) is a very broad interdisciplinary field that is primarily concerned with assessing the integrity of a part or device without destroying its functionality. The NDE field uses a wide range of theories from different areas such as electromagnetics, physics and fracture mechanics. In most cases the goal is to inspect the part for defects or flaws that will affect the performance. Because the inspection is nondestructive, it can be used to extend the life of existing devices in use by indicating areas for repair or by certifying them serviceable. One of the most important applications of NDE is commercial aircraft inspection and reliability assessment. The airline companies are mandated by the FAA to inspect critical portions of the aircraft at specified time intervals. Through this procedure, airplanes generally remain safe and their operational lifetime is extended, often well beyond their designed lifetimes. Recently, the field of NDE has become more visible after several aircraft disasters attributed to structural failures either in the air surfaces or engine parts. This has placed pressure on the industries to devote more attention to their NDE activities in terms of better inspection and more inspection. Better inspection can be accomplished in two ways. First, research devoted to improved NDE methods and procedures are yielding more sensitive, accurate and predictable results. This is an ongoing task being addressed at many industrial companies as well

as centers of research in NDE. Second, a relatively new concept called "Life Cycle Engineering" is being initiated to design NDE inspectability into devices at the design stage (Burte and Chimenti 1987). This concept requires the involvement of NDE scientists and engineers in the design process. It is a naturally sound approach given that one of the major difficulties in NDE today is "inspectability". Many devices are not inspectable in certain areas simply because of physical limitations of the NDE technique being used. Sometimes a combination of many NDE techniques will be able to fully inspect a part, but not always. A logical time to consider this problem is at the design stage.

There are seven major areas of inspection in NDE (Halmshaw 1987). These are visual, radiological, ultrasonic, magnetic, electromagnetic, penetrant, acoustic emission, thermographic and holographic.

Visual inspection involves looking at the surface structure of a part for obvious signs of damage or fatigue such as surface cracking, deformations or corrosion.

Radiological inspection uses penetrating radiation (e.g., x-rays, neutrons) to create a projection of the inside of a part onto a suitable detector. Flaws within the part appear as a change in intensity of the detected x-ray beam caused by the variation in material density within the part (Halmshaw 1982).

Ultrasonic inspection utilizes the interaction (propagation or reflection) of acoustic waves with flaws within a part to characterize or detect them. Piezoelectric transducers are generally used to generate and detect the acoustic waves.

Magnetic inspection involves detecting defects within ferromagnetic materials by detecting changes in the magnetic properties of the material where the flaw exists. The changes are detected by the presence of a leakage field produced by the disconti-

nuity in the material where the flaw is located. This field can be detected by clusters of magnetic particles or powder that accumulate around the flaw locale.

Electromagnetic inspection uses eddy current probes to induce eddy currents in the material on the surface and at shallow depths. Flaws are detected as a change of impedance seen by the probe as the electromagnetic coupling between the probe and part changes when the probe nears a crack or other defect.

Penetrant inspection is used for detecting surface defects on a material. A liquid dye is spread over a nonabsorbing part and then is wiped clean. The dye penetrates into the surface defects and is not removed in the cleaning process. The dye, and thus the defects, can then be detected using a developer to make the dye visible. The dyed areas can also be detected using paper brought into contact with the part.

Acoustic emission uses elastic radiation caused by changes of stress within a part to detect the presence of flaws (Wadley et al. 1984). The change in stress is caused by the formation or propagation of defects within the material.

Thermographic inspection utilizes the thermal properties of a material to detect flaws or anomalies. This can be done by applying heat to one side of the object and image the heat diffused through to the other side with some thermal sensor such as an infrared camera. The spatial distribution on the other side at any given time will show inhomogeneities within the material as well as spatial variations in the material diffusivity.

Holographic inspection includes optical, acoustic and neutron modalities. In optical holography, very small deformations of a part will create interference fringes when superimposed with a hologram of a nominal part. In acoustic holography, defects are located and sized by reconstructing a profile of the elastic field intensity

within a part. In neutron holography, a hologram of the part is formed by placing it in a neutron beam with a Fresnel zone plate between the part and the film detector. The plate serves as an encoding device and is a series of concentric circles which alternatively absorb and transmit neutrons (Halmshaw 1987). This hologram can then be used to reconstruct the object in a plane in terms of its neutron absorption characteristic.

Each of these techniques has its advantages and disadvantages over the others depending on the application. For example, in steel castings of railroad switches, the grain structure of the steel alloy is too large to allow the use of ultrasonic inspection, while x-ray inspection works well using a high power radioisotope. In other situations ultrasonic inspection may be preferred over nonmagnification x-ray inspection because of the ability to detect smaller defects. There are many tradeoffs involved in selecting the inspection mode. These tradeoffs include signal-to-noise ratio of potential flaws, spatial resolution limits, physical inspectability limitations, time required for inspection and cost.

The type of inspection addressed in this dissertation uses x-ray radiography. One of the major benefits of radiography is that it can produce a two dimensional image of the inside of the part under test. Images are relatively easy to interpret as there is a direct correspondence between what we see in the radiographic image and what exists inside the part. One of the problems with interpretation, however, is that the depth information about the object is lost in the x-ray image. The x-ray intensity arriving at a detector after passing through an object is determined by the x-ray photon interaction with the object material along the line of sight between the source and and the detector position. There are also problems which complicate the quantitative

interpretation of detector signals (x-ray intensities) including geometric unsharpness, scattering, polychromatic effects and detector response. Geometric unsharpness is caused by the finite extent of the x-ray source. Thus, for any position on an x-ray detector, there is an intensity contribution from all points on the x-ray source. This has the effect of blurring out the projection of features on the detector. Figure 1.1 illustrates the unsharpness caused by a source shaped like a short line segment. Notice the radiation emanating from each end of the source blurs out the edge of the test object.

Microfocus x-ray sources have extremely small sizes (down to 10 μ m) and minimize the effects of geometric unsharpness unless extremely large magnifications are used. Magnification is accomplished by placing the part under test closer to the x-ray source where its features diverge to larger proportions on the x-ray detector. The magnification value is given by

$$m = \frac{D}{x}, \tag{1.1}$$

where D is the distance separating the x-ray source and detector, and x is the distance between the object and the source.

Scattered radiation is the radiation reaching the detector that has changed direction and energy after interacting with the material or other structures near the detector. If the scattered photons reach the detector, they cause an image degradation because they have not necessarily interacted with the material along the path from the source to the detector position of interest. Not all photons are scattered, however, and it is the fraction that are scattered that reduces the photon flux from the incident photon beam to contribute to an effective absorption of x-ray energy. Scattering is a random event that is very difficult to model or simulate except through

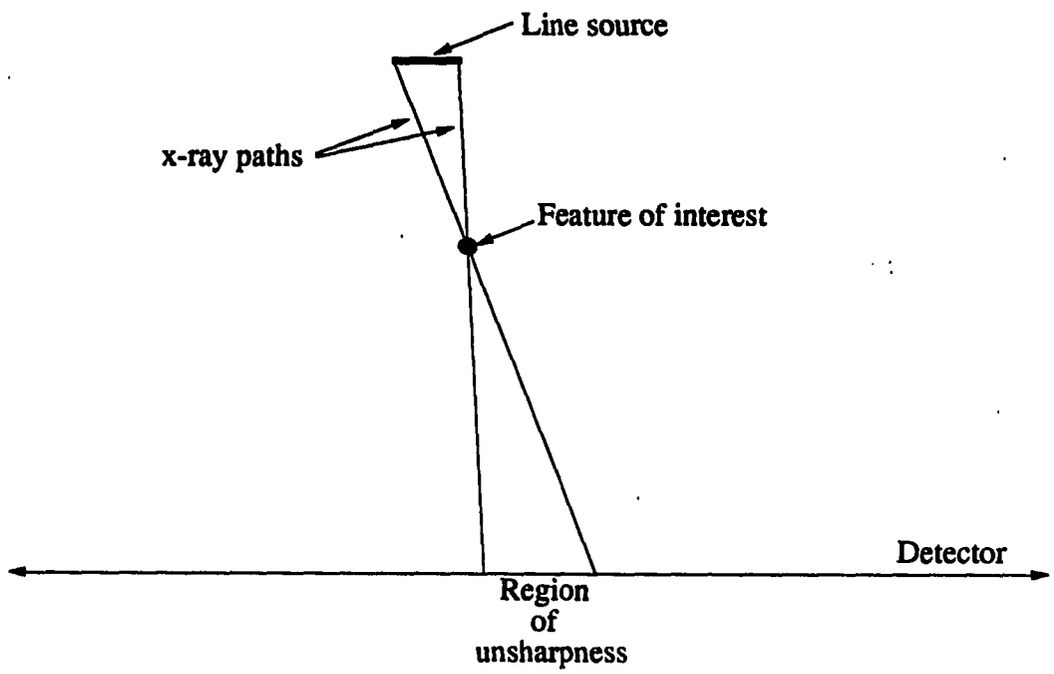

Figure 1.1: Illustration of geometric unsharpness cause by a line source

Monte-Carlo procedures. There are experimental techniques, however, that can minimize the contribution of scattering (Halmshaw 1982). Another major contributor to the absorption of the x-ray energy is photoelectric absorption. Photoelectric absorption occurs when the incoming x-ray photon is absorbed by an atom which resulting in the emission of an electron from the shell of the atom. This type of absorption is only significant for materials of low atomic number and for x-ray energies less than 100 keV.

The polychromatic nature of the x-ray radiation also complicates the quantitative interpretation of x-ray intensities at the detector. All x-ray machines generate a spectrum of x-ray energies which is broadband. These energies represent the characteristic radiation energies associated with the target material in the x-ray tube as well as Bremsstrahlung generated by the deceleration of electrons upon hitting the target. This broadband radiation spectrum causes difficulty because the absorption characteristics of all materials are energy dependent. In addition, the intensity of the generated radiation varies with energy.

Finally, all signals, or x-ray intensities must pass through a detector response function. In the case of x-ray film, models exist that relate the x-ray flux and the exposure time to optical film density, depending on certain physical film properties. Other detectors include scintillation detectors which count photons in a pencil beam and intensifying tubes which convert the x-ray intensity to light on a phosphor plane. The spatial distribution of light can then be digitized by a television camera and a digitizing board so that quantitative information about the image can be obtained. These detectors have an inherent efficiency which is also energy dependent. With scintillation detectors, the x-ray intensity or flux can be directly measured through

photon counts, but with intensifying tubes the relation between x-ray intensity and phosphor light intensity (as well as the digitized output from the television camera) is very complicated and calibration curves are used to emperically deduce it (Bernardi 1991).

We must be aware of the factors above which influence the image formation process as well as the x-ray physics to quantitatively interpret results and to understand the limitations of radiographic inspection.

The limitations of x-ray radiography create a problem with inspectability and flaw detectability. One of these limitations is the thickness and type of material under test. In many situations, it is impossible for the radiation to penetrate through certain materials. Examples of these materials are thick steel castings or materials of high atomic number in which x-rays from a microfocus source ($\leq$ 200 keV energy) cannot penetrate. Another limitation occurs when variations of material thickness create a situation in which part of the image is optimally exposed while other parts are underexposed or overexposed. Figure 1.2 illustrates a part shape in which the geometry would cause sub-optimal exposure over some portion of a film detector.

A related limitation is the dynamic range associated with the detector for any one choice of x-ray voltage and current. For film, the low end of the range is limited by a background optical density, called fog, and the high end is limited by the number of activated silver halide grains in the film emulsion. When all of the grains have been activated, any increase in exposure does not affect the film optical density. To utilize the full dynamic range of film can be difficult. That is, when creating a optimal exposure at areas of thin material, the rest of the part having thicker material can cause underexposure in which no x-rays pass through. Conversely, if an optimal

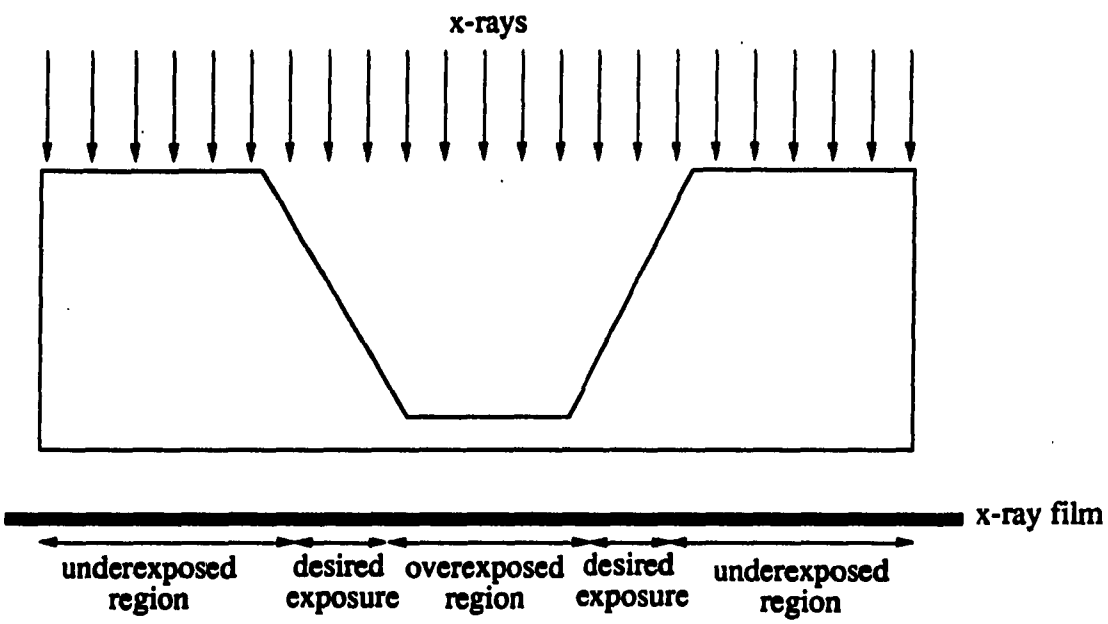

Figure 1.2: Illustration of part geometry causing underexposure and overexposure

exposure is set up for a region of thick material, those regions of thin material will be overexposed and the film will be saturated. Scintillation detectors effectively have an infinite dynamic range. The reason for this is they can continue to count photons indefinitely. Thus, sufficiently high x-ray voltage and current are used to create a high signal to noise ratio in the thick regions and the comparatively high x-ray intensity in the thin regions can be measured simply as a higher number of photon counts.

Other limitations include resolution and sensitivity of the detector. These limitations can be overcome by a variety of techniques such as re-orienting the part under test, taking several exposures at different energy levels, changing the beam properties, and using different types of x-ray detectors. There are applications, however, in which the limitations are very difficult to overcome. All of these limitations play an important role in quantitative flaw measurement. In order to critically assess the integrity of a part, we often need to know the sizes of the flaws as well as their locations. The limitations of inspectability create a major problem for this type of work.

There are two basic approaches to quantitative flaw measurement in x-ray inspection. The first approach involves the reconstruction of the complete structure as well as the material composition of the part under test. This generally involves the determination of all internal and external material boundaries and the spatial distribution of the material x-ray attenuation coefficient. In this manner, material deformations as well as internal flaws can be detected by changes in the reconstructed attenuation coefficient distribution.

The most common way of performing reconstruction is through computed to-

mography (CT). Computed tomography is a technique used for reconstructing cross sections of the x-ray attenuation coefficient from multiple projections around the object (Kak and Slaney 1988). CT reconstruction is based on the Radon transform (Deans 1983) and the central slice theorem. The central slice theorem states that the 1-D Fourier transform of the parallel projection of an object is equal to a slice of the 2-D Fourier transform of the object. This is illustrated pictorially in Fig. 1.3. The parallel projection is obtained from parallel x-rays along the line detector having orientation θ. The object in the spatial domain is a 2-D slice of the spatial x-ray attenuation function of the object.

The spatial attenuation coefficient function is reconstructed by building up points in the frequency domain from projections at many angles followed by an inverse 2-D Fourier transform. Different sections of the object can then be reconstructed and stacked to reconstruct the full 3-D spatial attenuation coefficient function. Obviously this requires an enormous amount of data since many projections are required for each cross section to guarantee complete sampling of the object. Good sampling requires adequate detector resolution as well as a small step size of θ. In industrial CT systems, resolution down to 0.1 mm can be obtained for parallel beam scans and 0.05 mm in magnification (cone-beam or fan-beam) scans (Feldcamp et al. 1988).

There is a large body of literature on CT in both the medical and NDE fields in which alternative reconstruction approaches are presented for various acquisition geometries. These include Algebraic reconstruction in which the object is represented by a discrete matrix of attenuation coefficient values and a system of algebraic equations is solved to determine the values (Andersen 1989); fan-beam reconstruction where the x-ray beam spreads out like a fan from a point source (Peng and Stark

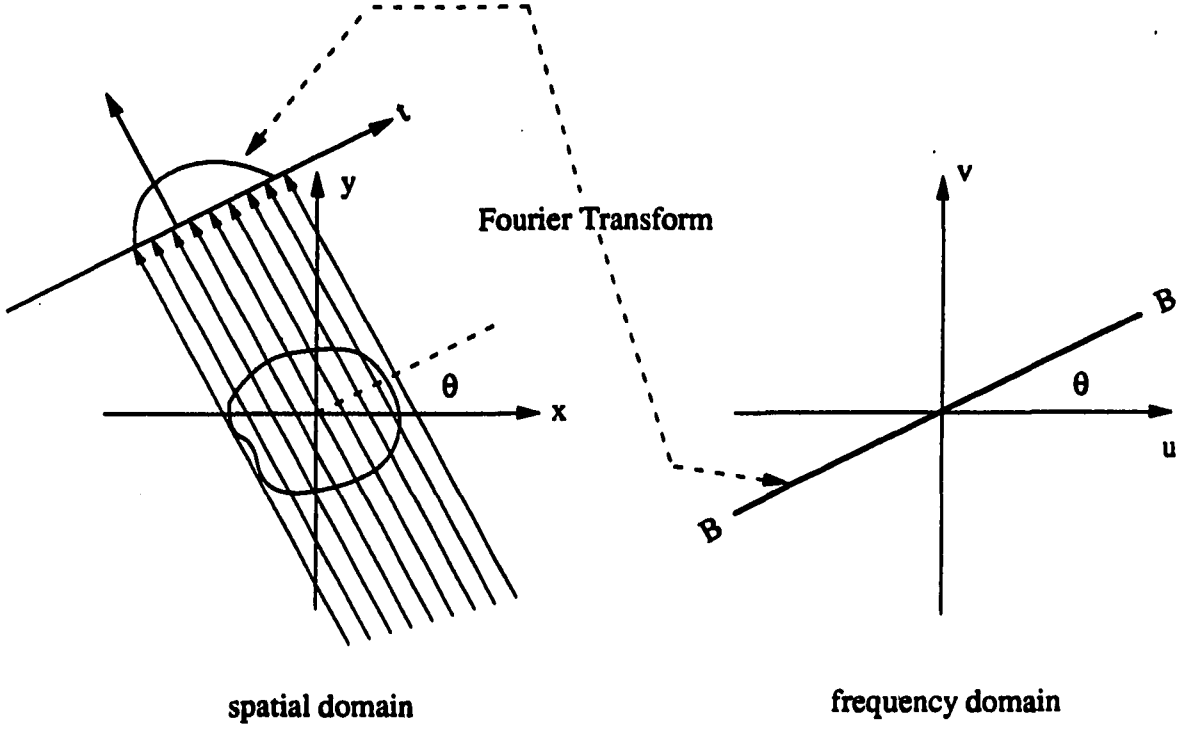

Figure 1.3: Central slice used in CT reconstruction (after Kak and Slaney 1988)

1987); and cone beam reconstruction in which the 3-D attenuation coefficient function is reconstructed directly from angular scans of a cone beam x-ray source (Nalcioglu and Cho 1978; Denton et al. 1979). In a cone beam scan, the entire 2-D projection of the 3-D object is used in the reconstruction as opposed to the 1-D projection of a 2-D slice.

In standard CT reconstruction the object must be inspectable from all angles. As mentioned previously this is often not possible due to geometric considerations. In some cases the object under test is too large or awkward to be used in a CT reconstruction scheme. This results in an incomplete sampling of the frequency domain and the introduction of unwanted artifacts when performing the reconstruction. There are many techniques available which attempt to estimate the missing data or minimize the artifacts in the reconstructed image. The more notable techniques are cited in Chapter 3. There are also situations in which only a few (two or three) projections are available and no amount of estimation to correct for the missing data is sufficient to warrant an attempt at CT reconstruction.

In industrial CT there are other problems associated with obtaining quantitative information about the part under inspection. The problems are similar to those discussed earlier in generic radiography. They include energy dependent attentuation characteristics of materials, broadband x-ray energy spectrum, x-ray beam hardening, scattering, and equipment stability (Vannier and Ellingson 1988). Beam hardening refers to the change in the energy spectrum of the x-ray beam as it passes through an object. Beam hardening artifacts can be reduced by techniques that linearize the attenuation vs. thickness curve (Kak and Slaney 1988) or by dual energy measurement techniques (Vannier and Ellingson 1988). The problems of energy dependent

attenuation process and broadband spectrum have been addressed by McCullough et al. (1974, 1975) who introduced the concept of effective energy (Kak and Slaney 1988). Effective energy is the monochromatic energy that will attenuate the same amount as the broadband energy measured by the CT scanner.

The second approach to quantitative flaw measurement is modeling. In this approach, a geometric model is assumed for the flaw of interest and the flaw is is described by the model parameters rather than the true flaw distribution. The model parameters are estimated by fitting the analytical projection of the model to the measured projections of the flaw. The model can be a geometric figure such as an ellipsoid, box, polygon, or piecewise linear curve. In these cases, the model parameters are the geometric properties defining the figure (e.g., axes lengths, side lengths, centroid location). This approach has several advantages. First, the number of projections required to estimate the model parameters is very small compared to CT. The reason for this is the amount of information being computed is much less. A related advantage is the reduction in computation time required to compute the model parameters. Another advantage is the simplified data acquisition requirements. This is due to the fact that only a few projections are required to perform the model parameter estimation and in many cases, the object under test requires inspection from one side only.

This type of flaw measurement is not a new idea as flaw models such as EDM (electrical discharge machining) notches have been used in eddy current inspection (Sabbagh and Sabbagh 1983, 1984) and ellipsoids have been used for volumetric flaw sizing in ultrasonic inspection (Schmerr et al. 1988). However, there has not been much work in model-based flaw reconstruction using x-ray radiography. One

approach has been to assume a convex hull model for a flaw distribution and to reconstruct the convex hull using an iterative CT approach at restricted angles (Tam 1989). Another approach has been to reconstruct polyhedra shapes from three views (Hung et al. 1989). This approach uses edge and corner information from three views to reconstruct a polyhedron model of an object. It is specifically geared towards photographic scene-type images, but could be applied to x-ray images.

In this project, a technique, specifically geared towards NDE x-ray radiography has been developed that uses a piecewise linear curve model for crack-like flaws and an ellipsoidal model for volumetric flaws (Wallingford and Basart 1988, 1989a, 1989b, 1990). In the piecewise linear curve model, the endpoints of the linear segments that model the crack are reconstructed from two or more stereographic or rotational projections. In the ellipsoidal model, the model parameters are also reconstructed from at least two stereographic projections. This dissertation deals with the theoretical development of the flaw models, the reconstruction algorithms and the error analysis of the results. In addition, experimental results are shown to demonstrate the practicality of this approach. The major purpose behind this work is to develop and implement practical methods of obtaining reliable estimates of flaw sizes, shapes and locations in materials where the inspectability is a limitation.

The dissertation is divided into four sections. Chapter 2 deals with the reconstruction of the locations of flaw feature points as well as crack-like flaws using a stereo-radiographic approach. We use the term reconstruction henceforth to mean the estimation or determination of parameters of the flaw model. Chapter 3 presents the theory of two-dimensional volumetric flaw parameter estimation using an elliptical flaw model. This chapter is used as a precursor to Chapter 4, which deals with

three-dimensional ellipsoidal flaw parameter estimation. Chapter 5 is devoted to addressing practical issues of measurement data acquisition as well as experimental results of the model-based volumetric flaw parameter estimation.

2. STEREOGRAPHIC RECONSTRUCTION

2.1 Background

Reconstruction from stereographic projections is not a new idea. It has been in use for a long time to reconstruct depth and location of objects from two viewpoints of the same object. The basic idea behind stereographic reconstruction is to use the disparity between the same objects in stereo images to extract the 3-D depth information about the object. For images produced by shifting the x-ray source. The reconstruction involves geometric triangulation and is illustrated in Fig. 2.1. There is a large body of literature on stereographic reconstruction for many different applications. Among these applications are robot vision (Pong et al. 1989), scene analysis, photogrammetry (Day and Muller 1989), nondestructive evaluation and medicine (Stern and Lewis 1970; Oden et al. 1958). In most of this literature the reconstruction is based on camera views of opaque objects and scenes. With this type of reconstruction, there is a uniqueness assumption that states for any feature point, there is a unique disparity value between the two stereo projections (Grimson 1981).

There is also a broad field of study, called *stereology*, which is the study of three dimensional structure from two-dimensional images. Much of the work in this field is devoted to determining sizes, shapes, numbers and orientations of objects from their

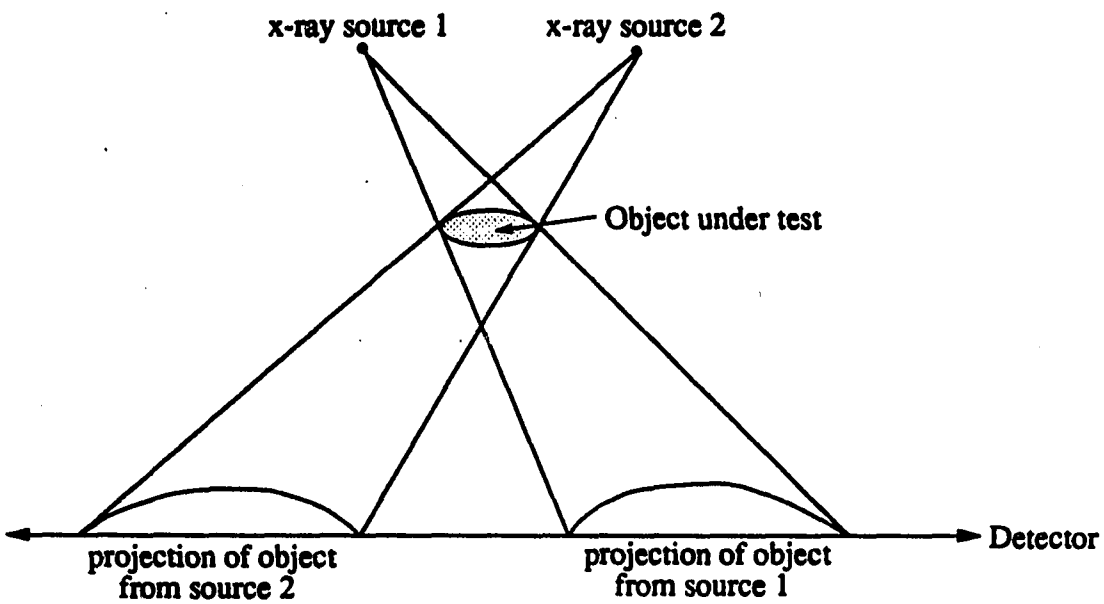

Figure 2.1: Illustration of stereographic projection with shifted source

two dimensional images (Elias and Hyde 1983). Most of the work, however, assumes the images have been obtained by slicing through the test material so that the image represents a true two-dimensional version of the object (Russ 1986). Other image formats include the viewing of discrete particulate matter that has been dispersed on a flat substrate and projections of flat sections of objects as viewed in a microscope. All of these formats are distinctly different from that obtained from an x-ray projection. This is because the intensity at any point in the image from an x-ray projection is influenced by all features in the material along the ray path back to the x-ray source. Stereology concepts can be useful, however in computing properties of volumetric flaws as will be shown in Chapter 5.

A major issue in stereoradiographic reconstruction is solving the problem of identifying the same features between the different projections. This is known as the correspondence problem. The correspondence problem has been addressed by many researchers in the field of machine and computer vision to perform automatic locating of objects. Many of these techniques will be discussed in a later section. The following section assumes that the correspondence problem is solved and presents the derivation of the reconstruction equations for point features or piecewise linear features.

2.2 Stereographic Reconstruction Equations

The reconstruction of the 3-D location of a feature from stereographic x-ray views can be accomplished through a linear shift of the object under test. Often times, this is a convenient method as the sample can be placed on an automatic positioner and translated while the x-ray source and detector system remain fixed. The derivation of the reconstruction equations presented here uses the shifted sample

scheme with a microfocus x-ray source (point source). It is a simple matter, however, to reformulate the problem for a shifted source scheme when that type of arrangement is being used. The shifting process allows the coordinates of the features of interest to be uniquely reconstructed. Multiple shifts can also be incorporated to obtain least-squares solutions for the feature locations.

Figure 2.2 illustrates the geometry used for the reconstruction of a crack like flaw. In this case, the sample under test is shown as the shaded box on the left with a crack like feature inside being approximated by a single linear segment. The objective is to reconstruct the endpoints of the linear segment in 3-D from two projections of the sample. Even though the simulated crack shown has zero thickness, it is assumed that a real crack-like flaw in the material will have sufficient thickness to create a signal on the detector. The minimum detectable thickness depends on the type of detector being used. For highly sensitive film, it is approximately 2% of the total thickness of material being inspected (Nondestructive Testing Handbook 1985).

We label the endpoints of the segment as (x_{c1}, y_{c1}, z_{c1}) and (x_{c2}, y_{c2}, z_{c2}). These endpoints project to the detector coordinates $(x_{11}, y_{11}, 0)$ and $(x_{12}, y_{12}, 0)$, respectively. When the sample is shifted by amount x_T in the x direction the new segment endpoints become $(x_{c1} + x_T, y_{c1}, z_{c1})$ and $(x_{c2} + x_T, y_{c2}, z_{c2})$. These endpoints project to the detector coordinates $(x_{21}, y_{21}, 0)$ and $(x_{22}, y_{22}, 0)$, respectively. The lines connecting the x-ray source to the segment endpoints can be described by parameterized vector equations. The generic form of these equations is given by

$$\mathbf{V} = \mathbf{V}_i + t(\mathbf{V}_f - \mathbf{V}_i), \tag{2.1}$$

where $\mathbf{V}_i$ is the vector from the origin to an initial point on the line to be described,

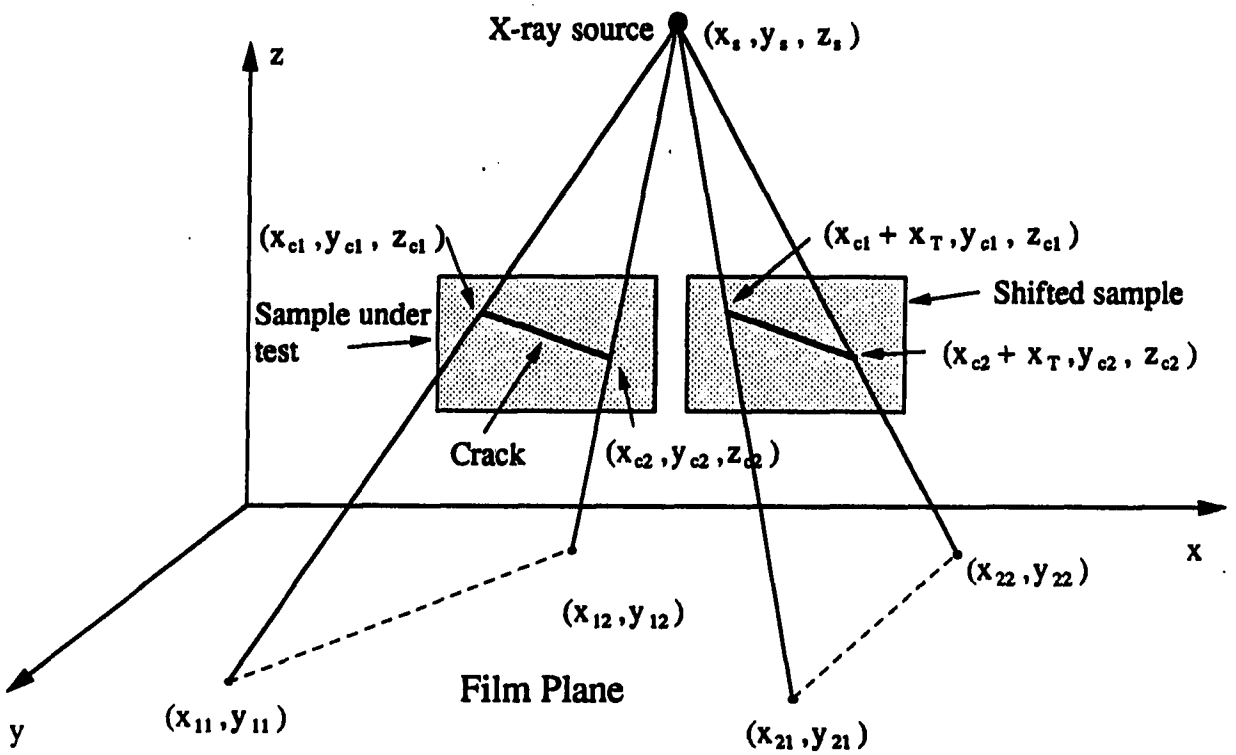

Figure 2.2: Geometry for crack reconstruction (shifted sample)

and $\mathbf{V}_f$ is the vector from the origin to a final point on the same line. The parameter, t is a scalar that varies between zero and one as the vector moves from the initial point to the final point along the line. For the x-ray line through the first endpoint of the unshifted sample, we write

$$\mathbf{V}_i = x_{11}\hat{i} + y_{12}\hat{j} + 0\hat{k} \tag{2.2}$$

$$\mathbf{V}_f = x_s\hat{i} + y_s\hat{j} + z_s\hat{k} \tag{2.3}$$

where $\hat{i}$, $\hat{j}$, $\hat{k}$ are the unit vectors in the x, y and z directions, respectively. Thus for both endpoints of the shifted and unshifted segment, we have the following four vector equations:

$$\mathbf{V}_{11} = x_{11}\hat{i} + y_{11}\hat{j} + t_1[(x_s - x_{11})\hat{i} + (y_s - y_{11})\hat{j} + z_s\hat{k}] \tag{2.4}$$

$$\mathbf{V}_{12} = x_{12}\hat{i} + y_{12}\hat{j} + t_2[(x_s - x_{12})\hat{i} + (y_s - y_{12})\hat{j} + z_s\hat{k}] \tag{2.5}$$

$$\mathbf{V}_{21} = x_{21}\hat{i} + y_{21}\hat{j} + t_3[(x_s - x_{21})\hat{i} + (y_s - y_{21})\hat{j} + z_s\hat{k}] \tag{2.6}$$

$$\mathbf{V}_{22} = x_{22}\hat{i} + y_{22}\hat{j} + t_4[(x_s - x_{22})\hat{i} + (y_s - y_{22})\hat{j} + z_s\hat{k}]. \tag{2.7}$$

We constrain these equations to be the vectors to the segment endpoints. Thus,

$$\mathbf{V}_{11} = x_{c1}\hat{i} + y_{c1}\hat{j} + z_{c1}\hat{k} \tag{2.8}$$

$$\mathbf{V}_{12} = x_{c2}\hat{i} + y_{c2}\hat{j} + z_{c2}\hat{k} \tag{2.9}$$

$$\mathbf{V}_{21} = (x_{c1} + x_T)\hat{i} + y_{c1}\hat{j} + z_{c1}\hat{k} \tag{2.10}$$

$$\mathbf{V}_{22} = (x_{c2} + x_T)\hat{i} + y_{c2}\hat{j} + z_{c2}\hat{k}. \tag{2.11}$$

Combining Eqs. (2.4)-(2.7) and Eqs. (2.8)-(2.11), we have

$$x_{c1}\hat{i} + y_{c1}\hat{j} + z_{c1}\hat{k} = x_{11}\hat{i} + y_{11}\hat{k} + \tag{2.12}$$

$$t_1((x_s - x_{11})\hat{i} + (y_s - y_{11})\hat{j} + z_s\hat{k})$$

$$x_{c2}\hat{i} + y_{c2}\hat{j} + z_{c2}\hat{k} = x_{12}\hat{i} + y_{12}\hat{j} + \tag{2.13}$$
$$t_2((x_s - x_{12})\hat{i} + (y_s - y_{12})\hat{j} + z_s\hat{k})$$

$$(x_{c1} + x_T)\hat{i} + y_{c1}\hat{j} + z_{c1}\hat{k} = x_{21}\hat{i} + y_{21}\hat{j} + \tag{2.14}$$
$$t_3((x_s - x_{21})\hat{i} + (y_s - y_{21})\hat{j} + z_s\hat{k})$$

$$(x_{c2} + x_T)\hat{i} + y_{c2}\hat{j} + z_{c2}\hat{k} = x_{22}\hat{i} + y_{22}\hat{j} + \tag{2.15}$$
$$t_4((x_s - x_{22})\hat{i} + (y_s - y_{22})\hat{j} + z_s\hat{k}).$$

Equations (2.12)-(2.15) yield the following 12 scalar equations:

$$x_{c1} = x_{11} + t_1(x_s - x_{11}) \tag{2.16}$$

$$y_{c1} = y_{11} + t_1(y_s - y_{11}) \tag{2.17}$$

$$z_{c1} = t_1 z_s, \tag{2.18}$$

$$x_{c2} = x_{12} + t_2(x_s - x_{12}) \tag{2.19}$$

$$y_{c2} = y_{12} + t_2(y_s - y_{12}) \tag{2.20}$$

$$z_{c2} = t_2 z_s, \tag{2.21}$$

$$x_{c1} + x_T = x_{21} + t_3(x_s - x_{21}) \tag{2.22}$$

$$y_{c1} = y_{21} + t_3(y_s - y_{21}) \tag{2.23}$$

$$z_{c1} = t_3 z_s, \tag{2.24}$$

and

$$x_{c2} + x_T = x_{22} + t_4(x_s - x_{22}) \tag{2.25}$$

$$y_{c2} = y_{22} + t_4(y_s - y_{22}) \tag{2.26}$$

$$z_{c2} = t_4 z_s. \tag{2.27}$$

From Eqs. (2.18) and (2.24), and Eqs. (2.21) and (2.27), we see that $t_1 = t_3$ and $t_2 = t_4$. We can easily solve for these parameters by subtracting Eq. (2.22) from Eq. (2.16) and Eq. (2.25) from Eq. (2.19). This yields the equations

$$x_T = (x_{21} - x_{11}) + t_1(x_{11} - x_{21})$$

$$x_T = (x_{22} - x_{12}) + t_2(x_{12} - x_{22}).$$

Solving for t_1 and t_2 we get

$$t_1 = \frac{(x_T + x_{11} - x_{21})}{(x_{11} - x_{21})} \tag{2.28}$$

$$t_2 = \frac{(x_T + x_{12} - x_{22})}{(x_{12} - x_{22})}. \tag{2.29}$$

The segment endpoints are computed by substitution of Eqs. (2.28) and (2.29) into Eqs. (2.16)-(2.21). We have,

$$x_{c1} = x_{11} + \frac{(x_T + x_{11} - x_{21})(x_s - x_{11})}{(x_{11} - x_{21})} \tag{2.30}$$

$$y_{c1} = y_{11} + \frac{(x_T + x_{11} - x_{21})(y_s - y_{11})}{(x_{11} - x_{21})} \tag{2.31}$$

$$z_{c1} = \frac{z_s(x_T + x_{11} - x_{21})}{(x_{11} - x_{21})} \tag{2.32}$$

$$x_{c2} = x_{12} + \frac{(x_T + x_{12} - x_{22})(x_s - x_{12})}{(x_{12} - x_{22})} \tag{2.33}$$

$$y_{c2} = y_{12} + \frac{x_T + x_{12} - x_{22})(y_s - y_{12})}{(x_{12} - x_{22})} \tag{2.34}$$

$$z_{c2} = \frac{z_s(x_T + x_{12} - x_{22})}{(x_{12} - x_{22})}. \tag{2.35}$$

These equations can be generalized to compute the coordinates of an arbitrary number of endpoints along a piecewise linear curve. They can also be easily modified to account for a sample shift in the y-direction. The length of the individual crack-like segments is computed as the distance between endpoints and is given by

$$L_s = \sqrt{(x_{c1} - x_{c2})^2 + (y_{c1} - y_{c2})^2 + (z_{c1} - z_{c2})^2}. \tag{2.36}$$

From a computational standpoint, it is useful to implement these equations in a spreadsheet package such as LOTUS 1-2-3 (reference). In this way, the crack coordinates can be easily recomputed by adjusting any of the input parameters such as the projected coordinates of the crack or the x-ray source location. This type of computational environment is also very useful to get an intuitive feel for how the reconstructed coordinates vary as certain parameters are changed. Figure 2.3 shows

CRACK RECONSTRUCTION

OUTPUTS

t1 = 0.5000
t2 = 0.5487

Crack coordinate 1

(xc1	yc1	zc1)
113.5000	14.0000	286.0000

Crack coordinate 2

(xc2	yc2	zc2)
98.5398	-19.4336	313.8407

INPUTS

Film coordinates

(x11,y11)	142.0000	19.0000
(x12,y12)	115.0000	-54.0000
(x21,y21)	40.0000	19.0000
(x22,y22)	2.0000	-54.0000

Sample shift

(dx,dy)	-51.0000	0.0000

Source coordinates

(xs	ys	zs)
85.0000	9.0000	572.0000

Figure 2.3: LOTUS spreadsheet display of a sample crack reconstruction

an example printout of the LOTUS display of a sample reconstruction. Under the heading labeled INPUTS, the film coordinates are entered along with the sample shift distances and x-ray source coordinates. The coordinates of the two crack endpoints and the parameters t_1 and t_2 are displayed under the heading, OUTPUTS. When any input parameter is changed, the values under the OUTPUT heading are immediately recomputed and displayed to reflect the changes.

2.3 Experimental Scenario

In performing an experiment to reconstruct the locations of crack endpoints, the general procedure is to acquire the x-ray data, perform the appropriate measurements, and compute the endpoint coordinates. Acquisition of the x-ray data involves obtaining at least two radiographs of the features of interest using a suitable detector such as film or image intensifier. The two projections are made of the object in a reference or original position and of the object after a known linear shift. Included in these projections must be a suitable landmark or reference marker that is invariant of the object shift. This landmark is used as a coordinate system reference from which to measure the film coordinates.

The measurements required for reconstructing the crack locations are the coordinates of the projected crack endpoints in the reference image, (x_{11}, y_{11}) and (x_{12}, y_{12}) (assuming that only one linear segment is used to approximate the crack), the coordinates of the corresponding points in the image of the shifted object, (x_{21}, y_{21}) and (x_{22}, y_{22}), and the coordinates of the x-ray source, (x_s, y_s, z_s). These measurements are typically made with respect to the reference landmark on the film mentioned earlier. These values are then used in Eqs. (2.30)-(2.35) to compute the coordinates of the crack endpoints in 3-D. Equations for the error bounds on the coordinates using a sensitivity analysis are derived in the next section.

2.4 Reconstruction Error Equations

Errors in the reconstructed coordinates are caused by experimental measurement error, numerical uncertainty and correspondence error. We can establish maximal

bounds on the reconstruction error by estimating maximal bounds on the errors in the input parameters. The maximal reconstruction error is computed through error equations derived by a sensitivity analysis.

For the x_{c1} coordinate, we find the maximal error by first writing it in functional form as

$$x_{c1} = f_{xc1}(x_{11}, x_{21}, x_s; x_T). \tag{2.37}$$

The quantity x_T is treated as a parameter because it can be controlled much more accurately than the other measurements, especially when the sample is shifted using an automatic positioner.

The form of the function found by simplifying Eq. (2.30) is

$$x_{c1} = x_s + \frac{x_T(x_s - x_{11})}{x_{11} - x_{21}}. \tag{2.38}$$

The total differential of this function is

$$df_{xc1} = \frac{\partial f_{xc1}}{\partial x_{11}} dx_{11} + \frac{\partial f_{xc1}}{\partial x_{21}} dx_{21} + \frac{\partial f_{xc1}}{\partial x_s} dx_s \tag{2.39}$$

$$= \frac{x_T(x_{21} - x_s)}{(x_{11} - x_{21})^2} dx_{11} + \frac{x_T(x_{11} - x_s)}{(x_{11} - x_{21})^2} dx_{21} + \left(1 + \frac{x_T}{x_{11} - x_{21}}\right) dx_s. \tag{2.40}$$

An upper bound for the reconstruction error can be written as (Young 1962 , p.7)

$$\Delta x_{c1} \leq \left|\frac{\partial f_{xc1}}{\partial x_{11}}\right| \Delta x_{11} + \left|\frac{\partial f_{xc1}}{\partial x_{21}}\right| \Delta x_{21} + \left|\frac{\partial f_{xc1}}{\partial x_s}\right| \Delta x_s, \qquad (2.41)$$

where Δx_{11}, Δx_{21} and Δx_s are the estimated maximum errors on x_{11}, x_{21}, and x_s, respectively.

Absolute values of the partial derivatives are used to guarantee a maximum bound on the reconstruction error. In practice, we use Eq. (2.41) to determine the maximum variation in the reconstructed coordinated based on estimates of Δx_{11}, Δx_{21} and Δx_s. These quantities are determined from estimated errors or uncertainties encountered in the experimental measurement process. We usually have a good good feel for the maximum source coordinate error as these numbers are usually collected by hand with a tape measure or ruler. Assigning errors to the film coordinate measurements can be more tricky. These errors are caused by imprecision in the measuring device, detector misalignment, geometric unsharpness and correspondence. We can compute a bound on the contribution of geometric unsharpness due to the finite size of the x-ray source from the x-ray source size and the measurement geometry (Halmshaw 1982). We can also estimate bounds on the measurement imprecision and detector misalignment from the process of setting up the experiment. The most difficult contribution to account for is the correspondence error. Because we have no knowledge of the true flaw distribution, it is impossible to obtain exact point correspondence between the projections. In some cases, however, it is possible to examine the flaw features and estimate a value for a maximum correspondence error. The maximum correspondence error is the total distance across the flaw in the case of crossed disparities (see later section on the correspondence problem). Crossed

disparities refers to the apparent crossing of the projected feature points between the two projections. Since this condition is relatively rare, the correspondence error is usually much less. A typical maximum to use in practice when correspondence cannot be made with high confidence is 25% of the distance across the feature.

Equation (2.41) is primarily intended for the scientist to determine how his or her experimental errors affect the reconstructed coordinates. It is very useful to know if the bounds on the reconstruction errors are a significant fraction of the nominal values in establishing a confidence in the method.

The estimated reconstruction error bounds for the other coordinates are computed similarly and are given by

$$\Delta x_{c2} \leq \left|\frac{x_T(x_{22}-x_s)}{(x_{12}-x_{22})^2}\right|\Delta x_{12} + \left|\frac{x_T(x_{12}-x_s)}{(x_{12}-x_{22})^2}\right|\Delta x_{22} + \left|1+\frac{x_T}{(x_{12}-x_{22})}\right|\Delta x_s \tag{2.42}$$

$$\Delta y_{c1} \leq \left|\frac{x_T}{(x_{11}-x_{21})}\right|\Delta y_{11} + \left|\frac{x_T(y_{11}-y_s)}{(x_{11}-x_{21})^2}\right|\Delta x_{11} + \left|\frac{x_T(y_{11}-y_s)}{(x_{11}-x_{21})^2}\right|\Delta x_{21} + \left|1+\frac{x_T}{(x_{11}-x_{21})}\right|\Delta y_s \tag{2.43}$$

$$\Delta y_{c2} \leq \left|\frac{x_T}{(x_{12}-x_{22})}\right|\Delta y_{12} + \left|\frac{x_T(y_{12}-y_s)}{(x_{12}-x_{22})^2}\right|\Delta x_{12} + \left|\frac{x_T(y_{12}-y_s)}{(x_{12}-x_{22})^2}\right|\Delta x_{22} + \left|1+\frac{x_T}{(x_{12}-x_{22})}\right|\Delta y_s \tag{2.44}$$

$$\Delta z_{c1} \leq \left|\frac{x_T x_s}{(x_{11}-x_{21})^2}\right|\Delta x_{11} + \left|\frac{x_T x_s}{(x_{12}-x_{22})^2}\right|\Delta x_{21} + \tag{2.45}$$

$$\left|1+\frac{x_T}{(x_{11}-x_{21})}\right|\Delta z_s$$

$$\Delta z_{c2} \leq \left|\frac{x_T x_s}{(x_{12}-x_{22})^2}\right|\Delta x_{12}+\left|\frac{x_T x_s}{(x_{12}-x_{22})^2}\right|\Delta x_{22}+ \left|1+\frac{x_T}{(x_{12}-x_{22})}\right|\Delta z_s. \tag{2.46}$$

The error bound on the crack length is computed by taking the total differential of Eq. (2.36), yielding

$$dL \leq \left(\frac{1}{2L}\right)\{|2(x_{c1}-x_{c2})|(\Delta x_{c1}+\Delta x_{c2})+|2(y_{c1}-y_{c2})| (\Delta y_{c1}+\Delta y_{c2})+|2(z_{c1}-z_{c2})|(\Delta z_{c1}+\Delta z_{c2})\}. \tag{2.47}$$

The error bound equations have been incorporated into the LOTUS spreadsheet package with the reconstructed coordinates. A printout of the LOTUS display for a sample reconstruction is shown in Fig. 2.4. The inputs to the spreadsheet are the quantities under the *Error Estimates* heading and the *Measurements* heading. From these values, the reconstructed coordinates and the corresponding upper bounds on the errors are computed and displayed under the headings *Reconstructed Coordinates* and *Reconstruction Error*, respectively. Again, this type of computation and display is extremely useful in determining the effects of measurement geometry and experimental errors on the reconstruction error bounds.

Ideally, one would like to perform the experiment many times and estimate the variances of all the measurements. The variance of the reconstructed coordinates could then be estimated using the standard propagation of error formula (Young

Error Estimates			Reconstruction Error	
(dx11,dy11)	0.50	0.50	dxc1	1.2733
(dx12,dy12)	0.50	0.50	dyc1	1.3282
(dx21,dy21)	0.50	0.50	dzc1	3.6340
(dx22,dy22)	0.50	0.50	dxc2	1.3170
dxs	2.00		dyc2	1.5568
dys	2.00		dzc2	3.4149
dzs	2.00		dL	6.1330

Measurements			
(x11,y11)	144.0	20.0	
(x12,y12)	114.0	-50.0	
(x21,y21)	38.0	20.0	
(x22,y22)	2.0	-50.0	
(xs,ys,zs)	85.0	9.0	572.0
dx	-51.0		

Partial Derivatives			
dxc1/dxs	0.51887	dxc2/dxs	0.54464
dxc1/dx11	0.21333	dxc2/dx12	0.33745
dxc1/dx21	0.26780	dxc2/dx22	0.11790
dyc1/dys	0.51887	dyc2/dys	0.54464
dyc1/dy11	0.48113	dyc2/dy12	0.45536
dyc1/dx11	0.04993	dyc2/dx12	0.23988
dyc1/dx21	0.04993	dyc2/dx22	0.23988
dzc1/dzs	0.51887	dzc2/dzs	0.54464
dzc1/dx11	2.59630	dzc2/dx12	2.32557
dzc1/dx21	2.59630	dzc2/dx22	2.32557
dl/dxc1	0.39435		
dl/dyc1	0.83535		
dl/dzc1	0.38297		

Reconstructed Coordinates			
t1	0.5189		
t2	0.5446		
xc1	113.3868	xc2	98.2054
yc1	14.2925	yc2	-17.8661
zc1	296.7925	zc2	311.5357
length	38.4969		

Figure 2.4: LOTUS spreadsheet display including estimated error bounds

1962)

$$\sigma^2_{f_{xc1}} = (\frac{\partial f_{xc1}}{\partial x_{11}})^2\sigma^2_{x_{11}} + (\frac{\partial f_{xc1}}{\partial x_{21}})^2\sigma^2_{x_{21}} + (\frac{\partial f_{xc1}}{\partial x_s})^2\sigma^2_{x_s}. \qquad (2.48)$$

where $\sigma^2_{x_{11}}$, $\sigma^2_{x_{21}}$, and $\sigma^2_{x_s}$ are the sample variances of x_{11}, x_{21} and x_s, respectively. However, it is often very impractical to estimate the variances since it requires performing the same experiment many times.

2.5 Formulation in Terms of a Linear Model

In a previous section we have derived the reconstruction equations from 10 scalar equations with 6 unknown desired parameters and two unknown nuisance parameters. If we write the equations in terms of a linear model, we have an overdetermined system of equations. Because of the random and systematic errors in the measurement variables, there are many possible solutions to this system. A linear model formulation with an overdetermined system that possibly includes extra projections is ideal for treating the reconstructed coordinates as random variables and optimally estimating them. If we assume iid and normally distributed errors in the measurement variables, then the best linear unbiased estimator (BLUE) for the reconstructed coordinates is the least squares estimator (Bain and Engelhardt 1987). If the errors are not correlated or not identically distributed the estimator is not the BLUE, however, the least squares estimator is still a useful and convenient criterion for estimating the coordinates. We formulate the model in the following way.

Let

$$\mathbf{r} = \mathbf{H}\boldsymbol{\theta} + \mathbf{e} \qquad (2.49)$$

where

$$\mathbf{r} = \begin{bmatrix} x_{11} \\ y_{11} \\ 0 \\ x_{12} \\ y_{12} \\ 0 \\ x_{21} - x_T \\ y_{21} \\ x_{22} - x_T \\ y_{22} \\ \vdots \end{bmatrix}, \quad \mathbf{H} = \begin{bmatrix} 1 & 0 & 0 & 0 & 0 & 0 & (x_{11} - x_s) & 0 \\ 0 & 1 & 0 & 0 & 0 & 0 & (y_{11} - y_s) & 0 \\ 0 & 0 & 1 & 0 & 0 & 0 & z_s & 0 \\ 0 & 0 & 0 & 1 & 0 & 0 & 0 & (x_{12} - x_s) \\ 0 & 0 & 0 & 0 & 1 & 0 & 0 & (y_{12} - y_s) \\ 0 & 0 & 0 & 0 & 0 & 1 & 0 & z_s \\ 1 & 0 & 0 & 0 & 0 & 0 & (x_{21} - x_s) & 0 \\ 0 & 1 & 0 & 0 & 0 & 0 & (y_{21} - y_s) & 0 \\ 0 & 0 & 0 & 1 & 0 & 0 & 0 & (x_{22} - x_s) \\ 0 & 0 & 0 & 0 & 1 & 0 & 0 & (y_{22} - y_s) \\ & & & & & \vdots & & \end{bmatrix},$$

$$\theta = \begin{bmatrix} x_{c1} \\ y_{c1} \\ z_{c1} \\ x_{c2} \\ y_{c2} \\ z_{c2} \\ t_1 \\ t_2 \\ \vdots \end{bmatrix},$$

and **e** is the vector of residuals.

Notice that the linear system can be augmented to include measurement data from extra projections. This can be done by repeating the experiment more than

once or by taking projections with different sample shifts. The least-squared error solution to the system is found by minimizing $\|\mathbf{e}\|^2$. We write

$$S = \|\mathbf{e}\|^2 \equiv \|\mathbf{r} - \mathbf{H}\theta\|^2 = (\mathbf{r} - \mathbf{H}\theta)^T(\mathbf{r} - \mathbf{H}\theta) \quad (2.50)$$

$$= \mathbf{r}^T\mathbf{r} + \theta^T\mathbf{H}^T\mathbf{H}\theta - \theta^T\mathbf{H}^T\mathbf{r} - \mathbf{r}^T\mathbf{H}\theta. \quad (2.51)$$

Then setting

$$\frac{\partial S}{\partial \theta} = 0 \quad (2.52)$$

$$= 2(\mathbf{H}^T\mathbf{H})\theta - \mathbf{H}^T\mathbf{r} - \mathbf{H}^T\mathbf{r}, \quad (2.53)$$

the least-squares estimate of θ is

$$\hat{\theta}_{LS} = (\mathbf{H}^T\mathbf{H})^{-1}\mathbf{H}^T\mathbf{r}. \quad (2.54)$$

2.6 Total Least-Squares Solution

In the previous section, the reconstruction equations were formulated in terms of a linear model so that the least-squares estimator could be used to estimate the coordinates. One of the assumptions built into the method of least squares is that there is no error in the explanatory variables. For the 1-D case of a linear model

$$y_i = x_i m + e_i$$

it is assumed that the explanatory variable, x_i has no error when estimating the slope, m. In the linear model of the reconstruction equations, the matrix of explanatory variables, $\mathbf{H}$ consists of measurement variables themselves. For this type of situation, there is a method called *total least squares* (TLS) to minimize the sum of squared errors (Golub and Van Loan 1979, 1980). The method is called *total* because the

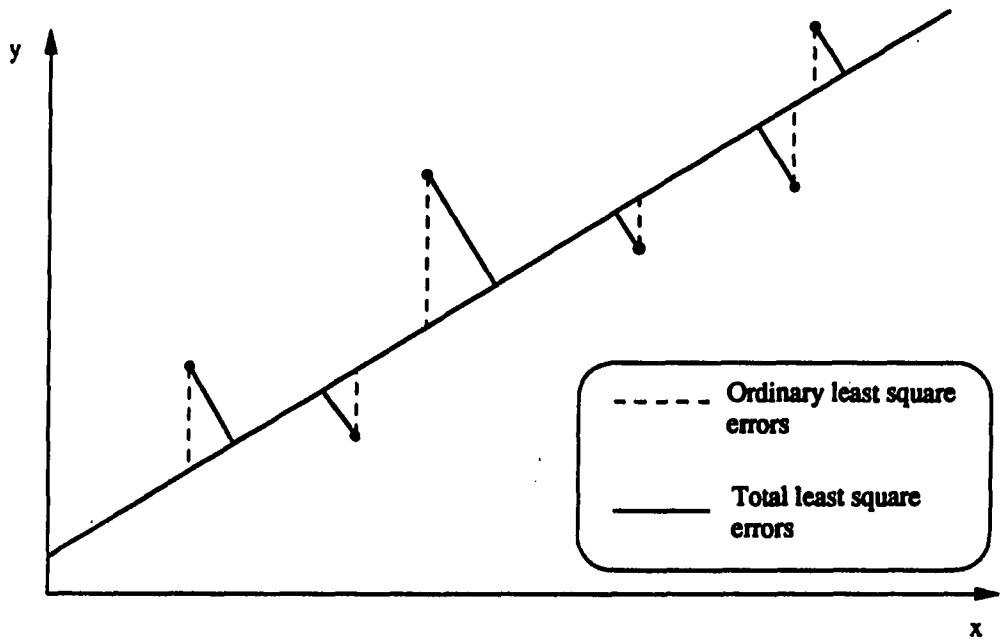

Figure 2.5: Comparison of residual error criteria in total vs. ordinary least squares

residual error is minimized subject to the total error of $\mathbf{r}$ and $\mathbf{H}$. The residual errors for total and ordinary least squares in a 1-D case are illustrated for comparison in Fig. 2.5. In this case, the total least squares estimator minimizes the perpendicular distance from the data point to the fitting line or hypersurface instead of the vertical distance used in ordinary least squares.

We write the linear system for a total least squares scheme as follows:

$$\mathbf{r} + \mathbf{e} = (\mathbf{H} + \mathbf{E})\theta. \tag{2.55}$$

where $\mathbf{e}$ and $\mathbf{E}$ are the errors in $\mathbf{r}$ and $\mathbf{H}$ respectively. The TLS problem can be thought of as perturbing $\mathbf{r}$ and $\mathbf{H}$ by minimal amounts so that $(\mathbf{r} + \mathbf{e})$ can be "predicted" by the columns of $(\mathbf{H}+\mathbf{E})$ (Golub and Van Loan 1980). This is accomplished

by minimizing

$$\|\mathbf{E} \mid \mathbf{e}\|_F$$

where $\|\cdot\|_F$ is the Frobenius norm (Kreyszig 1987, p.824). The total least squares solution is

$$\hat{\theta}_{TLS} = \mathbf{V}(\mathbf{S}^T\mathbf{S} - s_{n+1}^2\mathbf{I})^{-1}\mathbf{S}^T\mathbf{U}^T\mathbf{r}, \tag{2.56}$$

where the matrices **U**, **V** and **S** are obtained from the singular value decomposition (SVD) of **H** (Golub and Van Loan 1989, p. 471),

$$\mathbf{H} = \mathbf{USV}^T.$$

Here, **H** is the $m \times n$ matrix of explanatory variables, **U** is an $m \times m$ orthogonal matrix, **V** is an $n \times n$ orthogonal matrix, and **S** is the $m \times n$ matrix of singular values of **H**. The value s_{n+1}^2 is the minimum singular value of [**H**|**r**] (Golub and Van Loan 1980). Of importance is the fact that the total least squares solution may not exist. The condition for existence is that $s_n < s_{n+1}$, where s_n is the minimum singular value of **H**.

An alternative method to the TLS solution is to use the normal equations (Branham 1989). This yields

$$\hat{\theta}_{TLS} = (\mathbf{H}^T\mathbf{H} - s_{n+1}^2\mathbf{I})^{-1}\mathbf{H}^T\mathbf{r}. \tag{2.57}$$

The value s_{n+1}^2 can be computed either through an SVD of [**H**|**r**] or by an eigenvalue-eigenvector decomposition of $[\mathbf{H}|\mathbf{r}]^T[\mathbf{H}|\mathbf{r}]$ (Branham 1989).

2.7 Experimental Issues

In performing stereographic reconstruction, there are several practical issues that must be considered. These include the experimental setup, the measurement

process, and the choice of x-ray detector. In setting up the experiment, a method must be available to translate the sample under test in a direction parallel to the detector plane. In addition, source location and detector coordinates with respect to some fixed reference point must be determined with as much accuracy as possible. We must also keep in mind that the locations computed from the reconstruction equations are with respect to this fixed reference point. A good way of establishing a reference point is to produce an x-ray shadow of a well defined object such as a thin needle point on the detector in a location that will not interfere with the features of interest. Because the object producing the reference shadow is fixed during the test-object translation, it can be used as the origin of the measurement coordinate system. It is also convenient to define the film plane as the $z = 0$ plane as used in the formulation of the reconstruction equations. This works especially well when using film as a detector. The reason is that two separate films are needed for the stereographic projections. When the film cassette is replaced, it is not necessary to have it perfectly registered in the $z = 0$ plane with the previous film, as the reference point will still have the same location.

Accurate measurement of the source location and guaranteeing sample translation parallel to the detector can be tricky business, especially with some laboratory setups. Often, due to cramped quarters or making the measurements in the field, this is quite difficult. The best approach is to use plumb bobs, levels, tape measures, and angle iron to attempt the most accurate measurements. In laboratory measurements it can be useful to use the laboratory floor as one reference plane. The plumb bob can then be dropped from the x-ray source and the reference point to the floor to measure their height (y-coordinate). The x and z coordinates can be measured easily

off of the floor. Alternatively, one can run a line from the source to the detector plane with a level. A good method for guaranteeing sample translation parallel to the detector plane is to check for equal sample-to-detector distances at several shift amounts.

In setting up the radiography experiment and making the measurements, the best approach is to do it as precisely as possible while estimating the uncertainty for the various measurements. These uncertainties should be used in the reconstruction error equations. The beauty of these equations is that they tell the experimenter how the uncertainties in the experiment affect the results. It is extremely useful to know if the reconstruction results are potentially dominated by measurement errors for a given experimental setup.

Another experimental issue is the choice of x-ray detector. The types of detectors under consideration here are film, real-time image intensifier and scanning scintillation. The factors of importance that are affected by the choice of detector in stereographic reconstruction are spatial resolution and sensitivity. Because we are mainly interested in feature locations in performing the reconstruction, the actual detector signal levels associated with flaw features are not as important as simply the presence of flaw signals and their locations. Detector sensitivity determines whether or not a signal will be present with some perceptible contrast. In this sense, for very faint signals associated with small flaws, or flaws which are small compared to the thickness of material under inspection, the scintillation detector is superior by virtue of its extremely large dynamic range and integration ability. The real-time image intensifier is not nearly as sensitive as either the scintillation or film detectors but it can be used with multiple acquisitions to effectively integrate and reduce noise,

increasing its sensitivity. Film sensitivity can range from good to bad depending on the film speed. A slow speed film with long integration time yields the highest sensitivity (Halmshaw 1982). Good detector spatial resolution is required to obtain accurate measurements of the feature coordinates. The scanning scintillation counter potentially has the highest resolution depending on the mechanics of the scanner. In some cases resolution as fine as 10 microns is possible. Film has the next best resolution followed by the real-time image intensifier. In most cases, however, the image intensifier has adequate resolution to accurately measure the coordinates of the features of interest. The problem with the scanning scintillation counter, is that it takes too much time to build up a 2-D image with sufficient resolution. Thus, either film or image intensifier will usually suffice as an acceptable detector for this type of reconstruction.

2.8 The Correspondence Problem

One of the most important problems in all of stereographic reconstruction is that of correspondence (Weinshall 1990). Correspondence refers to the matching of identical features between the two projections so that the disparity can be used to reconstruct the feature position in 3-D. Disparity is defined as the distance between identical features in the stereo images. Matching corresponding features can be quite difficult in many cases due to presence of similar features, occluding features, nonunique features, undetectable features due to their orientation, and crossed disparities. In radiography, the presence of similar features is quite common as many voids, cracks, and porosity structure look alike. Occluding occurs when a feature blocks the line of sight of another feature to the x-ray source. Figure 2.6 illustrates

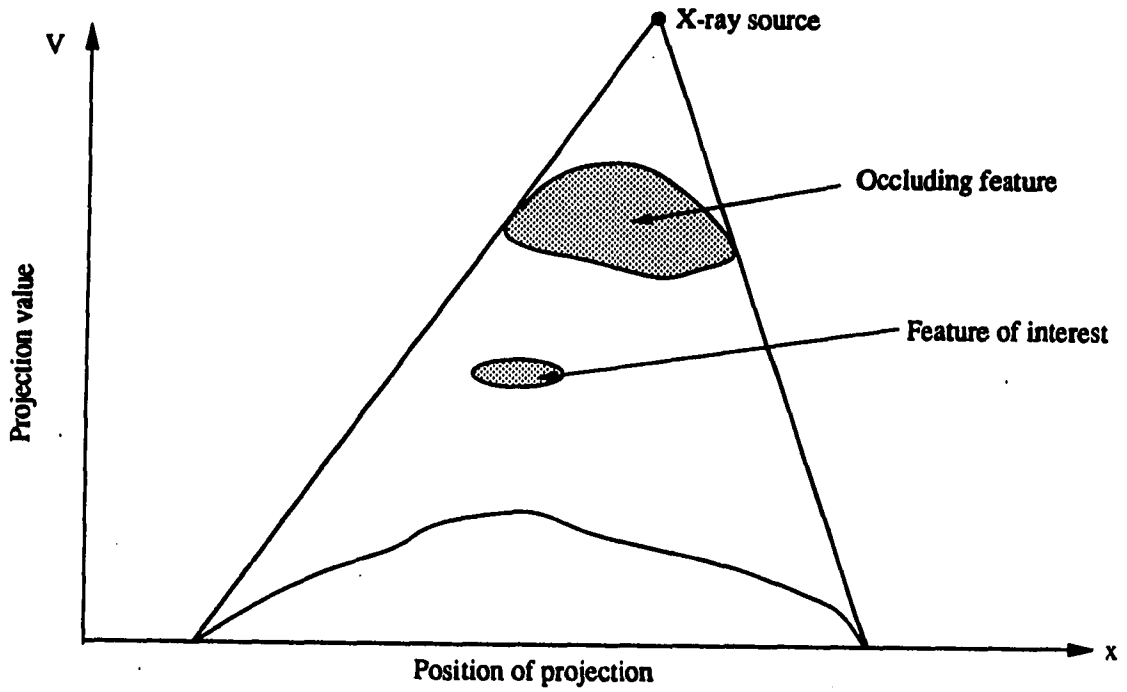

Figure 2.6: Example of occluding feature

an example of an occluding feature. Notice that in this projection feature 1 occludes feature 2. If the source was moved to the left, the two features would be distinct and the projection would move to the right.

Nonunique features refer to the fact that in projection radiography, a feature in the image plane does not necessarily correspond to a unique feature in 3-D space. This happens because each point in the image plane is a result of the integration of all features along the x-ray path connecting the image point to the x-ray source.

Fig. 2.7 shows a very dramatic case of the uniqueness problem. The projection of the unshifted crack-like feature produces a one-to-one correspondence between each point on the detector and each point on the feature, while the projection of points P1 and P2 on the shifted crack-like feature are identical.

In some cases, when the sample under test is shifted, a feature of interest may have changed orientation making it undetectable due to a small x-ray path length within the feature. When the feature becomes undetectable in the shifted image, identification of corresponding points is impossible. This is a potential problem with the detection of extremely thin cracks. When the crack is perpendicular to the path of the x-ray, it may be undetectable, however, it may be perfectly detectable when it is oriented with some non-perpendicular angle.

Crossed disparities refers to the situation in which the order of the corresponding features from left to right becomes reversed when the object under test is shifted. Figure 2.8 illustrates this situation for a crack like flaw. Notice that the ordering of the projections of P1 and P2 have reversed after a shift of the crack-like feature.

The problems with correspondence discussed above indicate that it is difficult to come up with any general strategy for matching all points in stereographic x-ray projections. Almost all literature on the subject of correspondence addresses the problem from a computer vision standpoint where correspondence matching is to be performed automatically. Some of these techniques (Grimson 1981, Marr and Poggio 1979, Aloimonos and Hervé 1990) make certain assumptions about the scene to eliminate some of the problems discussed above. Marr and Poggio (1979) attempt to understand the human early visual system to design appropriate matching strategies. Aloimonos and Hervé (1990) make the assumption that all points to be reconstructed

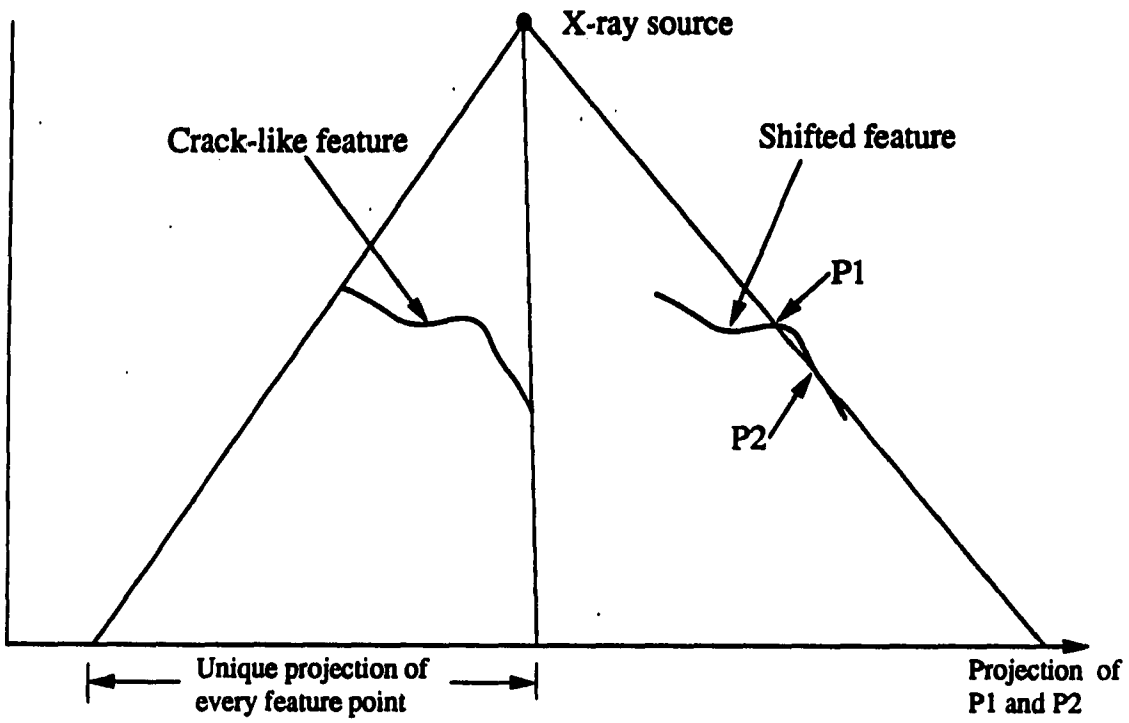

Figure 2.7: Example of the nonunique correspondence

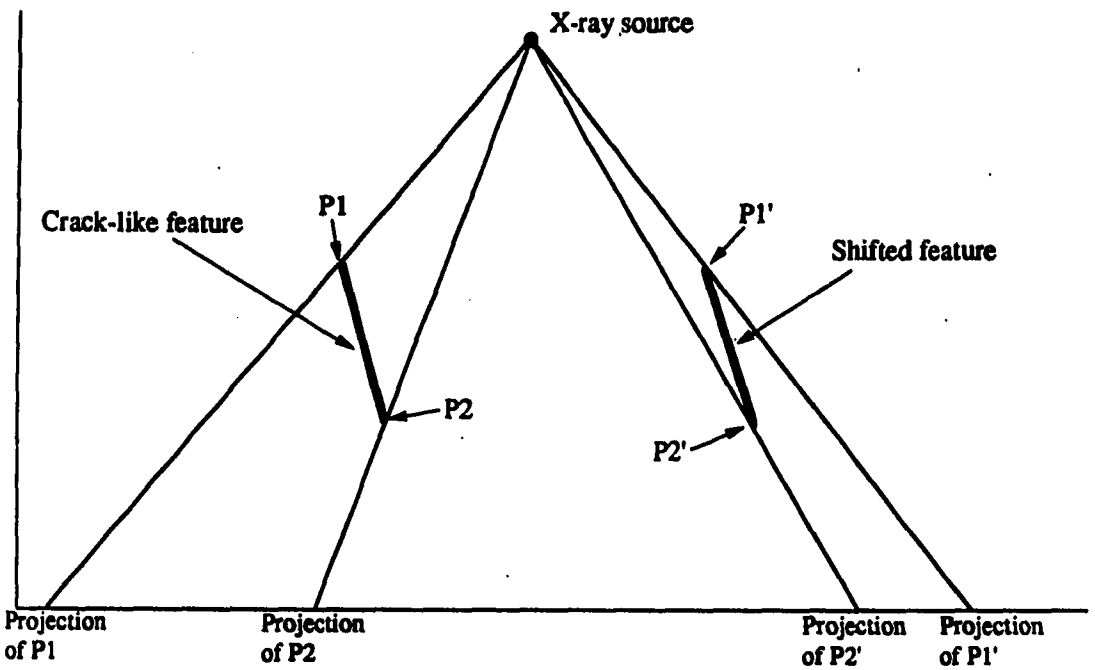

Figure 2.8: Example of crossed disparities

lie in a plane of unknown location and orientation. This assumption relaxes the requirement of exact correspondence. All that is required is the x-y locations of all feature points in stereographic scenes. Marr and Poggio (1979) assume uniqueness as well as slowly varying feature surfaces. They also introduce the idea of eliminating false matches by reducing the resolution of accepted disparities and limiting the absolute range of accepted disparities depending on the physical situation. An interesting book by Grimson (1981) has taken much of this work and shown how to implement it. In addition, it presents a very good literature review of the area of surface reconstruction from stereo images. The common feature of these techniques is that they attempt to match a large number of points in the image (either all image points or points along edge pixels) automatically.

An alternative approach is to match only feature points that are of interest. An obvious first step to this approach is to perform edge detection on the images and reconstruct only the edge features. Even with edge images, we still have a correspondence problem with matching points on the edges between the two images. The problem can be reduced by interpolation of the egdes and treating them as curves (Brint and Brady 1990) or piecewise linear curves (Mendioni and Nevatia 1985). There is a fundamental limitation, however when attempting to reconstruct the edges of a smoothly varying surface such as a spheroid. When such an object is viewed from different orientations, the edge points of its projections do not correspond to the same points on the physical surface on the object. Figure 2.9 illustrates this point. Notice that P1 and P2 do not correspond to points P1' and P2', respectively.

The most accurate correspondences are made when the feature of interest has sharp edges such that these edges can be identified with confidence in the stereo

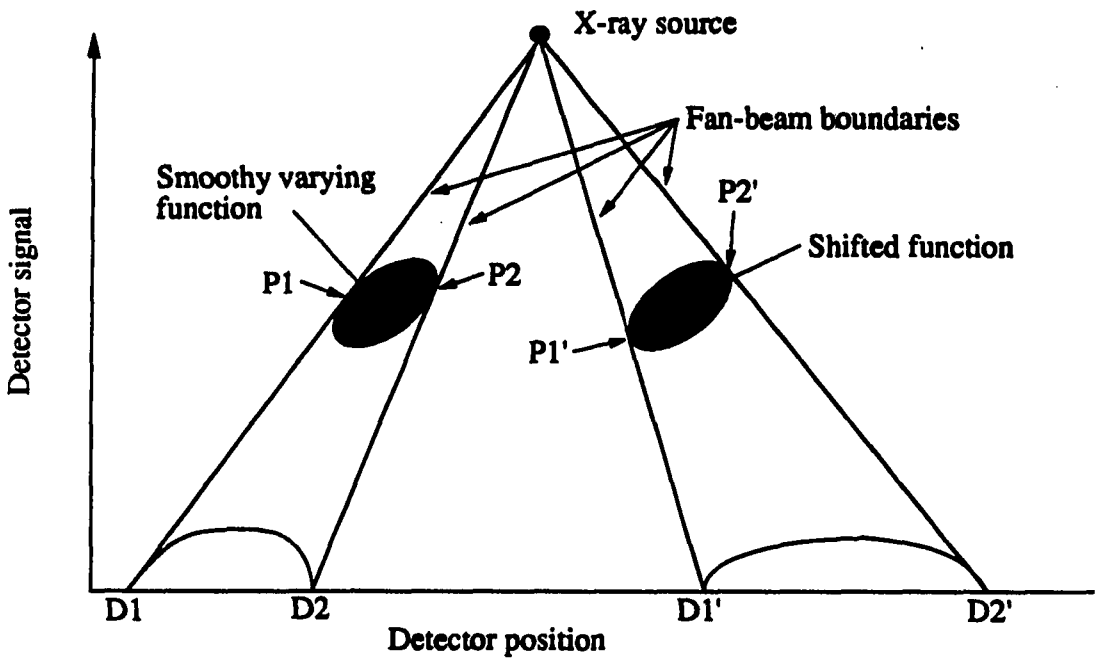

Figure 2.9: A smoothly varying surface projects noncorresponding edges

projections. Crack-like flaws generally meet this requirement as the ends of a crack usually terminate at a point and they usually have a one- or two-dimensional structure.

In an NDE application, stereographic reconstruction does not necessarily need to be performed automatically. In applications such as robotics and machine vision, the reconstruction is automatic by definition. In fact, there is a great reluctance in the NDE and medical fields to believe the results of reconstruction when automated processing is involved. The reason is that the error rates are too high and the penalty for error is very large. This reluctance is slowly disappearing as the field of image processing advances and effects of processing are quantified using rigorous information measures. In NDE flaw reconstruction, the images are often very complicated and only a few features require identification for reconstruction. The most accurate method of selecting the flaw features is manual identification. This requires the NDE technician to view each stereo pair of images and select the features to reconstruct as well as identify the corresponding features. When the number of features is relatively small, manual identification can be faster and more reliable than automatic identification. The primary advantages of automated identification in this type of situation are the reduction of operator fatigue and the cost savings of eliminating the operator from the task.

2.9 Interactive Stereo Correspondence and Reconstruction

With the permeation of graphics workstation computers into NDE, an interactive stereographic reconstruction routine is feasible in which the stereo image pairs are displayed side by side and features are reconstructed by interactively identifying

corresponding feature points in the left and right images. This type of reconstruction routine has been incorporated into a commercial image processing software package being developed at ISU (Brown et al. 1990). Among the features of this package are that it is user friendly, it is menu and mouse driven, and it is easy to augment with new routines as they become available. The stereographic reconstruction routine requires stereo image pairs and physical information about the inspection geometry. The routine initiates by prompting the user to select the left and right images with a mouse click in each image. The user is then prompted to point and click with the mouse at the location of an absolute reference point in both images. This reference point usually corresponds to the origin of the measurement coordinate system and serves as a reference for measuring the coordinates of the image features. A parameter menu then appears in which the physical distances and coordinates associated with the inspection geometry are entered. Figure 2.10 shows a photograph of the workstation display with two images and the parameter block displayed. A description of each parameter is given below:

source x = x coordinate of x – ray source location

source y = y coordinate of x – ray source location

source z = z coordinate of x – ray source location

reference x = x coordinate of reference point in images

reference y = y coordinate of reference point in images

shift x = Distance of source or sample translation in the x – direction

shift y = Distance of source or sample translation in the y – direction

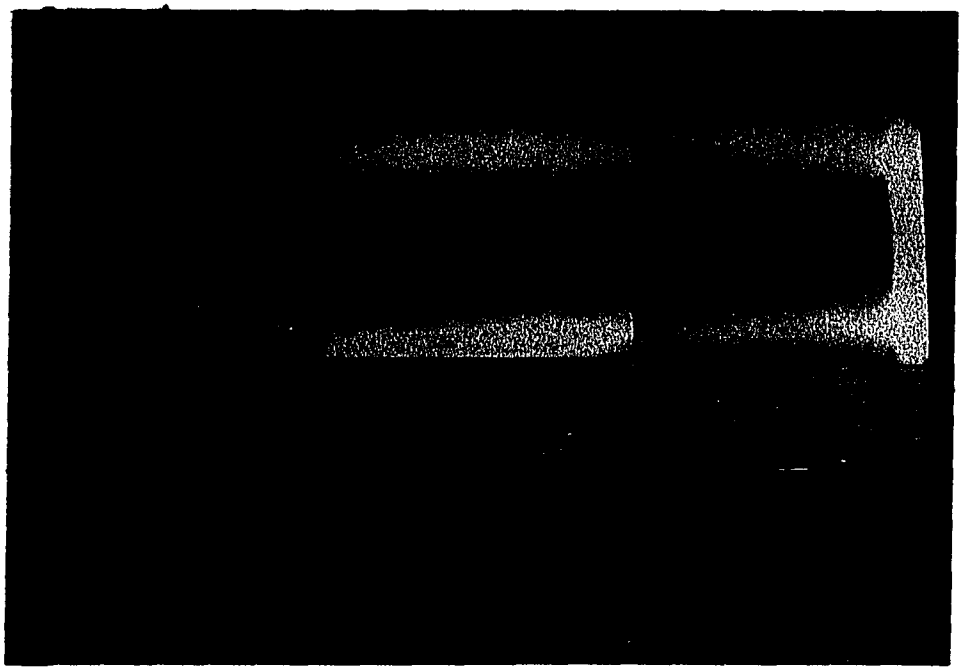

Figure 2.10: Interactive reconstruction environment

source or sample = Flag indicating a source or sample translation

dist/pix x = Absolute distance per pixel in the x direction

dist/pix y = Absolute distance per pixel in the y direction

numfeat = Number of points to be reconstructed

Done = Indication all parameters have been entered

The geometry used in the reconstruction computations of this package require that the plane of the detector correspond to the z=0 plane. It also assumes that the sample or source shift is invariant in z. Once the "done" menu is clicked in

the parameter menu block, the user is prompted to point and click corresponding features in the left and right images until the requested number of features have been identified. The routine then calculates the 3-D location of each feature with respect to the coordinate system origin and displays these coordinates in a new menu-type block. The feature points in the two images are highlighted and all coordinates of feature points and reconstructed points as well as the inspection geometry are recorded in an image history file.

2.10 Experimental Results of Stereographic Reconstruction

Tests of the stereographic reconstruction method were made on three types of objects. The objects were a fabricated sample consisting of a needle imbedded in a slab of paraffin wax, a railroad frog, and a fabricated sample consisting of holes of varying diameters and depths drilled into an aluminum slab.

2.10.1 Reconstruction of Needle Length

A sample was fabricated consisting of an ordinary sewing needle imbedded in a slab of paraffin wax. The objective was to accurately reconstruct the length of the needle from stereo projections from a microfocus x-ray source in magnification mode. Figure 2.11 shows a schematic diagram of the experimental setup. The x-ray machine was a Ridge microfocus (Model HOMX 160A) unit capable of generating x-rays with energy levels up to 160KeV. The approximate focal spot size of the source is 10 μm. The x-y stage was a computer controlled positioner for precise translation of the sample. A film cassette, holding Kodak DEF-5 film was used as the detector. The absolute reference was obtained by producing a shadow of a fixed needle onto

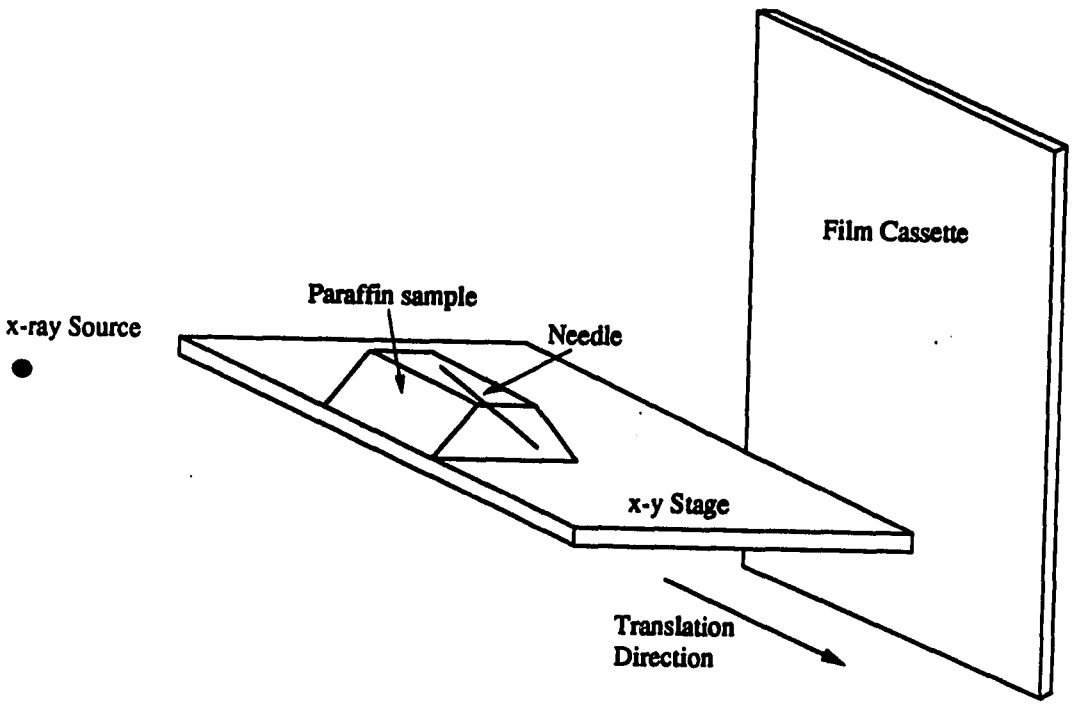

Figure 2.11: Experimental setup for stereo radiography

the films.

The stereo image pairs were produced by radiographing the sample after translating the sample 51 mm in the x direction. The image pairs are shown in Fig. 2.12. The needle is the large white diagonal line in the figure. In the digitized and duplicated images, it is difficult to see the needle endpoints especially when the shifted sample is close to the stand. In the original radiographs, however, the endpoints are readily visible. The fixed reference point is the tip of the vertical white feature

attached to the top of the stand.

The measurement quantities and reconstruction results for two independent experiments are summarized in Tables 2.1 and 2.2. Column two contains the measurements made of the quantities listed in column one. These include the coordinates of the needle endpoints on the film (x_{ij}, y_{ij}), the x-ray source coordinates (x_S, y_S, z_S), the sample shift (x_T) and the needle length. Column three contains the calculated values for the needle length as well as the coordinates of the needle endpoints in 3-D. Column four contains the estimated error bounds on the measured quantities and the computed error bounds on the computed quantities. The estimated error bounds on the film coordinates were obtained from the estimated precision of the ruler used to make the measurements and the geometric unsharpness. For the first experiment, the measurement error bounds were estimated to be approximately 0.5 mm. In the case of experiment run number 2, the geometric unsharpness was slightly less and a ruler with finer graduations was used, hence the reduction in the estimated error bounds. The error bounds for the source location were obtained by estimating the measurement imprecision, as great care was taken to align the experimental setup. The error bounds on the computed needle length and endpoint coordinates were calculated using Eq. (2.41) and Eqs. (2.43)-(2.47).

Notice that in both cases, the reconstructed needle length is very close to the true value (within 7 percent) and they are well within the predicted error bounds. The locations of the needle endpoints were not measured because the needle was embedded within the paraffin, making this measurement very difficult.

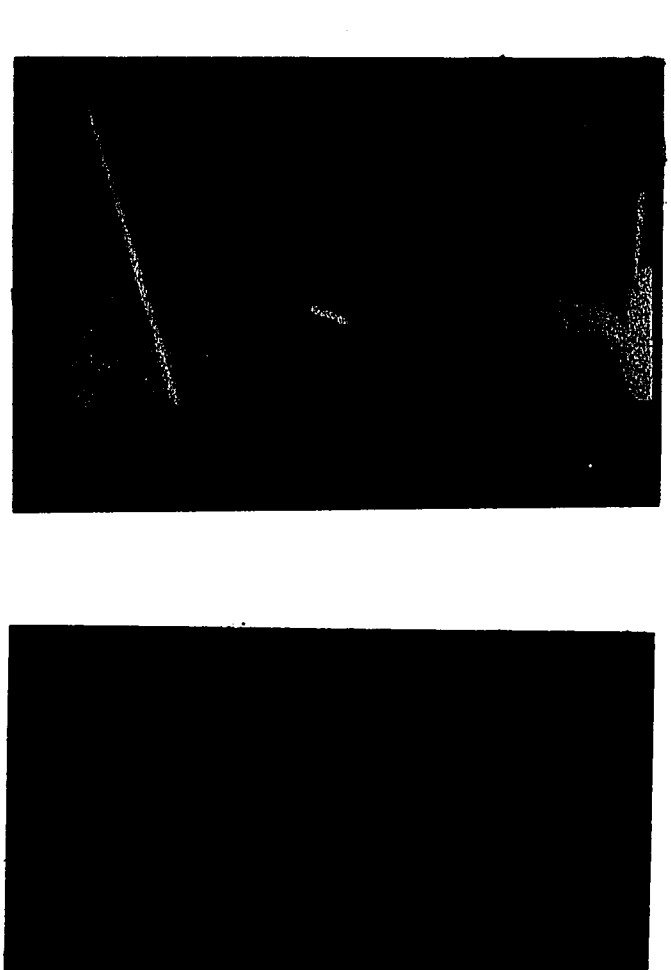

Figure 2.12: Stereo image pairs of needle imbedded in paraffin sample

Table 2.1: Reconstruction results of experiment run 1

Quantity	Measured value (mm)	Reconstructed value (mm)	Error bound (mm)
(x_{11}, y_{11})	(144.0,20.0)	-	± (0.5,0.5)
(x_{12}, y_{12})	(114.0,-50.0)	-	± (0.5,0.5)
(x_{21}, y_{21})	(38.0,20.0)	-	± (0.5,0.5)
(x_{22}, y_{22})	(2.0,-50.0)	-	± (0.5,0.5)
(x_T)	-51.0	-	-
(x_s, y_s, z_s)	(85,9,572)	-	± (2,2,2)
(x_{c1}, y_{c1}, z_{c1})	-	(113.4,14.3,296.8)	± (1.3,1.3,3.6)
(x_{c2}, y_{c2}, z_{c2})	-	(98.2,-17.9, 311.5)	± (1.3,1.6,3.4)
Length	41.0	38.5	± 6.1

Table 2.2: Reconstruction results of experiment run 2

Quantity	Measured value (mm)	Reconstructed value (mm)	Error bound (mm)
(x_{11}, y_{11})	(50.5,-34.0)	-	± (0.2,0.2)
(x_{12}, y_{12})	(15.0,-76.0)	-	± (0.2,0.2)
(x_{21}, y_{21})	(105.3,-34.5)	-	± (0.2,0.2)
(x_{22}, y_{22})	(73.0,-76.1)	-	± (0.2,0.2)
(x_T)	-38.1	-	-
(x_s, y_s, z_s)	(38,64,513)	-	± (2,2,2)
(x_{c1}, y_{c1}, z_{c1})	-	(46.7,-4.5,154.4)	± (0.8,1.2,3.4)
(x_{c2}, y_{c2}, z_{c2})	-	(22.9,-28.0,176.0)	± (0.8,1.5,3.2)
Length	41.0	39.8	± 6.1

2.10.2 Reconstruction of Features in a Railway Frog

A railway frog is the portion of railroad track where two rails come together and branch off into different directions. It is used to allow tracks that are going in different directions to cross each other. The railroad industry is continually inspecting and repairing these frogs as the ever-increasing railroad car tonnage causes them to crack and wear. Much of the cracking problem is caused by excessive loading, although some is caused by material shrinkage during fabrication at the foundry. Thus, the railroad industry and the frog manufacturers are interested in NDE inspection as a means of quality control as well as for detecting cracks due to loading.

The heavy and extremely large frogs are cast from a manganese steel alloy. When inspected for defects, a judgement regarding the feasibility of repair is made. There are essentially three options. Either the flaw content is deemed acceptable and the frog is put back into service, the flaws are repaired, or the frog is deemed unrepairable. Usually, the only frogs radiographed that have been in service are those which show some exterior signs of damage. Exterior wear or cracking can be easily repaired by welding and re-shaping the surface. The judgement of flaw acceptability is made by an experienced radiographer through the comparison of the radiographs against ASTM standard radiographs of varying degrees of flaw severity. The degrees range from level 1 (not very severe) to level 5 (very severe) for different flaw types (shrinkage cracks, porosity, inclusions). The cutoff for acceptability is somewhere around level 3. There is a fuzzy line on this point because of the inconsistencies between different radiographers and the problem of drawing the line between acceptable and unacceptable for such a wide variety of radiographs. When the flaw content is judged unacceptable, a repair is attempted by cutting into the frog with a torch until the

the flawed areas are found. If the areas are close enough to the surface, they can be repaired by welding. If not, they cannot be repaired because the structural integrity would be damaged. At present, the depths of the flaw areas are determined during the attempt to repair the frog. Therefore, it is advantageous to be able to compute flaw locations stereographically, saving the time and expense of cutting into unrepairable frogs.

To attempt a sterographic reconstruction of the depth of various flaws, three frogs were radiographed at the Chicago & Northwestern Railroad Reclamation Yard in Council Bluffs, IA. Unfortunately, the results have not yet been correlated with the results of destructive tests. However this will be done at a later time. Figure 2.13 shows a photograph of the radiographic setup. The frog was leveled by placing it between two equal-height stacks of railroad ties. It was then radiographed by clamping the x-ray source beneath the frog to a movable stand and placing the film cassette directly on top of the frog.

The stereo pairs were produced by shifting the source rather than the frog. Because the film holder was in contact with top surface of the frog, a shift of the source is essentially equivalent to a shift of the sample with a minor correction to the definition of the film coordinates. The film coordinates of the features in the image after the source shift must be shifted by an amount $-x_T$, where x_T is the source shift distance. Note that the coordinate being corrected is the one corresponding to the source shift direction. The x-ray source was an isotope of Iridium-192 with a strength of 62 Ci. This type of source is common in industrial radiography where penetration through large thicknesses of steel is required. The size of the source was 0.1" x 0.1". This size produces a detectable amount of geometric unsharpness in the

Figure 2.13: Experimental setup for frog radiography

image. A maximum bound on the unsharpness is 0.2 mm computed from Eq. (2.58).

$$U_{max} = \frac{d_2 s}{d - d_2} \tag{2.58}$$

where

s = Maximum length across x – ray source

d = Source to detector distance

d_2 = Maximum sample to detector distance.

Isotope sources also cause a film unsharpness on the order of 0.2 mm.

A lead reference marker was fixed to the top of the frog to establish the coordinate system. The source location was measured with respect to this marker by dropping a plumb bob down to the plywood surface and measuring distances on the plywood. After shifting the source, the film cassette was relaced with a fresh sheet of film and aligned on top of the frog. Figure 2.14 shows the digitized projections of the frog. Notice how the flaw features change position relative to the reference marker (white line). Table 2.3 summarizes the measurements and the results of reconstructing the depth of two flaw features identified in the images. Column two lists the appropriate measurements as well as the calculated depth for flaw 1, and column three lists the corresponding data for flaw 2. The two flaw features are identified with circles in Fig. 2.14. Estimates of the bounds on the measurement errors are ± 0.5 mm for the film coordinates and ± 5 mm for the x-ray source coordinates. These bounds were estimated by considering the maximum geometric unsharpness and the measurement precision. A different frog was radiographed on a later occasion with the intention of submitting it to accelerated service at a test facility in Pueblo, CO followed by

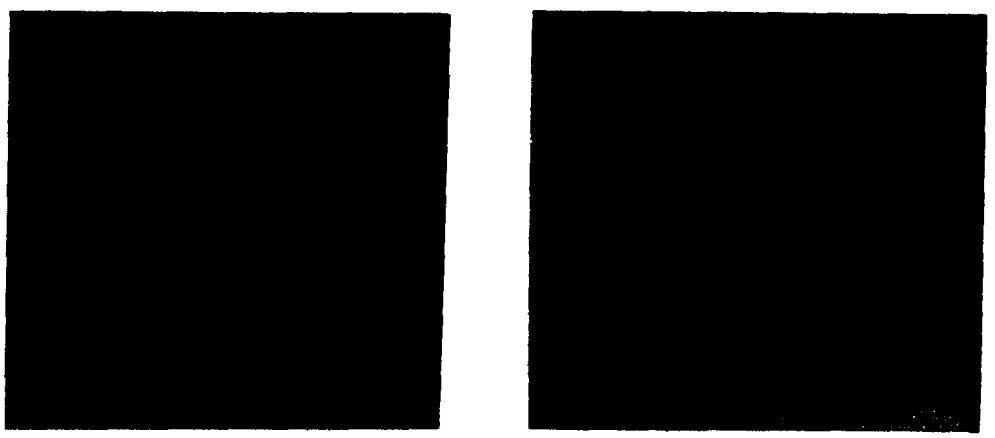

Figure 2.14: Stereographic projections of 1st railway frog (flaws of interest circled)

re-radiography and destructive sectioning. The radiography procedure was similar to that of the previous frog. The left and right stereo image pairs are shown in Fig. 2.15, and the corresponding reconstruction results are given in Table 2.4. In this case, four flaw points were selected for depth calculation as indicated by the four columns of Table 2.4. Estimates of the measurement error bounds are again ± 0.5 mm for the film coordinates and ± 5 mm for the x-ray source coordinates. The feature points selected for reconstruction are highlighted by white dots in Fig. 2.15.

Observe in both cases that feature points as opposed to crack endpoints were reconstructed as the flaw structure in the frog resembles porosity more than cracks. This is reasonable as long as the correspondence can be made with high confidence.

Table 2.3: Results of flaw depth reconstruction in 1st railway frog

Parameter	Flaw 1	Flaw 2
Film coordinate (x_{11}, y_{11}) (mm)	(25.5,0.0)	(-12.0,0.0)
Film coordinate (x_{21}, y_{21}) (mm)	(-79.5,0.0)	(-65.5,0.0)
Source shift x_T (mm)	-51	-51
Source position (x_S, y_S, z_S) (mm)	(0,0,524)	(0,0,524)
Reconstructed flaw depth (mm)	29.1 ± 9.4	24.5 ± 9.6

Table 2.4: Results of flaw depth reconstruction in 2nd railway frog

Parameter	Upper Flaw	Lower Flaw	Left Flaw	Right Flaw
Film coordinate (x_{11}, y_{11}) (mm)	(168.5,25.0)	(164.0,31.0)	(148.0,31.0)	(175.5,36.0)
Film coordinate (x_{21}, y_{21}) (mm)	(164.5,23.0)	(160.0,29.0)	(144.0,29.0)	(171.5,34.0)
Source shift x_T (mm)	-51	-51	-51	-51
Source position (x_S, y_S, z_S) (mm)	(191,0,600)	(191,0,600)	(191,0,600)	(191,0,600)
Reconstructed flaw depth (mm)	49 ± 9	44 ± 9	43.0 ± 9	43.0 ± 9

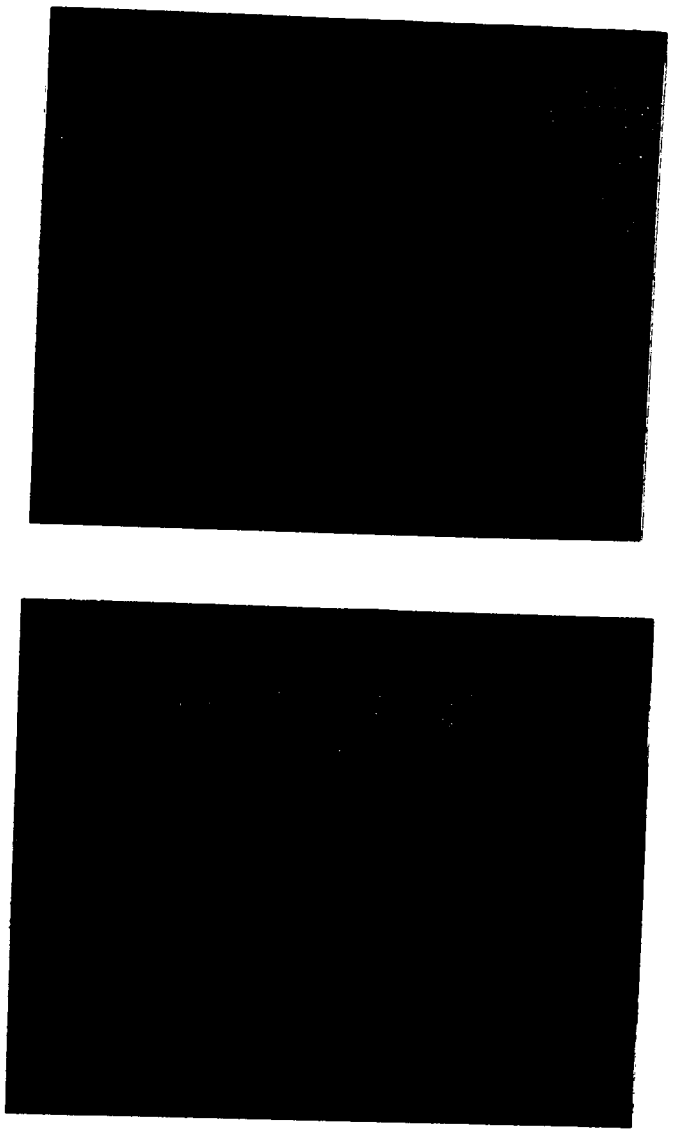

Figure 2.15: Stereographic projections of 2nd railway frog (flaws of interest highlighted)

In this case, feature points were selected that were relatively isolated and at the edge of the flaw structure. Also notice that the maximum error bound on the flaw depth is rather high. This could be improved by either making more accurate source location measurements or by reducing the source to film distance. In general, errors can be minimized by using the smallest possible source-film distance due to the lever arm effect. The trade-off of using small source-detector distance is the reduction in the feature shift distances between various projections. The feature shift must be sufficiently large to be measurable. The feature shift amount can be increased, however, by increasing the magnification.

In any case, these experiments demonstrate the promise of this technique in real NDE applications in the field. It remains to be seen, however, how well the results correlate with destructive tests. At this point the first frog has finished accelerated service after having a failure and is in the process of being re-radiographed and destructively sectioned. The accelerated testing was performed on the test frog because the railroad industry required data on the performance of the frog under heavy axle load in a controlled environment.

2.10.3 Fabricated Sample of Drilled Holes in an Aluminum Block

To provide another verification of the stereographic reconstruction technique on a sample with varying degrees of feature detectability, a sample was fabricated consisting of several 0.5 inch thick aluminum slabs. One of these slabs had a series of flat bottom drilled holes of varying diameters and depths. The objective was to place the drilled slab between the undrilled slabs and reconstruct the location of the various holes in the sandwich. The variation in depth of the holes created features

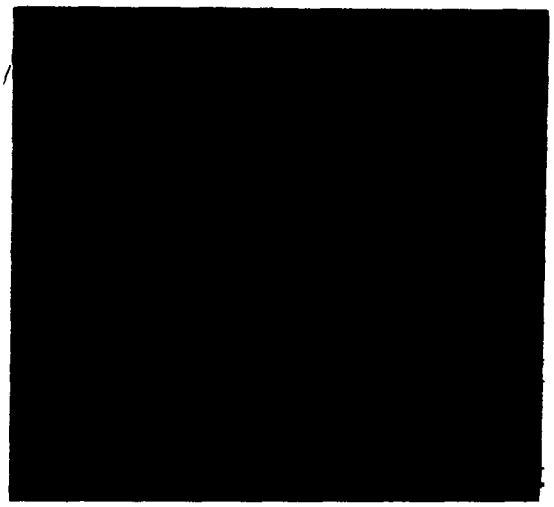

Figure 2.16: Real-time radiograph of drilled block sample (128 averages)

ranging from undetectable to easily detectable.

The drilled slab was clamped between two undrilled slabs and radiographed using a real-time image intensifier detector. The radiographs were made by translating the sample on an automatic positioner to three separate locations and capturing the image using a digitizing frame-grabber. Figure 2.16 shows the first radiograph of the sandwich after 128 ensemble averages. The average was obtained by repeatedly acquiring an image from the intensifier and continually averaging the acquired image with the previous image. This is equivalent to acquiring 128 separate images and averaging them.

This type of averaging dramatically reduces the level of the electronic noise in

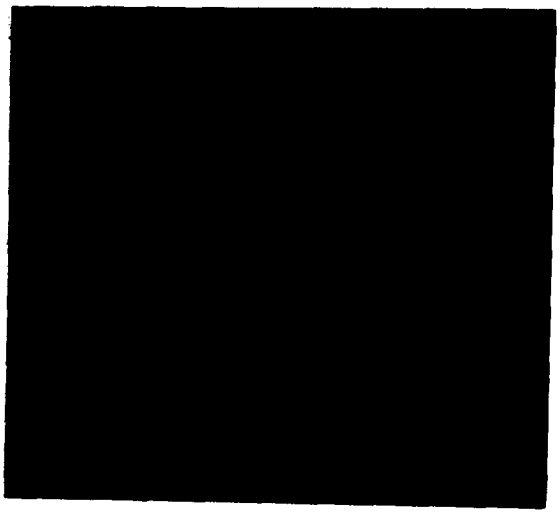

Figure 2.17: Background image obtained from real-time system

the camera and the x-ray generator noise as the realtime detector by itself does not have any integration capacity. The dark line near the right side of the image serves as a reference point for the reconstruction coordinate system. It was established by mounting a paper clip to the face of the intensifier. The image quality was further improved by subtracting a background image with no sample. This removed the effects of imperfections in the camera optics as well as trends across the image caused by spatial variations in the detector response, radial divergence, and beam fall-off. The background image used in the subtraction is shown in Fig. 2.17.

The resultant three radiographs after background subtraction and slight contrast stretching are shown in Fig. 2.18. The holes in the images are not quite circular due

to an aspect ratio inconsistency between the frame grabber electronics and the image display. This is not too important, however, because a geometric calibration is performed to establish the number of pixels per physical distance unit in the image plane. This is done by radiographing a circular ceramic disk of known diameter mounted to the face of the intensifier. By counting the maximum number of pixels within the extent of the disk in the x and y dimensions, calibration factors for distance/pixel are established for the x and y directions. Figure 2.19 shows the image of the disk after background subtraction. Notice its oblate nature due to the inconsistent aspect ratios. The measured diameter of the disk was 38.0 mm. The extent of the disk in the x-direction was 175 pixels and the extent in the y-direction was 221 pixels. Thus the calibration factors were

$$k_x = 0.218 \quad \text{mm per pixel}$$

$$k_y = 0.172 \quad \text{mm per pixel.}$$

These calibration factors are useful for any image acquired from the same image intensifier detector because no magnification is used.

The source location with respect to the reference point was x=13 $\pm$ 2 mm, y=25 $\pm$ 2 mm, z=1984 $\pm$ 5 mm. The first translation distance was 18.0 $\pm$0.5 mm, and the second translation distance was 25.0 $\pm$0.5 mm.

The coordinates of the holes to be used in depth reconstruction were selected manually as the center of the holes to minimize correspondence error. The z-location of each hole was reconstructed using the first and third image for the smaller diameter holes, and the second and third image for the larger diameter holes. The results are summarized in Table 2.5 for both the least squares (column 2) and total least squares (column 3) solution using the linear model. The small hole terminology in the table

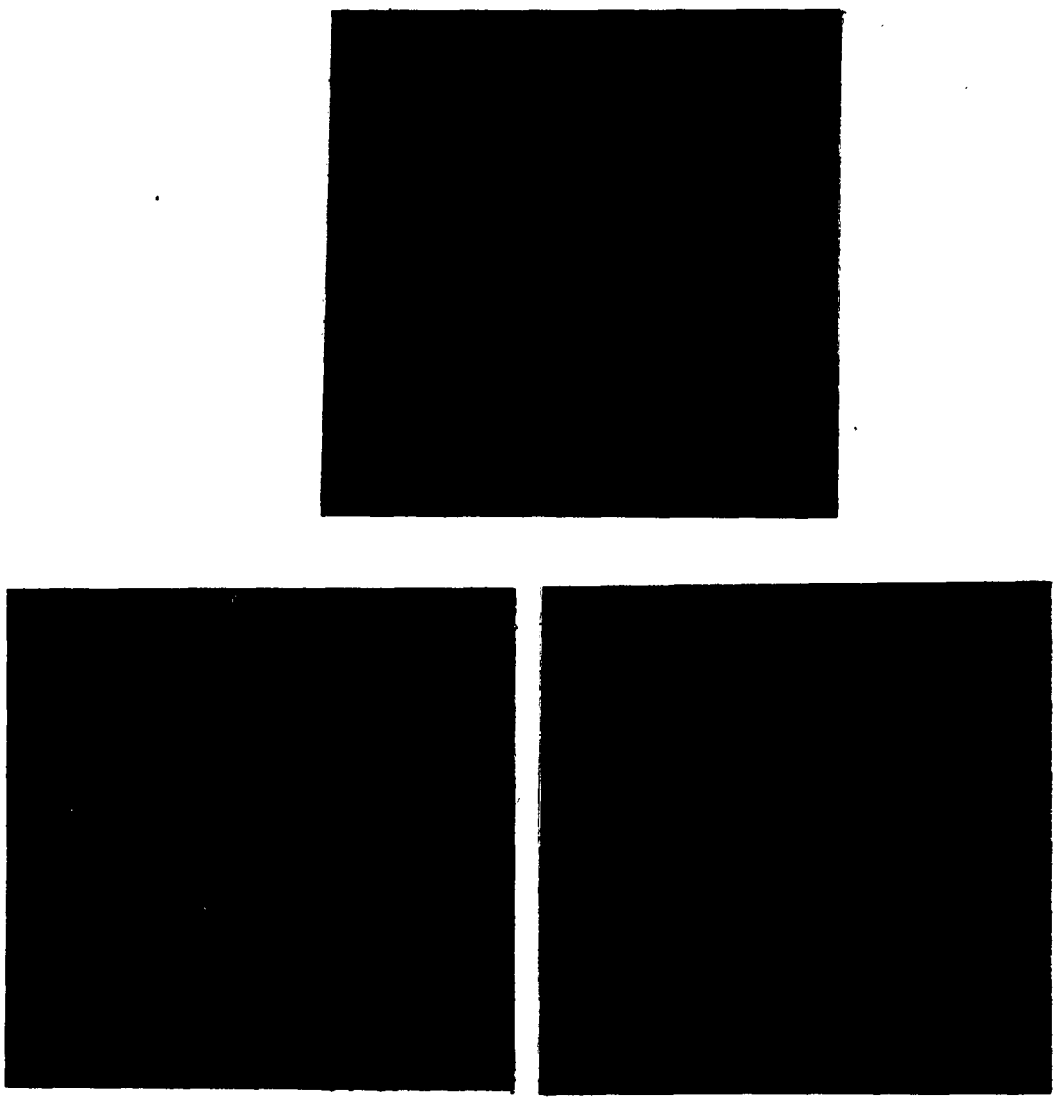

Figure 2.18: Drilled block radiographs after background subtraction

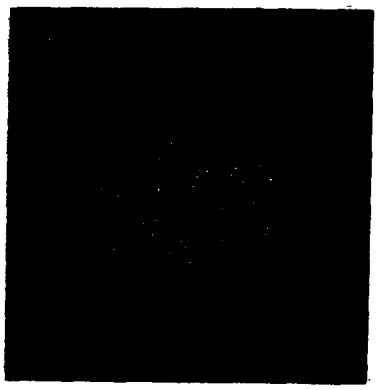

Figure 2.19: Radiograph of calibration disk

refers to the column of holes on the right hand side of the first image in Fig. 2.18. The large hole refers to the column of larger holes on the left hand side of the same image. The numbering of the holes begins with 1 at the top and continues with 2, 3, 4, toward the bottom. Approximate upper bounds on the reconstruction error have been computed by using the nominal measurement values in the sensitivity-error analysis equations.

Notice that the reconstructed hole locations are fairly close to the true value and are well within the bounds predicted by the error analysis. The reason that the error bounds are large is the fact that the source-detector distance is so great. These errors could be reduced significantly if this distance were reduced. The fractional error as a percentage of the source-film distance would essentially remain the same, however.

Table 2.5: Results of z-location reconstruction of holes in drilled block

Hole	z-location LS (mm)	z-location TLS (mm)	True z-location (mm)
small hole 1	578 ± 22	579 ± 22	565 ± 5
small hole 2	578 ± 22	579 ± 22	565 ± 5
small hole 3	561 ± 22	561 ± 22	565 ± 5
small hole 4	580 ± 22	578 ± 22	565 ± 5
large hole 1	570 ± 21	572 ± 21	565 ± 5
large hole 2	560 ± 21	561 ± 21	565 ± 5
large hole 3	549 ± 21	554 ± 21	565 ± 5
large hole 4	560 ± 21	561 ± 21	565 ± 5

2.11 Stereographic Reconstruction Through Sample Rotation

In some inspection situations where the part under test is relatively small and inspectable from various angles, it is more convenient or easier to rotate the sample rather than translate it. The CT inspection scheme usually involves rotation of the sample or a bank of detectors. Thus, it seems reasonable to formulate the stereo reconstruction equations in terms of a sample rotation.

We define the reconstruction geometry as shown in Fig. 2.20. The object under test is rotated in the x-z plane by an angle θ. The x-z plane is chosen for the rotation because it is easily implemented with a turntable type sample holder. Considering a single feature point to be reconstructed we write the following parameterized vector equations:

$$\mathbf{X}_f = x_1\hat{i} + y_1\hat{j} + t_1\{(x_s - x_1)\hat{i} + (y_s - y_1)\hat{j} + z_s\hat{k}\} \tag{2.59}$$

$$\mathbf{X}_f' = x_1'\hat{i} + y_1'\hat{j} + t_2\{(x_s - x_1')\hat{i} + (y_s - y_1')\hat{j} + z_s\hat{k}\} \tag{2.60}$$

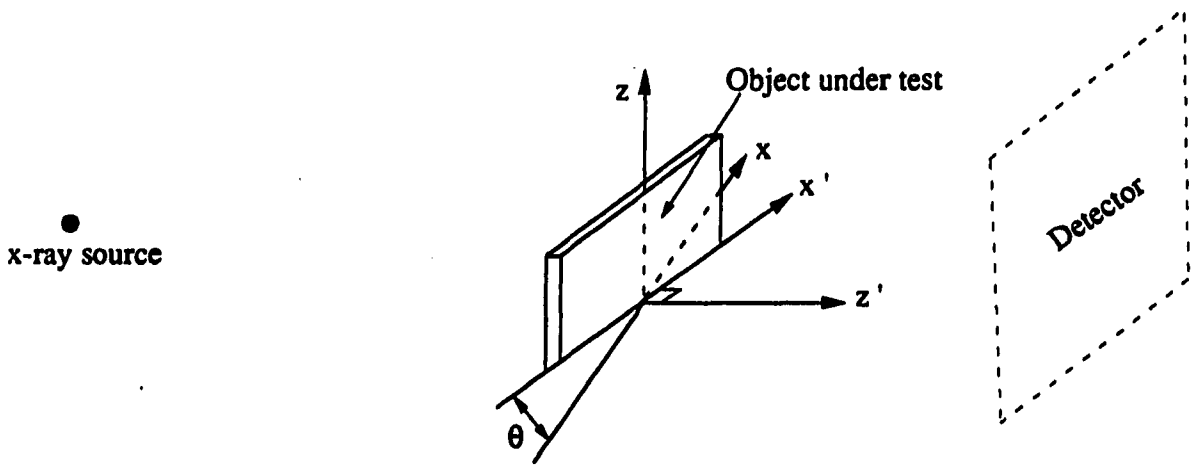

Figure 2.20: Geometry used in sample rotation scheme

where $\mathbf{X_f}$ is the vector from the origin to the line connecting the x-ray source to the feature in the image, $x_1\hat{i} + y_1\hat{j}$ is the vector from the origin to the feature in the image, and t_1 and t_2 are parameters. Note: The primed quantities correspond to the vectors and coordinates after rotation.

The left hand sides of the above equations are constrained to the feature point in the material, (x_c, y_c, z_c) yielding

$$x_c\hat{i} + y_c\hat{j} + z_c\hat{k} = x_1\hat{i} + y_1\hat{j} + t_2\{(x_s - x_1)\hat{i} + (y_s - y_1)\hat{j} + z_s\hat{k}\} \quad (2.61)$$

$$x'_c\hat{i} + y'_c\hat{j} + z'_c\hat{k} = x'_1\hat{i} + y'_1\hat{j} + t_2\{(x_s - x'_1)\hat{i} + (y_s - y'_1)\hat{j} + z_s\hat{k}\}. \quad (2.62)$$

From the two vector equations, we write the following six scalar equations:

$$x_c = x_1 + t_1(x_s - x_1) \quad (2.63)$$

$$y_c = y_1 + t_1(y_s - y_1) \quad (2.64)$$

$$z_c = t_1 z_s \quad (2.65)$$

$$x'_c = x'_1 + t_2(x_s - x'_1) \tag{2.66}$$

$$y'_c = y'_1 + t_2(y_s - y'_1) \tag{2.67}$$

$$z'_c = t_2 z_s \tag{2.68}$$

Unless the coordinate origin is the center of rotation for the object, the center of rotation must be specified as (x_r, y_r, z_r). The rotation of the feature point (x_c, y_c, z_c) can be described by the following linear transformation.

$$\begin{bmatrix} x''_c \\ y''_c \\ z''_c \end{bmatrix} = \begin{bmatrix} \cos\theta & 0 & -\sin\theta \\ 0 & 1 & 0 \\ \sin\theta & 0 & \cos\theta \end{bmatrix} \begin{bmatrix} x_c - x_r \\ y_c - y_r \\ z_s - z_r \end{bmatrix} \tag{2.69}$$

where the double primed quantities indicated the location of the rotated feature in the (x_r, y_r, z_r) reference frame. Converting back to the original coordinate system, we have

$$x'_c = x''_c + x_r \tag{2.70}$$

$$y'_c = y''_c + y_r \tag{2.71}$$

$$z'_c = z''_c + z_r \tag{2.72}$$

or,

$$x'_c = (x_c - x_r)\cos\theta - (z_c - z_r)\sin\theta + x_r \tag{2.73}$$

$$y'_c = y_c \tag{2.74}$$

$$z'_c = (x_c - x_r)\sin\theta + (z_c - z_r)\cos\theta + z_r \tag{2.75}$$

The scalar equations are now rewritten as

$$x_c = x_1 + t_1(x_s - x_1)$$

$$y_C = y_1 + t_1(y_S - y_1)$$

$$z_C = t_1 z_S$$

$$(x_C - x_r)\cos\theta - (z_C - z_r)\sin\theta + x_r = x_1' + t_2(x_S - x_1')$$

$$y_C = y_1' + t_2(y_S - y1')$$

$$(x_C - x_r)\sin\theta + (z_C - z_r)\cos\theta + z_r = t_2 z_S,$$

which can be written as the following linear system of equations:

$$\begin{bmatrix} 1 & 0 & 0 & (x_1 - x_S) & 0 \\ 0 & 1 & 0 & (y_1 - y_S) & 0 \\ 0 & 0 & 1 & -z_S & 0 \\ \cos\theta & 0 & -\sin\theta & 0 & (x_1' - x_S) \\ 0 & 1 & 0 & 0 & (y_1' - y_S) \\ \sin\theta & 0 & \cos\theta & 0 & -z_S \end{bmatrix} \begin{bmatrix} x_C \\ y_C \\ z_C \\ t_1 \\ t_2 \end{bmatrix} =$$

$$\begin{bmatrix} x_1 \\ y_1 \\ 0 \\ x_r\cos\theta - z_r\sin\theta - x_r + x_1' \\ y_1' \\ x_r\sin\theta + z_r\cos\theta - z_r \end{bmatrix} \tag{2.76}$$

This linear system can be used in the least squares or total least squares estimators to obtain minimum squared error estimates of the feature coordinates. The manner of implementation is very similar to that of the linear sample shift formulation. The major differences are that two parameters (t_1 and t_2) are computed during

the solution of the system and that the coordinates of the center of rotation, (x_r, y_r) are required. The film coordinates of the flaws of interest and the coordinates of the x-ray source are measured in the same manner described in the sample shift method.

3. 2-D VOLUMETRIC FLAW RECONSTRUCTION

In volumetric flaw reconstruction, the goal is to not only reconstruct the locations of flaws but to reconstruct their shape and other properties as well. By definition, the flaw consists of some volume of anomalous material, be it a void of gas or an area of different density solid such as an inclusion. In the medical field, this subject has been addressed vigorously since the early part of the century. The goal is to reconstruct areas in the human body under suspicion of abnormal growths or disease. As stated earlier, one of the most popular methods of quantitatively reconstructing the shapes and locations of flaws is Computed Tomography (CT). This method has gained unprecedented popularity in the medical field due to its accurate results (approaching 1 part in 1000) (Kak and Slaney 1988) and its safety to the patient. CT has also been applied to the field of Nondestructive Evaluation (Hack et al. 1987; Reimers and Goebbels 1983). A major problem with CT, however, is that a large number of projections is required by angular scanning around the object. As discussed earlier, many objects are not inspectable in certain directions due to their geometry. The lack of projection data at some angular positions in the CT reconstruction algorithms creates severe artifacts in the reconstructed cross-sections. Many efforts have been made recently to reduce these artifacts with astounding results. Among these efforts include iterative CT reconstruction using a priori knowledge of the part under test

(Tam et al. 1989), maximum entropy reconstruction of CT data (Park and Park 1987, Safaeinili et al. 1991), constrained extrapolation (Kudo and Saito 1988), iterative algebraic reconstruction (Andersen 1989) and Bayesian reconstruction (Hanson and Wecksung 1983). There are cases, however, where the inspectability is severely limited and only a few projections over a limited angle range may be taken. This occurs when a film detector or a radioisotope source is used. In this situation, a CT type reconstruction is hopeless. One of the distinguishing features of CT is that it reconstructs whatever is present in the x-ray beam regardless of whether it is of interest or not. By considering only those features of interest and modeling them as geometric figures, the number of projections required to reconstruct the model can be very small. This reduction is expected from an information theory standpoint [1] as we assume we know something about the shape of a feature (i.e., described by a model). Thus, the feature or flaw can be described by a relatively small number of model parameters.

Model-based *stereology* concepts can be very useful in determining properties of volumetric flaws. Much of the work in stereology has been applied to the natural sciences to determine geometric properties of objects in 2-D images by assuming geometric shapes such as ellipsoids of revolution and cylinders (Russ 1986; Elias and Hyde 1983; Saxl 1989). These same ideas can be applied to x-ray projection images after correction for magnification. However, much of the theory behind stereology involves geometric statistics to show the reliability of geometric models when large

[1] Information theory specifies that the number of bits required to describe or encode a signal depends on its information content. Information is defined as the amount of *randomness*. For a signal that is well known, i.e., less random, a smaller number of bits are required.

samples of objects are being described. For instance, when modeling cylinders, computed properties such as volume and surface area can be very inaccurate depending on the orientation of the cross section through the cylinder. For a large number of randomly oriented cylinders, geometrical statistics can show that the estimate of the total volume of all of the cylinders approaches the true value, on average. This makes sense intuitively through the process of over and under estimating the volumes due to the particular orientations. In our case, we don't have the luxury of a large sample of objects to reconstruct. Typically, there are one, two, or several flaws within the field of view. Some of the measures presented in stereology still can be very useful however when we understand the nature of the possible errors and we understand the assumptions behind the measures. Combining stereological concepts with the stereographic methods of Chapter 2 can be a powerful yet simple way to estimate the geometric properties. This will be addressed in the Chapter 5. The technique presented in this chapter is also model based, but is considerably more complicated and potentially more accurate.

Ultimately, we wish to reconstruct volumetric flaw-like features with a 3-D geometric model so that equivalent size, volume and location information can be determined. Performing an accurate 3-D model reconstruction is a complicated problem, especially due to the geometry involved and the difficulty in visualizing many of the equations. For this reason, it is useful to first derive analogous reconstruction methods for the 2-D case. Once these are well understood, it is a much simpler matter to generalize them to the full 3-D case. In this chapter, an elliptical flaw model is used to simulate a cross section through a volumetric flaw. Analytical x-ray projection models are derived for both parallel and fan-beam (microfocus) x-ray sources.

Finally, inverse algorithms are implemented to estimate the model parameters based on simulated data using an exact solution and least squares solution.

3.1 Discussion of Geometric Model

In selecting a model for a volumetric flaw, there are many issues to consider. Most importantly, the model must accurately describe the nature of the flaw. In addition, the model should be robust enough to accurately describe a wide variety of commonly occurring volumetric flaws. The model should also be simple enough so that it can be visualized by its parameters. In addition, it should be simple enough that the inverse problem is numerically tractable. In selecting a geometric model, it should be pointed out that we are considering the flaws of interest to be homogeneous. This relaxes the requirement that the flaw model have a spatial distribution in 3-D. Thus, we can select a model that is essentially a surface and use this surface as the flaw boundary.

One of the first models that comes to mind is a polygon. Some researchers have modeled objects in scenes using polygons and three-view stereo images (Hung et al. 1989) with good results. One of the problems involved with polygonal models, however, is the correspondence problem which enters through the requirement of matching polygon vertices. In addition, the complexity of the model equation is very high. Granted, a general n-sided polygon can well approximate many convex flaw distributions, however, it is difficult to write general analytical expressions for the forward projection model.

A three-axes ellipsoid is a simple geometric surface that can take on a wide variety of shapes depending on its parameter values. The parameters are the principal axes

lengths, the orientation angles and the location of the center. By varying the ratios of principal lengths, various shapes ranging from long thin needles to flat pancakes, to spheroids, can be obtained. In addition, the analytical equations involved in developing a general forward projection model are reasonable. For these reasons, the ellipsoid was chosen as the geometric model for volumetric flaws. In this chapter, we are concerned with arbitrary ellipsoid cross sections (which are ellipses (Gellert et al. 1975)) to simplify the mathematics.

3.2 Forward Projection Model

The forward projection model for the elliptical flaw can be thought of as the model of the signal that would be present on the x-ray detector in the presence of an elliptical flaw. Actually, this is an oversimplification since we will neglect the physics of the x-ray generation and detector output. What we are considering here are the the path lengths of the x-rays inside and outside the material. This process is the primary cause of a signal in the presence of a flaw. The absence or presence of some anomalous material causes a change in the overall x-ray attenuation as compared with the attenuation through other defect-free regions, giving rise to a change in the detector signal. This change is called contrast and is generally defined as

$$C = \frac{\Delta I}{\bar{I}} \tag{3.1}$$

where $\bar{I}$ is the average background intensity and ΔI is the change in the intensity on the feature or region of interest (Macovski 1983). Assuming a single homogeneous elliptical flaw in a nonattenuating background medium [2], the detector signal is related

[2] Although an unrealistic situation in practice, this simplifies the mathematical development. The detector signals can be processed to account for this assumption.

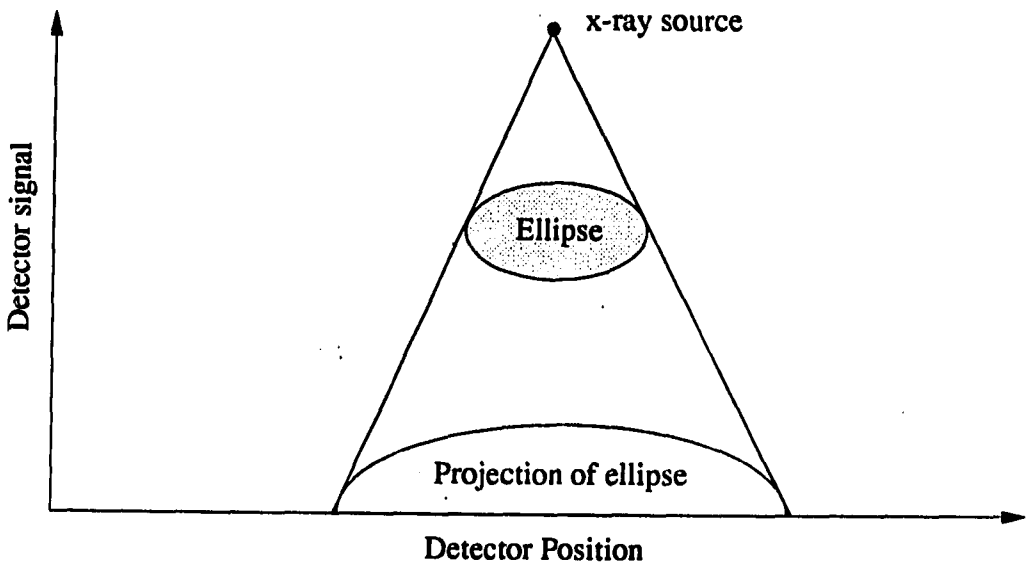

Figure 3.1: Detector signal vs. position for a homogeneous elliptical flaw

to the path length of the x-ray wave inside the ellipse. Figure 3.1 shows the detector signal versus position for an example ellipse and a point x-ray source.

The value of the signal at any position on the detector is also related to the Radon transform of the object. The Radon transform is the line integral of the object's x-ray attenuation coefficient function along a certain path defined by an orientation angle

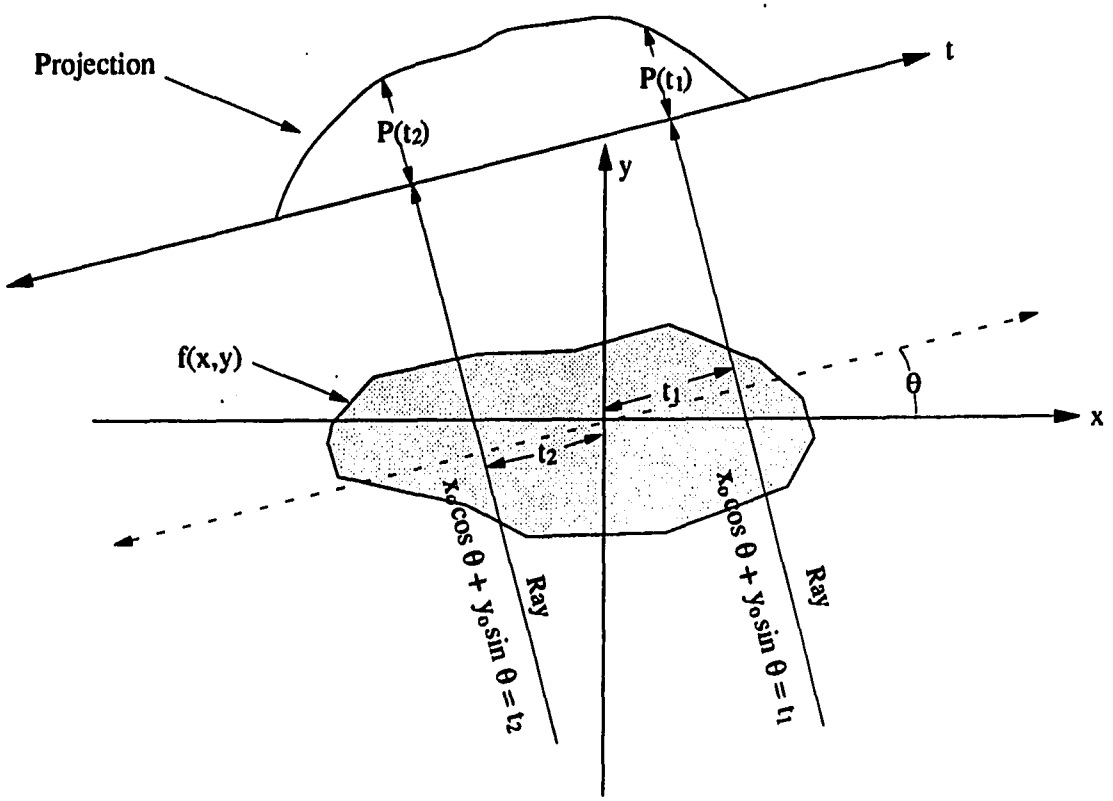

Figure 3.2: Geometry used in the Radon transform (from Kak and Slaney, 1988)

and a detector position. The Radon transform, given by (Deans 1983)

$$\mathsf{R}[f(x,y)] = P_\theta(t) = \int_{x-ray\ line} f(x,y)ds. \tag{3.2}$$

assumes that all x-rays are parallel with their paths perpendicular to the detector line, t, as shown in Fig. 3.2.

Here, $f(x,y)$ is the object attenuation coefficient function, θ defines the orientation of the detector, t specifies the position on the detector, and ds is the differential

x-ray path length. In CT reconstruction, the Radon transform is the quantity that is measured. The object is reconstructed by inversion of the Radon transform, yielding $f(x,y)$. In the model based reconstruction presented here, the Radon transform of the object under test is also measured (albeit at many less θ values), but an elliptically bounded constant is assumed for $f(x,y)$ and is reconstructed on a least squared error criterion.

The attractiveness of using the Radon transform in this type of reconstruction is that it provides a useful analytical formalism to the forward projection model and it has certain properties which allow for easy translation and rotation of the object.

We begin by deriving the Radon transform of an elliptically bounded constant centered at the coordinate origin with its principal axes aligned with the coordinate axes as shown in Fig. 3.3. The elliptical function is given by

$$f(x,y) = \begin{cases} 1 & \text{if } \left(\frac{x}{a}\right)^2 + \left(\frac{y}{b}\right)^2 \leq 1 \\ 0 & \text{otherwise} \end{cases} . \tag{3.3}$$

The line representing the detector position for evaluation of the Radon transform is given by the t axis and is specified by the line having equation $y = x\tan\theta$. The equations of the lines representing the x-ray paths through the ellipse are thus given by

$$y = -x\cot\theta + b_O \tag{3.4}$$

where b_O depends on the location of t. For a given detector position, b_O is computed by setting $x = t\cos\theta$ and $y = t\sin\theta$ in Eq. (3.4). We have

$$t\sin\theta = -t\cos\theta\cot\theta + b_O, \tag{3.5}$$

and after some manipulation,

$$b_O = t\csc\theta, \tag{3.6}$$

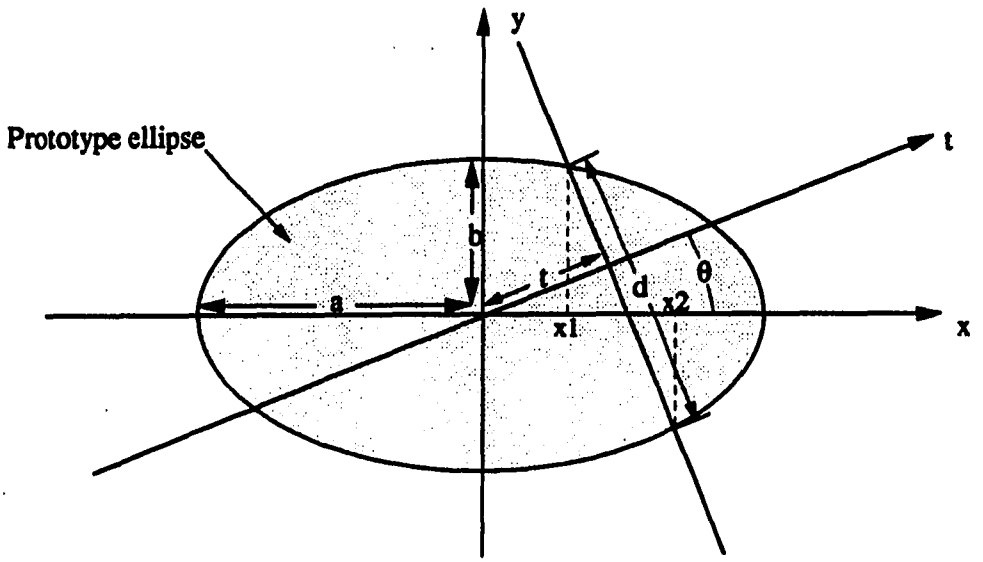

Figure 3.3: Geometry for computing the Radon transform of the prototype ellipse

and

$$y = -x\cot\theta + t\csc\theta. \tag{3.7}$$

Because $f(x,y)$ is constant within the ellipse, the Radon transform is simply the length of the x-ray path within the ellipse. This is computed geometrically as follows.

We have

$$y^2 = b^2\left(1 - \frac{x^2}{a^2}\right) \qquad \text{elliptical boundary} \tag{3.8}$$

$$y = -x\cot\theta + t\csc\theta \qquad \text{x-ray line} \tag{3.9}$$

The points of intersection of the ellipse with the x-ray line are found by equating Eq. (3.8) to the square of Eq. (3.9), yielding

$$b^2 - b^2\frac{x^2}{a^2} = (-x\cot\theta + t\csc\theta)^2. \tag{3.10}$$

This results in the following quadratic equation:

$$x^2\left(\cot^2\theta+\frac{b^2}{a^2}\right)+x(-2t\cot\theta\csc\theta)+t^2\csc^2\theta-b^2=0. \tag{3.11}$$

The two solution points are given by

$$x_{1,2}=\frac{(2t\cot\theta\csc\theta)\pm\sqrt{4t^2\cot^2\theta\csc^2\theta-4\left(\frac{b^2}{a^2}+\cot^2\theta\right)(t^2\csc^2\theta-b^2)}}{2\left(\frac{b^2}{a^2}+\cot^2\theta\right)}. \tag{3.12}$$

The x-ray path distance, d, is projected onto the x axis by

$$d_x=x_2-x_1=d\sin\theta. \tag{3.13}$$

Substituting the two solutions of Eq. (3.12) into Eq. (3.13) and solving for d, we obtain

$$\mathsf{R}[f(x,y)]=d=\frac{2ab\sqrt{b^2\sin^2\theta+a^2\cos^2\theta-t^2}}{b^2\sin^2\theta+a^2\cos^2\theta}. \tag{3.14}$$

When Eq. (3.12) yields a single solution or imaginary solutions, it means that the x-ray path line is either tangent to the ellipse or not intersecting it at all. In writing the expressions for the projection, as in Eq. (3.14), we assume that the solutions are real. Otherwise, we define the projection to be zero. Henceforth, all expressions for the projections make this implicit assumption to avoid the use of indicator functions.

3.2.1 Rotation and Translation of the Model

In order to derive the projections of the elliptical model for arbitrary location and orientation, rotation and translation properties of the Radon transform must be used. We begin by rewriting the definition of the Radon transform as

$$\mathsf{R}[f(x,y)]=g(t,\theta)=\int_{-\infty}^{\infty}\int_{-\infty}^{\infty}f(x,y)\delta(x\cos\theta+y\sin\theta-t)dxdy. \tag{3.15}$$

Notice that the delta function is unity on the x-ray line and zero everywhere else, causing the integral to sift $f(x,y)$ on the x-ray line.

The translation property of the Radon transform can be derived by considering an object function, $f(x,y)$ to be shifted by amount (x_o, y_o). The Radon transform of the shifted object is

$$\bar{g}(t,\theta) = \int_{-\infty}^{\infty}\int_{-\infty}^{\infty} f(x-x_o, y-y_o)\delta(x\cos\theta + y\sin\theta - t)dxdy. \tag{3.16}$$

Substituting $u = x - x_o$ and $v = y - y_o$, we have

$$\bar{g}(t,\theta) = \int_{-\infty}^{\infty}\int_{-\infty}^{\infty} f(u,v)\delta(u + x_o\cos\theta + v + y_o\sin\theta - t)dx\ dy \tag{3.17}$$

$$= \int_{-\infty}^{\infty}\int_{-\infty}^{\infty} f(u,v)\delta(u\cos\theta + v\sin\theta - (t - x_o\cos\theta - y_o\sin\theta))dudv \tag{3.18}$$

$$= g(t - x_o\cos\theta - y_o\sin\theta, \theta). \tag{3.19}$$

Thus, the Radon transform of a shifted ellipse with center (x_o, y_o) can be expressed by substituting the quantity $(t - x_o\cos\theta - y_o\sin\theta)$ for t in Eq. (3.14). This yields

$$\mathsf{R}[f_s(x,y)] = \frac{2ab\sqrt{b^2\sin^2\theta + a^2\cos^2\theta - (t - x_o\cos\theta - y_o\sin\theta)^2}}{b^2\sin^2\theta + a^2\cos^2\theta}. \tag{3.20}$$

The rotation property can be derived in a similar fashion. We begin by writing the Radon transform in polar form as (Kak and Slaney 1988)

$$\mathsf{R}[f(x,y)] = g(r,\phi) = \int_0^{\pi}\int_{-\infty}^{\infty} f(r,\phi)\delta(r\cos(\theta - \phi) - t)rdrd\phi. \tag{3.21}$$

Rotating the object function by θ_o, we have

$$\bar{g}(r,\phi) = \int_0^{\pi}\int_{-\infty}^{\infty} f(r,\phi + \theta_o)\delta(r\cos(\theta - \phi) - t)rdrd\phi. \tag{3.22}$$

Let $\alpha = \phi + \theta_o$. Then

$$\bar{g}(r,\phi) = \int_0^{\pi}\int_{-\infty}^{\infty} f(r,\alpha)\delta(r\cos(\theta+\theta_o-\alpha)-t)rdrd\phi \quad (3.23)$$

$$= g(r,\theta+\theta_o). \quad (3.24)$$

The Radon transform of the shifted *and* rotated ellipse must be derived with care. The order of application of the translation and rotation properties is important as the rotation takes place about the coordinate origin rather than the ellipse center. One usually wishes to first establish an ellipse orientation and second, translate the oriented ellipse to a desired location. If the operations are performed in reverse, the prototype ellipse is translated to a desired location and then rotated about the *coordinate axis.* In this case, we take the former approach by first substituting $(\theta+\theta_o)$ for θ in Eq. (3.14) and then applying the translation substitution. This yields

$$\mathsf{R}[f_{so}(x,y)] = \frac{2ab\sqrt{b^2\sin^2(\theta+\theta_o)+a^2\cos^2(\theta+\theta_o)-(t-x_o\cos\theta-y_o\sin\theta)^2}}{b^2\sin^2(\theta+\theta_o)+a^2\cos^2(\theta+\theta_o)}. \quad (3.25)$$

3.3 Fan-Beam Conversion

The forward projection model using the Radon transform so far has assumed a parallel beam x-ray source geometry. The type of source considered in this work, however, is a microfocus or point x-ray source in which the x-ray beam spreads out like a fan in any 2-D plane. Thus, the projection model given by Eq. (3.25) must be modified to account for the beam spreading out. The Radon transform can still be used in deriving the projection at any detector position by making a basic, but important observation: Any fan-ray can be thought of as a parallel ray for some other

detector orientation and position. If we can determine this orientation and position, the Radon transform can be computed, yielding the proper projection. Consider the fan-beam geometry shown in Fig. 3.4. The detector has orientation, θ and the fan-ray shown intersects the detector at point $t = t_1$. Line L_R represents the x-ray path orientation used in the conventional Radon transform for that detector position. If we re-orient the detector line by angle β, we have the new detector line, t'. Notice that for this detector orientation, the fan-ray would be the x-ray path for the Radon transform evaluated at $t' = t'_1$. We therefore require that an equivalent detector orientation and position be computed for each fan ray to be used in the Radon transform, yielding the proper projections. For an original detector position, t_1, and orientation, θ, the fan angle, γ is given by

$$\gamma = \tan^{-1} \frac{t_1}{D}, \tag{3.26}$$

where D is the perpendicular source-to-detector distance. The new detector orientation is

$$\beta = \gamma + \theta, \tag{3.27}$$

and the new detector position is

$$t'_1 = t_1 \cos\gamma. \tag{3.28}$$

Applying the detector transformations of Eqs. (3.27) and (3.28) to Eq. (3.25) yield the forward projection model for an arbitrarily oriented and located elliptical flaw with fan-beam source geometry.

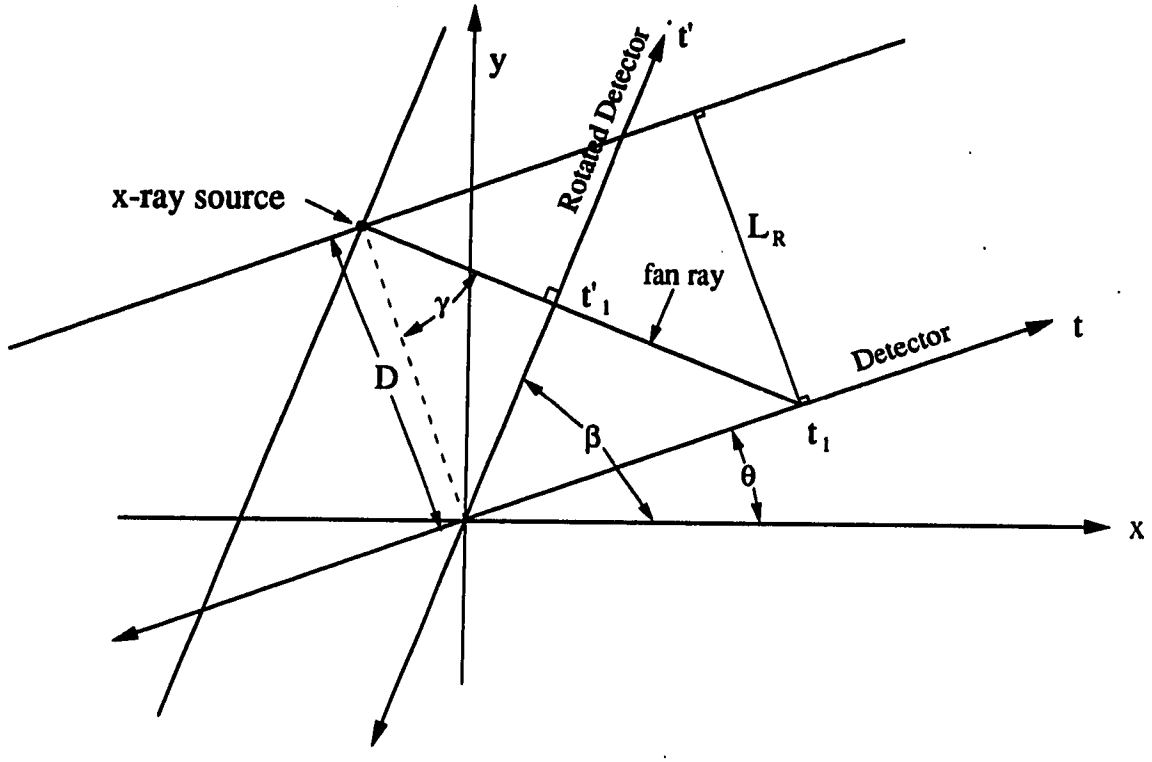

Figure 3.4: Fan-beam x-ray source geometry

$$g(t,\theta) = \left[\frac{4a^2b^2[b^2\sin^2(\gamma+\theta+\theta_o)+a^2\cos^2(\gamma+\theta+\theta_o)]}{[b^2\sin^2(\gamma+\theta+\theta_o)+a^2\cos^2(\gamma+\theta+\theta_o)]^2}\right. \tag{3.29}$$
$$\left. - \frac{4a^2b^2[t\cos\gamma - x_o\cos(\gamma+\theta) - y_o\sin(\gamma+\theta)]^2}{[b^2\sin^2(\gamma+\theta+\theta_o)+a^2\cos^2(\gamma+\theta+\theta_o)]^2}\right]^{\frac{1}{2}}$$

or, replacing γ by $\tan^{-1}\frac{t}{D}$,

$$g(t,\theta) = \left[\frac{4a^2b^2\left[b^2\sin^2[\tan^{-1}(\frac{t}{D})+\theta+\theta_o]+a^2\cos^2[\tan^{-1}(\frac{t}{D})+\theta+\theta_o]\right]}{\left[b^2\sin^2[\tan^{-1}(\frac{t}{D})+\theta+\theta_o]+a^2\cos^2[\tan^{-1}(\frac{t}{D})+\theta+\theta_o]\right]^2}\right.$$
$$\left. - \frac{4a^2b^2\{t\cos\tan^{-1}(\frac{t}{D}) - x_o\cos[\tan^{-1}(\frac{t}{D})+\theta] - y_o\sin[\tan^{-1}(\frac{t}{D})+\theta]\}^2}{\left[b^2\sin^2[\tan^{-1}(\frac{t}{D}+\theta+\theta_o]+a^2\cos^2[\tan^{-1}(\frac{t}{D})+\theta+\theta_o]\right]^2}\right]^{\frac{1}{2}}. \tag{3.30}$$

This model provides a compact, analytical expression for generating projections of ellipses having desired parameters at any arbitrary detector orientation. It also accounts for the fan-beam x-ray source, allowing for the effects of radial divergence of the x-ray beam and magnification to be seen. Example realizations of the forward projection model for various elliptical parameters are shown in Figs. 3.5-3.10. In each figure, the horizontal axis is the detector position and the vertical axis is the projection value, $g(t,\theta)$, given by Eq. (3.30). In Fig. 3.5, the skewness is caused by the offset of the ellipse as well as the nonzero orientation angle. In Fig. 3.6, the skewness is caused by the nonzero orientation angle alone. Figure 3.7 illustrates a symmetrical projection as the offset with respect to the detector origin and the orientation angle are both zero. Figure 3.8 illustrates the effect of magnification. The extent of the projection has increased as the ellipse has moved closer to the

source (y_o=12 as opposed to y_o=10). Figure 3.9 shows the effect of a decrease in magnification as the ellipse has moved away from the source ($y_o = 6$). Figure 3.10 shows the projections plotted together for ease of comparison.

3.4 Reconstruction – Inversion of the Projection Model

Performing the reconstruction of the elliptical flaw model involves the inversion of the forward projection model from the measured projection data. Obtaining projection data from the detector measurements involves using a detector model to convert the detector signal into x-ray intensity. The intensity can then be converted to projection values which are the actual Radon transform values of the ellipse. In this chapter, however, we will assume that the projection values are available for use in the model inversion procedure. The detector models and measurement conversions will be discussed in Chapter 5.

3.4.1 Noiseless Reconstruction

In a noiseless situation in which the model perfectly describes reality, the reconstruction procedure amounts to finding the elliptical parameters which correspond to the measurement data. While this is not the situation in practice, it is useful to simulate in order to understand the complexity of the inversion problem from a numerical standpoint. In the forward projection model, we have 5 unknown parameters, an explanatory variable and two known parameters. The unknown parameters are a, b, x_o, y_o, and θ_o; the known parameters are θ and D, and the explanatory variable is t. For perfect data, the parameters can be computed from five observations. The computation of these parameters is complicated by the fact that the projection

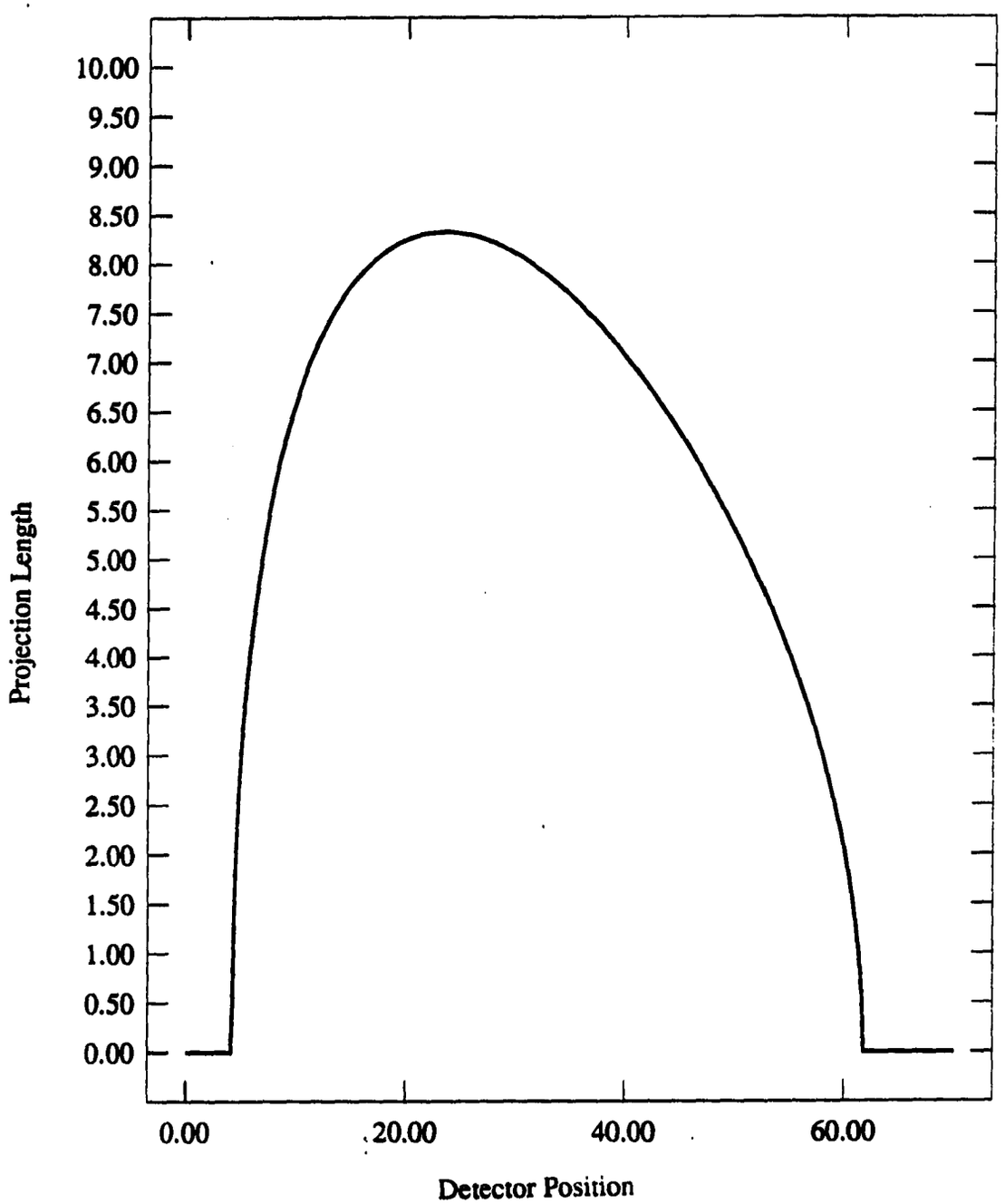

Figure 3.5: **Elliptical projection 1**
$(a = 8 \quad b = 4 \quad x_o = 10 \quad y_o = 10 \quad \theta_o = 0.5 \quad \theta = 0 \quad D = 20)$

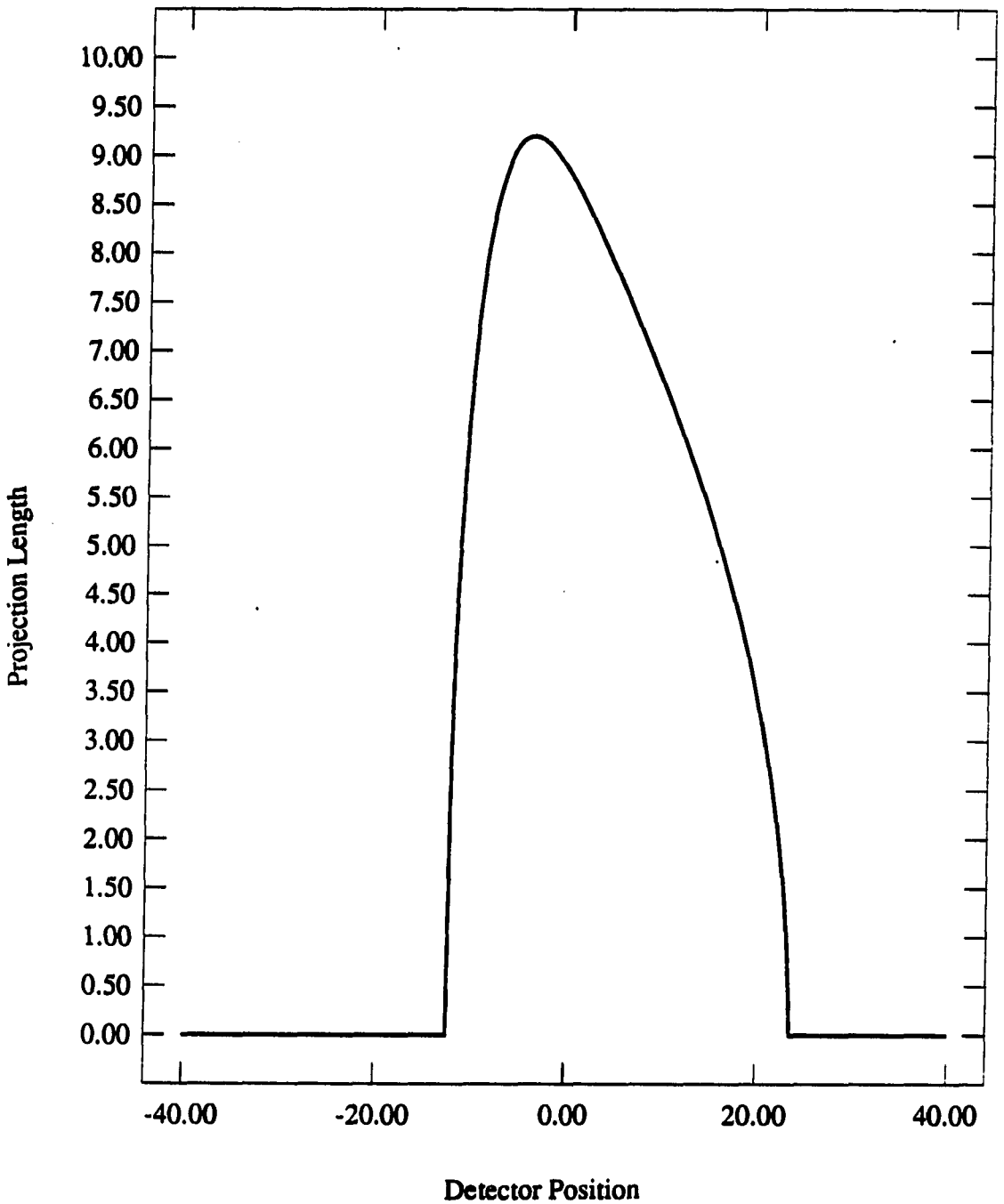

Figure 3.6: Elliptical projection 2
($a = 8$ $b = 4$ $x_O = 0$ $y_O = 10$ $\theta_O = 0.5$ $\theta = 0$ $D = 20$)

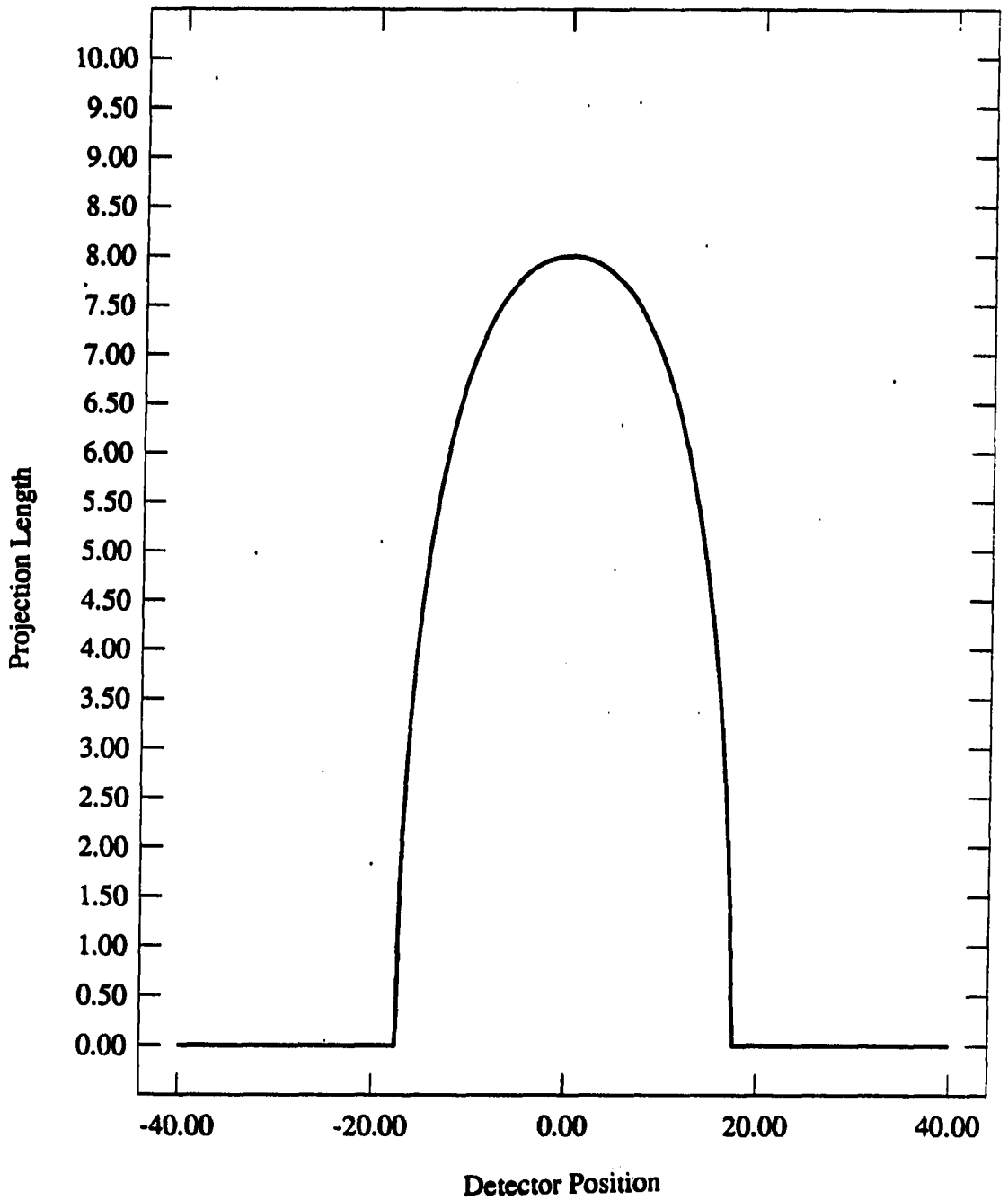

Figure 3.7: Elliptical projection 3
($a = 8$ $b = 4$ $x_o = 0$ $y_o = 10$ $\theta_o = 0$ $\theta = 0$ $D = 20$)

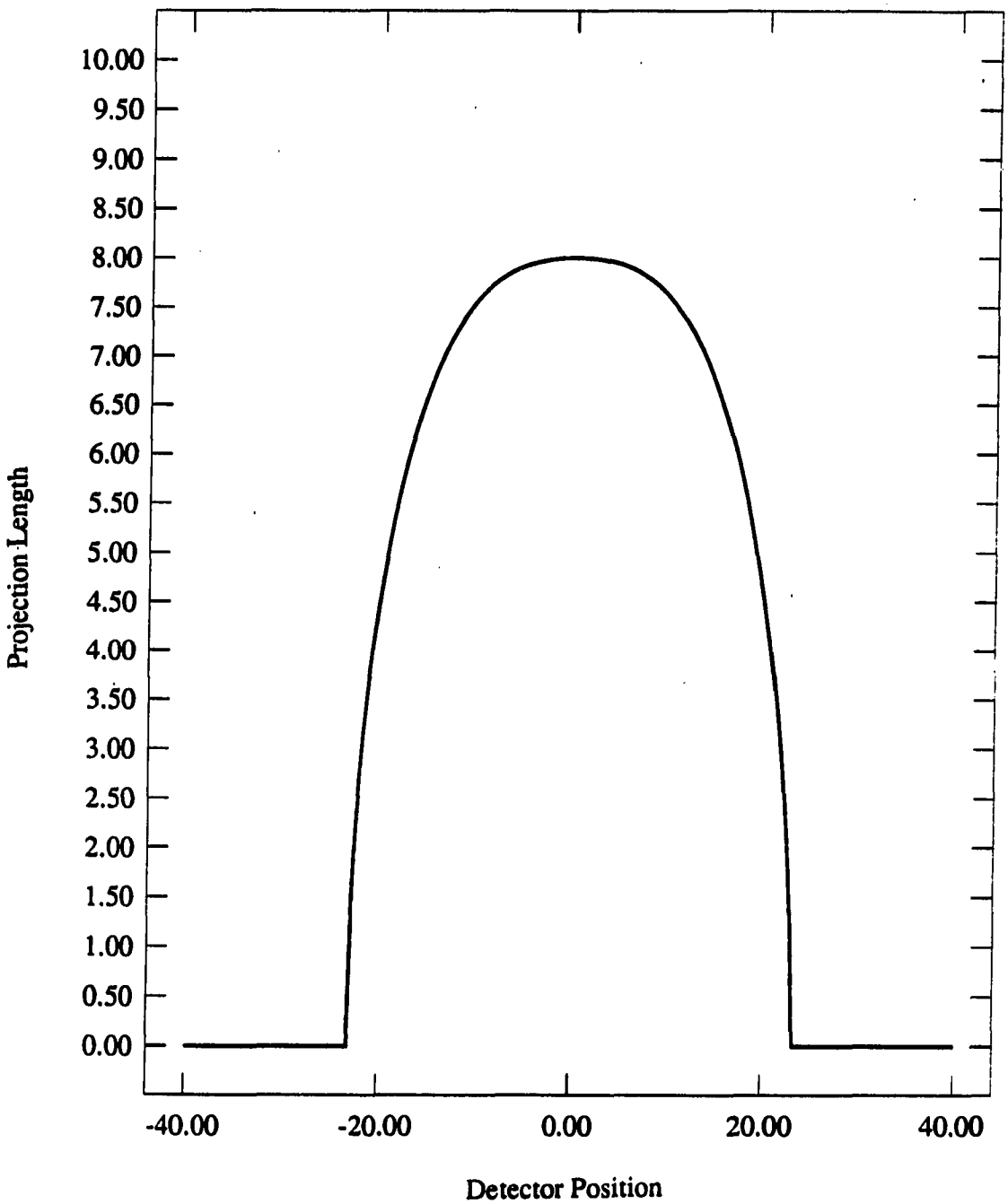

Figure 3.8: Elliptical projection 4
($a = 8$ $b = 4$ $x_o = 0$ $y_o = 12$ $\theta_o = 0$ $\theta = 0$ $D = 20$)

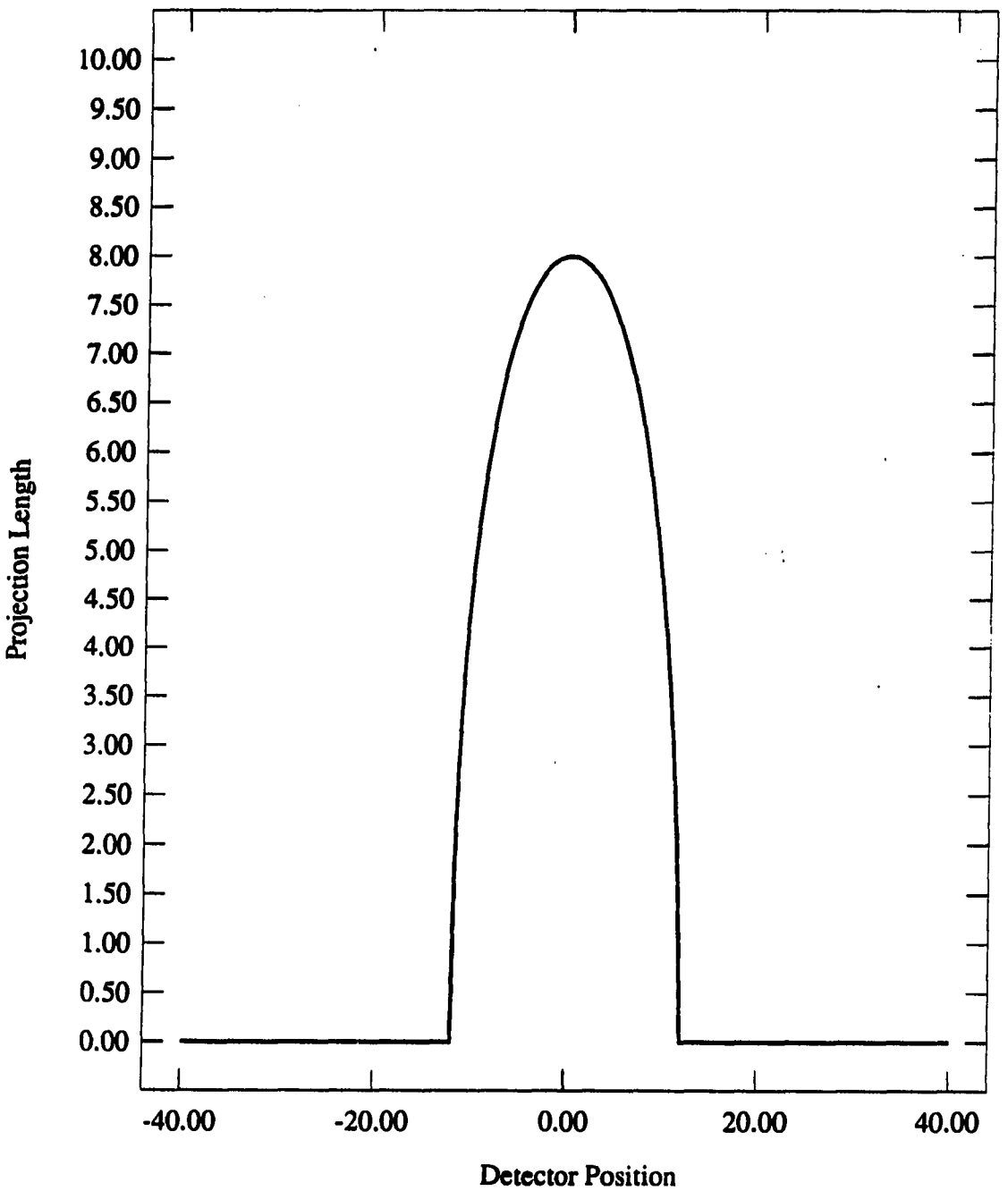

Figure 3.9: Elliptical projection 5
($a = 8$ $b = 4$ $x_O = 0$ $y_O = 6$ $\theta_O = 0$ $\theta = 0$ $D = 20$)

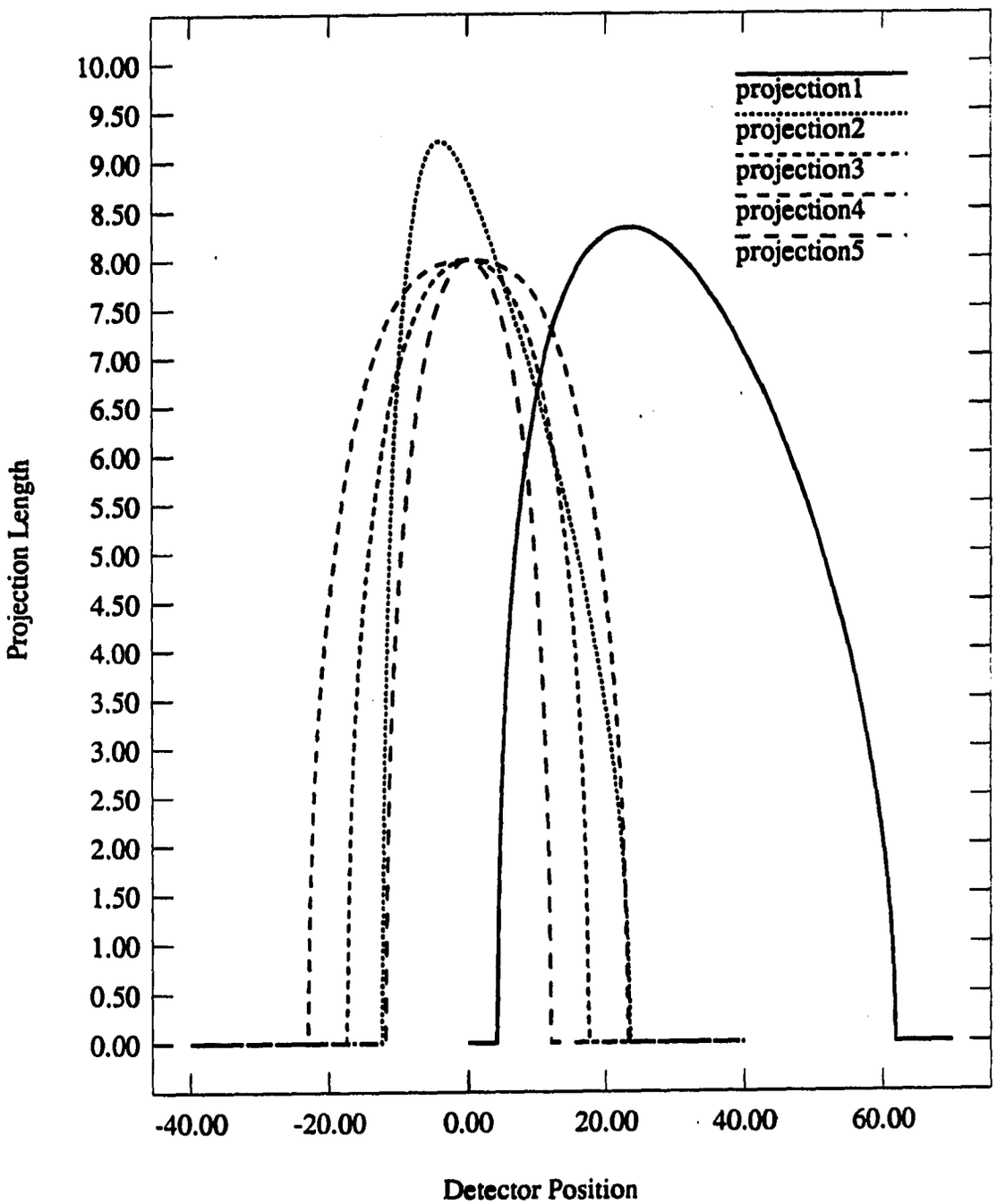

Figure 3.10: All projections plotted together

model is highly nonlinear and there is no good general method for solving systems of nonlinear equations (Press et al. 1988). Solving the system of equations requires the parameter space to be searched for the points satisfying the the model. This can be thought of as setting each equation in the system equal to zero, mapping out all of the zero-contour hypersurfaces for each equation and finding the common point(s) of intersection. For the five-dimensional parameter space here, this is a very difficult prospect unless some a priori knowledge is used to narrow the search. A commonly used method for solving nonlinear systems of equations where a priori information about the parameters is known is the Newton-Raphson iterative method (Press et al. 1988; Gerald and Wheatley 1984). The Newton-Raphson method linearizes the system of equations about a fixed point and computes a correction vector, taking the point closer to the solution to the system.

We will develop this method by letting the vector $\mathbf{x}$ contain the unknown parameter values. For notational convenience, we call these parameters $x_1, x_2, \ldots, x_5$ and define the vector $\mathbf{x}$ as

$$\mathbf{x} = \begin{bmatrix} a \\ b \\ x_o \\ y_o \\ \theta_o \end{bmatrix} = \begin{bmatrix} x_1 \\ x_2 \\ x_3 \\ x_4 \\ x_5 \end{bmatrix}. \tag{3.31}$$

The nonlinear system of equations is written as

$$f_1 = g(t_1, \theta; \mathbf{x}) - p_1(t_1, \theta) = 0$$

$$f_2 = g(t_2, \theta; \mathbf{x}) - p_2(t_2, \theta) = 0$$

$$f_3 = g(t_3, \theta; \mathbf{x}) - p_3(t_3, \theta) = 0 \tag{3.32}$$
$$f_4 = g(t_4, \theta; \mathbf{x}) - p_4(t_4, \theta) = 0$$
$$f_5 = g(t_5, \theta; \mathbf{x}) - p_5(t_5, \theta) = 0$$

where g is the forward projection model equation and $p_i(t_i, \theta)$ is the projection value measured at detector position t_i. The Taylor series for each equation can be generalized as

$$f_i(\mathbf{x} + \delta\mathbf{x}) = f_i(\mathbf{x}) + \sum_{j=1}^{5} \frac{\partial g(\mathbf{x})}{\partial x_j} \delta x_j + O(\delta\mathbf{x}^2), \tag{3.33}$$

so that

$$f_i(\mathbf{x}) + \sum_{j=1}^{5} \frac{\partial f_i(\mathbf{x})}{\partial x_j} \delta x_j \approx 0. \tag{3.34}$$

The correction vector, $\delta\mathbf{x}$ is computed by solving the linear system

$$p(t_i, \theta) - g_i(t_i, \theta; \mathbf{x}) = \sum_{j=1}^{5} \frac{\partial g(\mathbf{x})}{\partial x_j} \delta x_j \tag{3.35}$$

The solution will either converge to a set of parameters based on some convergence criterion or not converge if no solution exists nearby. The solution after convergence in general is not unique. There are situations where a permutation of the parameters yields a root of the system, as will be discussed later. However, it is believed that with the exception of cases of permuted parameters and physically unrealizable parameters (such as negative axes lengths), the solution is unique. This previous statement is made from experience only with no mathematical proof, although it would be useful to investigate the uniqueness in future research.

Applying the Newton-Raphson method to the inversion of Eq. (3.30), the partial derivatives are evaluated analytically and specific values are computed at each iteration by substituting the current parameter vector into the analytical expressions

Table 3.1: Convergence summary of simulated reconstruction

iteration	a	b	x_o	y_o	θ_o
initial	1.10	1.90	5.90	0.00	0.40
1	1.74	1.70	0.07	4.00	0.74
2	2.02	1.94	0.05	3.76	-7.12
3	1.87	1.86	0.04	4.33	-4.27
4	1.64	1.91	0.07	4.68	9.78
5	1.76	1.62	0.09	4.91	10.3
6	1.83	1.79	0.01	4.74	8.81
7	1.91	1.74	-0.04	4.71	13.6
8	1.73	1.82	-0.06	4.82	12.5
9	1.85	1.50	-0.04	4.94	12.2
10	2.28	1.59	-0.09	4.27	12.8
11	2.50	1.54	0.07	3.89	12.5
12	2.51	1.50	-0.01	3.96	12.6
13	2.50	1.50	0.00	4.00	12.6

for the derivatives. The complicated nature of Eq. (3.30) makes the program rather complex as there are many applications of the chain, product, and quotient rules in deriving the derivatives. The method was implemented and tested with a simulated elliptical projection. The ellipse used for the projection had the parameters, $a = 2.5$, $b = 1.5$, $x_o = 0.0$, $y_o = 4.5$, $\theta_o = 0.0$, with $D = 8.0$ and $\theta = 0.0$. Table 3.1 summarizes the iteration process to the correct solution starting with the initial guess of $a = 1.1$, $b = 1.9$, $x_o = 0.3$, $y_o = 5.9$, $\theta_o = 0.4$.

A plot illustrating the convergence properties graphically is shown in Fig. 3.11. Notice that the final value for θ_o is the proper value because of a 4π bias. This brings to light an interesting situation. In the parameter space there is no unique solution to the system of equations. This is due to the periodic nature of the trigonometric

functions as well as cases of equivalent ellipses with different parameters. One obvious example of this case is ($a = 2$, $b = 1$, $\theta = 0$) and ($a = 1$, $b = 2$, $\theta = \pi/2$). We need not concern ourselves with this problem because with either solution, the ellipsoid is equivalently described.

The previous exercise in inverting the forward projection model was motivated by an interest in the numerical difficulties associated with the inversion of such a complicated nonlinear system of equations. Other numerical tests have been run in which the solution vector does not converge. One of the major causes of nonconvergence is the choice of initial values that are grossly inconsistent with the measurement data. For instance, when the routine is run with initial values that produce a zero projection value at every measurement location, the parameter vector wanders aimlessly during the iteration process. In this simulation, it was found that the y_O initial value was very critical. An initial value greater than 5.9 or less than 3.0 caused nonconvergence. A related problem is the fact that the iteration process can take the parameter vector outside its region of support. In this situation, the projection model is undefined for a given set of parameters and measurement location. This occurs when the quantities under the radical sign of Eq. (3.30) become negative. This problem can sometimes be overcome by setting the model equal to zero. Other times, convergence will not be reached.

The key to convergence is to use initial estimates that are sufficiently close to the true values and that are somewhat consistent with the measurement data. A good rule of thumb is that the initial values should be within $\pm 50\%$ of the true value. This is a realistic goal because experience and a priori knowledge of the measurement geometry can allow meaningful initial values to be calculated.

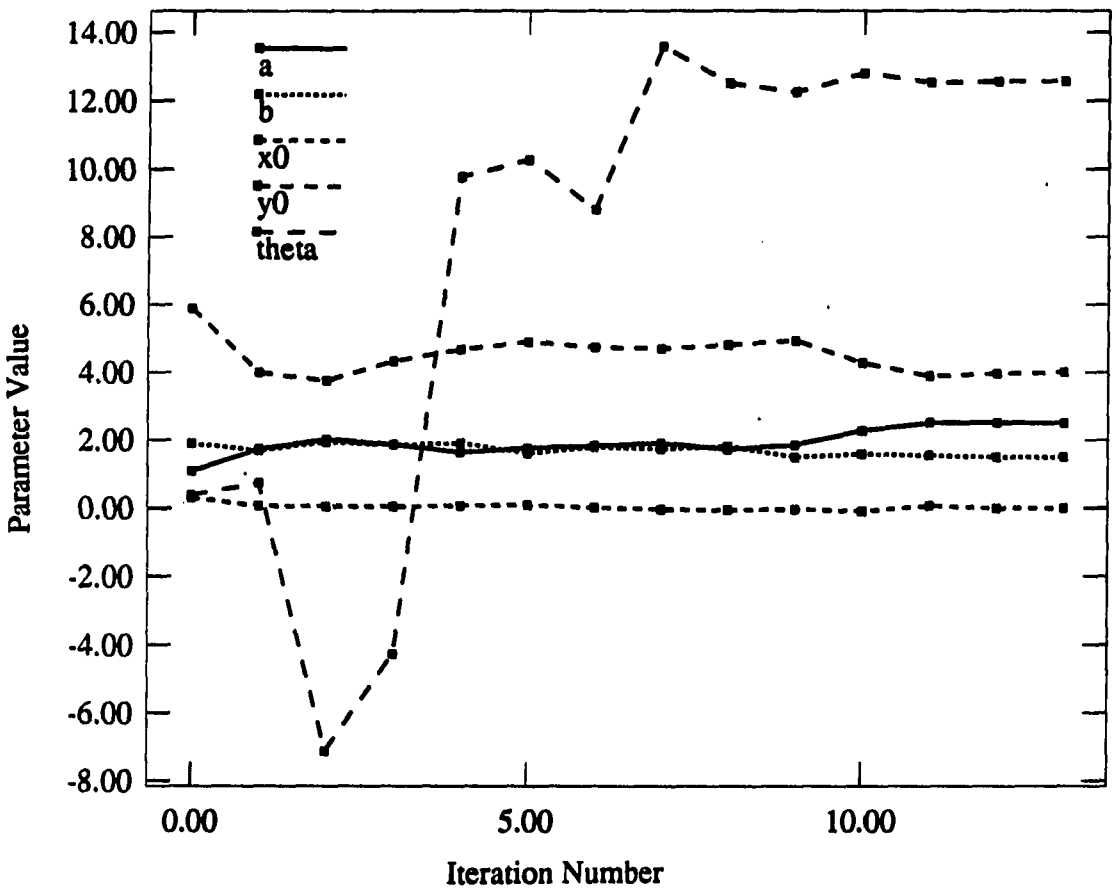

Figure 3.11: Graphical illustration of convergence properties

The major goal of the previous section has been to show that the forward projection model of Eq. (3.30) is invertible, given noiseless measurement data and initial values that are sufficiently close to the true values. In the next section, we consider noisy projection data and apply least-squares parameter estimators to the problem.

3.4.2 Reconstruction Using Noisy Data

In the real world, all measurement data contains noise. Noise is caused by many different processes and is defined as any component of the signal not capable of being described deterministically. Among the sources of noise are the x-ray generation itself, the noise in the x-ray photon interaction with the object under test, noise in the detector, noise in the digitization process, and noise in the measurement process. In this section we assume noise processes consisting of additive Gaussian noise, multiplicative signal-dependent noise from a Gaussian distribution and Poisson counting noise. The additive Gaussian noise is used for simulation purposes and the multiplicative and Poisson noise processes are used to model the film grain noise and the x-ray generator noise, respectively (Kuan et al. 1985).

The reconstruction problem in the presence of noisy measurement data amounts to finding the *best* set of ellipse parameters that satisfy the system of model equations. The term *best* refers to those parameters which minimize the total squared error between the predicted and measured projections. We rewrite the system of projection equations as

$$p_i(t_i, \theta) = h_i(t_i, \theta) + u_i(t_i, \theta) \tag{3.36}$$

where p is the measured projection, h is the *true* projection, and u is an error term. The term *best* is used because there are an infinite number of possible parameter

vectors which satisfy Eq. (3.36), depending upon $(u_1,\ldots,u_N)$. The least-squares estimator finds the parameter vector which minimizes $\|u\|^2$. When u is distributed NI(0,Σ_{uu}), then the least squares estimator is the maximum likelihood estimator (Fuller 1987). The error term in Eq. (3.36) is not necessarily Gaussian distributed or even random. It could be deterministic if there is some systematic measurement error or modeling error. Given that we can't tell for sure the distribution or cause of u, it still makes sense to minimize it, and because of the convenience of the least squares method, we apply it knowing that it is probably not optimal.

Computing the nonlinear least squares solution is very similar to finding the common roots of the model equations in the Newton-Raphson method. In this case, we simultaneously find the roots of an overdetermined system of the derivatives of merit functions. In least squares, the merit function is

$$\chi^2(\mathbf{x}) = \sum_{i=1}^{N} \left[\frac{p_i - g(t_i,\mathbf{x})}{\sigma_i}\right]^2, \tag{3.37}$$

where $\mathbf{x}$ is the parameter vector, p_i is the measured projection, g is the model-predicted projection, and σ_i is the standard deviation of the i*th* measurement, taken from the diagonal of Σ_{uu}. Minimizing Eq. (3.37) is equivalent to finding the roots of its first derivatives. This being a nonlinear problem, we make the approximation that χ^2 can be approximated by a quadratic surface sufficiently close to the roots (Press et al. 1988). We write

$$\chi^2(\mathbf{x}+\delta\mathbf{x}) \approx c + \mathbf{d}\cdot\delta\mathbf{x} + \frac{1}{2}\delta\mathbf{x}\cdot\mathbf{H}\cdot\delta\mathbf{x} \tag{3.38}$$

where

$$c = \chi^2(\mathbf{x}) \tag{3.39}$$

$$\mathbf{d} = \frac{\partial \chi^2(\mathbf{x})}{\partial x_i} \quad i = 1, \ldots, 5 \tag{3.40}$$

$$\mathbf{H} = \frac{\partial^2 \chi(\mathbf{x})^2}{\partial x_i \partial x_j} \quad i = 1, \ldots, 5 \; ; \; j = 1, \ldots, 5. \tag{3.41}$$

Minimizing (3.38) with respect to $\delta\mathbf{x}$ yields

$$\mathbf{0} = \mathbf{d} + \mathbf{H} \cdot \delta\mathbf{x} \tag{3.42}$$

or

$$\mathbf{H} \cdot \delta\mathbf{x} = -\mathbf{d}. \tag{3.43}$$

This can be written as the following system of linear equations:

$$\sum_{j=1}^{5} \frac{\partial^2 \chi(\mathbf{x})^2}{\partial x_i \partial x_j} \delta x_j = -\frac{\partial \chi^2(\mathbf{x})}{\partial x_i} \quad i = 1, \ldots, 5. \tag{3.44}$$

The solution, $\delta\mathbf{x}$ is added on to the current value of $\mathbf{x}$ at each iteration until convergence is reached. This method is known as the inverse Hessian method and is primarily used only when Eq. (3.37) is well approximated locally by a quadratic surface.

A method of minimizing χ^2 where the function does not locally approximate a quadratic surface is the steepest descent method (Press et al. 1988). In this algorithm, we take a series of steps down the gradient of the merit function, each time adding a correction vector to the current parameter vector:

$$\mathbf{x} = \mathbf{x} - \delta\mathbf{x} \tag{3.45}$$

where the components of the correction vector are

$$\delta x_i = k_i (\nabla \chi^2)_i = k_i \frac{\partial \chi^2(\mathbf{x})}{\partial x_i} \tag{3.46}$$

The minimization technique implemented in this dissertation is the Marquardt method (Marquardt 1963; Pankratz 1983; Press et al. 1988). This method compromises between the two methods previously discussed. It combines the best features of the inverse Hessian and steepest descent methods depending how well the merit function is approximated by a quadratic surface. Marquardt established logical method of computing a value for k_i in the steepest descent method as well as a way of switching smoothly between the two methods during the iteration process. The constant used in the gradient method is selected to be

$$k_i = \frac{1}{\lambda H_{ii}} \tag{3.47}$$

where H_{ii} is the ith diagonal component of the Hessian matrix, $\mathbf{H}$ and λ is a constant. The two methods are combined by defining a new Hessian matrix given by

$$H'_{ii} = H_{ii}(1+\lambda) \tag{3.48}$$

$$H'_{ij} = H_{ij} \quad (i \neq j). \tag{3.49}$$

The value of λ determines which method is being used in the search for the optimum $\mathbf{x}$. From (3.44) we have the linear system of equations

$$\sum_{j=1}^{5} H'_{ij}\delta x_j = \frac{\partial \chi^2(\mathbf{x})}{\partial x_i} \quad i = 1,\ldots,5. \tag{3.50}$$

We see that when λ is large, the matrix, $\mathbf{H}'$ is diagonally dominant with the diagonal term approximately equal to $1/k_i$, enforcing the steepest descent method. When λ is small, the method defaults to the inverse Hessian method. The value of lambda is chosen based upon a comparison of the residual error with that of the previous step. If the residual error goes up, λ is increased by a factor of 10 and the correction vector

is recomputed. If the residual error goes down, λ is reduced by a factor of 10 and the correction vector is applied to the current parameter vector (Press et al. 1988). This iteration process is repeated until convergence is reached. Convergence is difficult to guarantee with this method, even though it is extremely efficient at finding the optimal value very quickly. As with all nonlinear search algorithms, convergence depends heavily on the initial value selection.

The method has been tested with several sets of noisy simulated data. Again, it requires initial estimates which are reasonably close to the true values for convergence. In addition, there can be problems with the solution causing an inconsistency between the region of support and the measurement data. These problems will be discussed in the next section. Figure 3.12 shows a simulated noisy projection of an ellipse having parameters, (a=2.50, b=1.50, x_O=0.00, y_O=4.00, θ_O=0.30), and detector parameters, D=8.00, θ=0.00. The noise used was from the distribution NI(0,0.02) and was additive. The Marquardt nonlinear optimization technique was run on this data set of 200 projection values using initial parameters, (a=1.00, b=0.50, x_O=0.50, y_O=5.50, θ_O=0.00). After 12 iterations, the routine converged to the parameters (a=2.41, b=1.50, x_O=0.00, y_O=4.16, θ_O=0.33) with a χ^2 value of 191.0 and a residual error of 0.02. A graphical plot of the noisy data with the projection of the solution parameters and the initial parameters is shown is Fig. 3.13. The smaller dashed curve represents the projection of the initial parameters. The dotted curve represents the measurements, and the solid curve is the projection of the optimally fit parameters. The convergence properties of the reconstruction are shown in Fig. 3.14. Each line in Fig. (3.14) plots the parameter value versus the iteration number. All of the parameters are fairly stable in the convergence process with the exception of θ. The

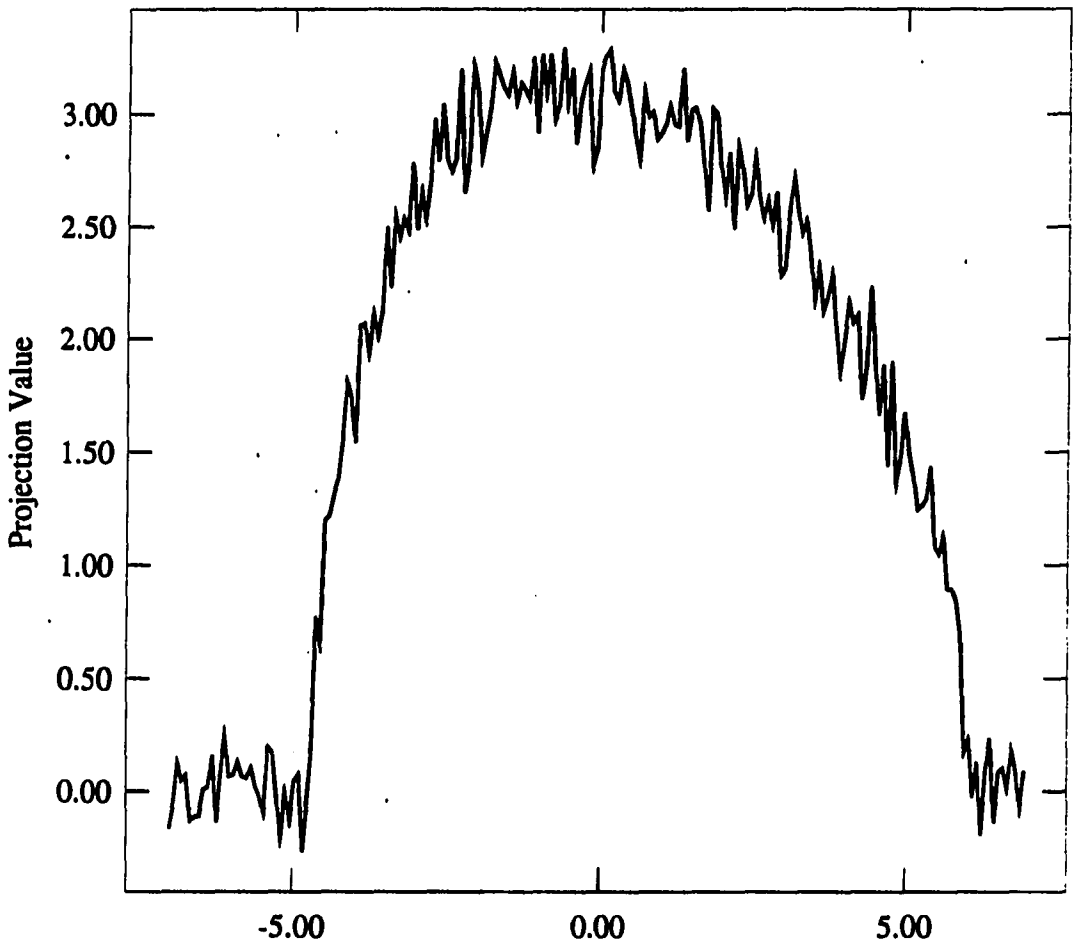

Figure 3.12: Plot of elliptical projection with Gaussian noise added

θ parameter tends to jump around due to its periodicity. This can be avoided simply by performing a modulo π.

When the measurement errors are normally distributed, the uncertainties of the parameters can be found by examining the parameter covariance matrix. The matrix is computed as (Press et al. 1988)

$$\mathbf{C} = \frac{1}{2}\mathbf{H}^{-1}. \tag{3.51}$$

The estimated standard errors of the parameters, obtained from the diagonal ele-

ments of the covariance matrix were (σ_a=0.124, σ_b=0.001, σ_{x_o}=0.001, σ_{y_o}=0.301, σ_{θ_o}=0.006).

The goodness of fit for the model can be assessed by through the chi-square goodness of fit test. The tail probability of the chi-square distribution with 195 degrees of freedom and a variate of 191.0 (the value of χ^2 from the optimization) is 0.568 indicating a good fit of the model. The $(1-P)x100\%$ confidence interval for each parameter can be computed as (Press et al. 1988)

$$CI_{x_i} = x_i \pm \sqrt{\Delta\chi^2_\nu}\sigma_{x_i} \tag{3.52}$$

where ν is the number of degrees of freedom (here $\nu = 5$) and $\Delta\chi^2_\nu$ is the variate from the χ^2_ν distribution with 1-P tail probability. The value of $\Delta\chi^2_\nu$ can also be thought of as the allowable change in χ^2_ν which would encompass 95% of all realizations of that parameter from estimations using the distribution of measurements. For ν = 5 df, $\Delta\chi^2_\nu = 11.1$. Thus for this simulation, the 95% confidence intervals for the parameters are:

$$CI_a = 2.41 \pm 0.41$$

$$CI_b = 1.50 \pm 0.00$$

$$CI_{x_o} = 0.00 \pm 0.00$$

$$CI_{y_o} = 4.16 \pm 1.00$$

$$CI_{\theta_o} = 0.33 \pm 0.02$$

The interpretation of the covariance matrix as uncertainties on the parameters breaks down in the case of nonnormal measurement errors. Because the measurement

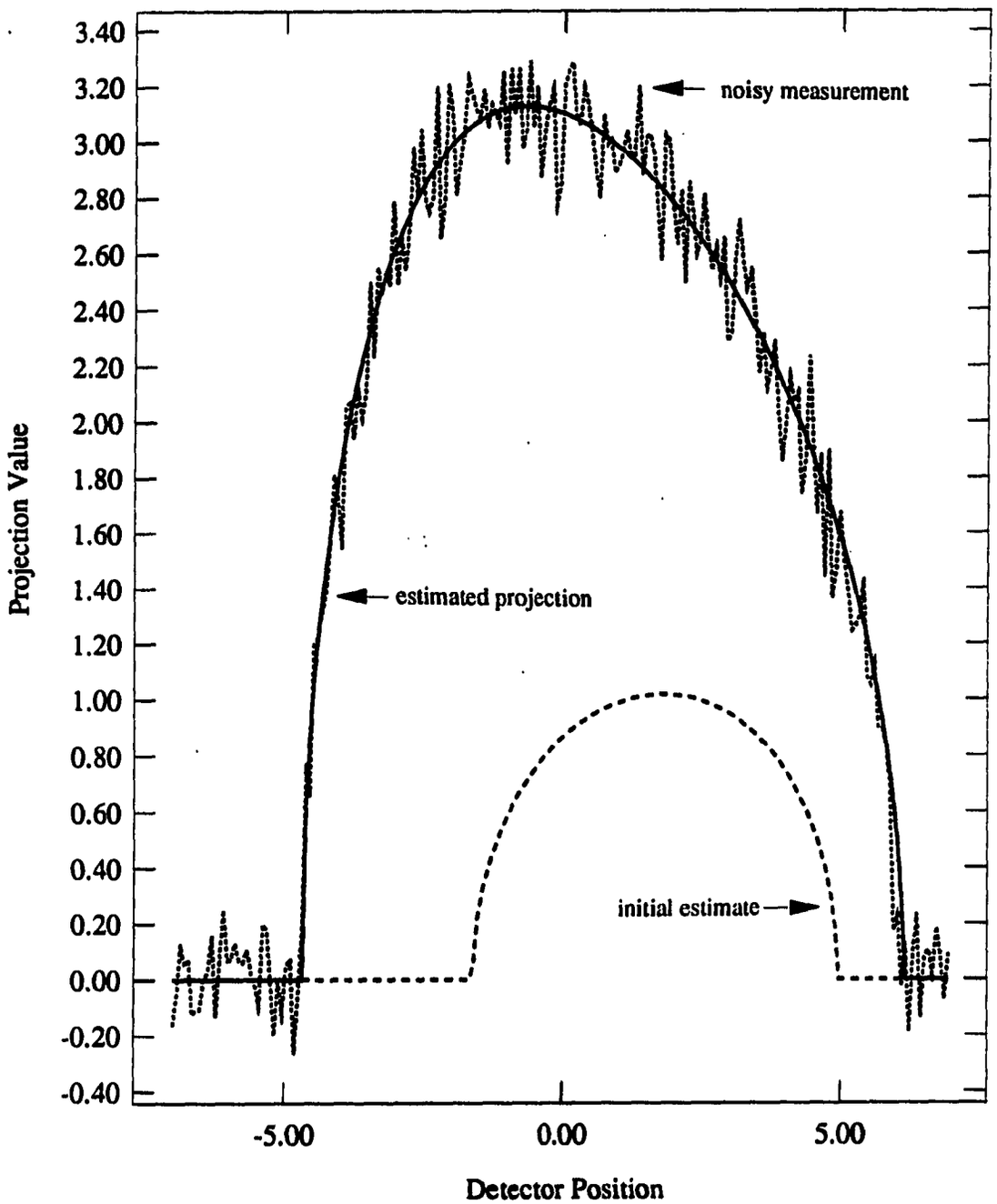

Figure 3.13: Simulated reconstruction of ellipse

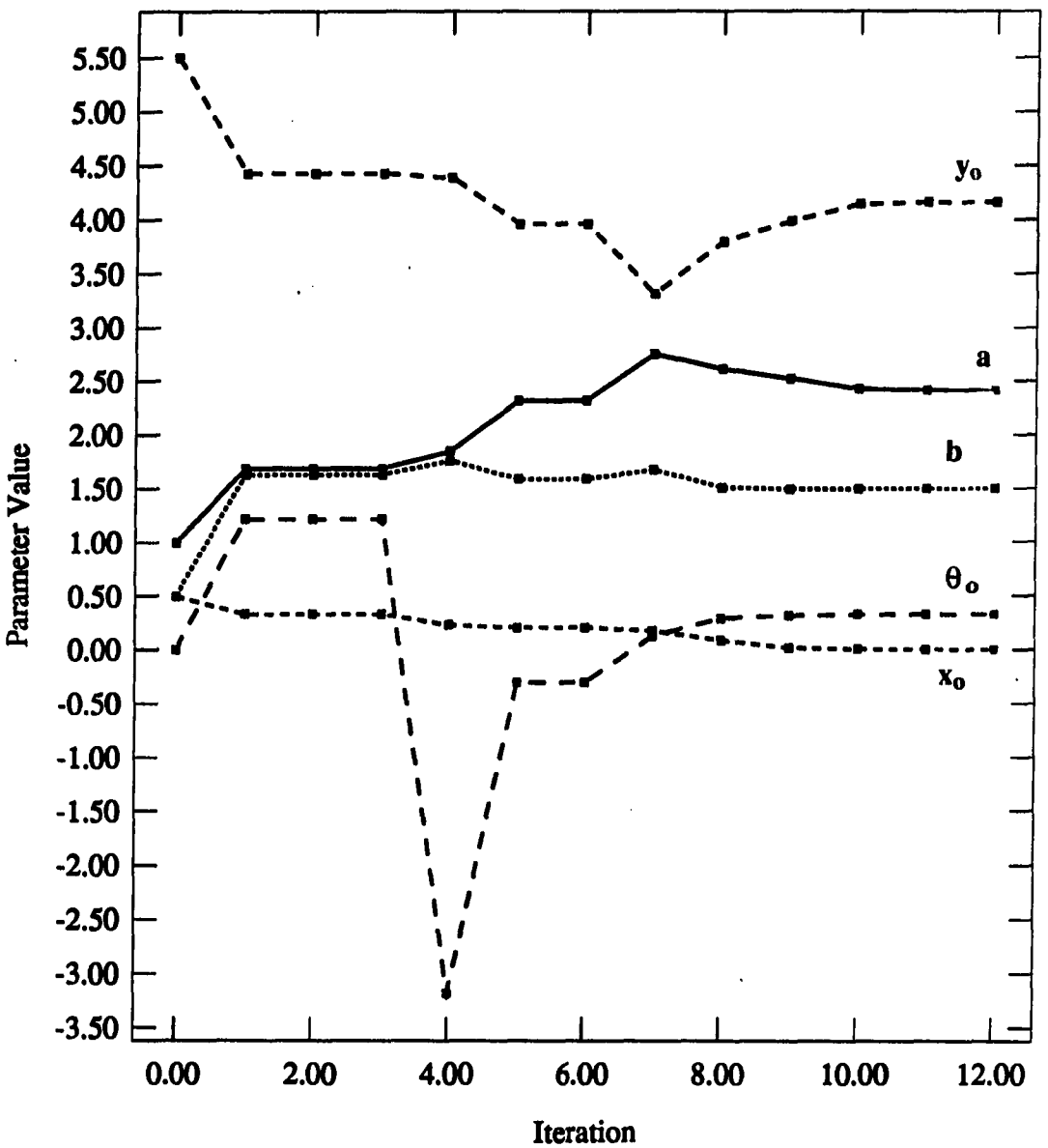

Figure 3.14: Convergence properties of simulated reconstruction

errors in reality are not normal, one way of computing confidence intervals for the parameters is by Monte-Carlo simulation. This method uses multiple estimations from different sample realizations (from the known measurement noise statistics) of the measurements. Each sample realization is generated using the estimated parameters as nominal values and a noise process using random number generators. The distribution of parameters is then plotted as a histogram or scatter plot and the variability is used to find a confidence interval. This analysis is only valid when the data fits the model well. The model fit is evaluated in a similar manner by comparing the nominal χ^2 value to the distribution of χ^2 values from the Monte-Carlo simulation. (Note: χ^2 is not distributed as a chi-square statistic. We call it "x squared".) If the nominal χ^2 value is not way out in the tail of the distribution, the model is deemed adequate.

This type of Monte-Carlo simulation has been performed for the case of a combination of multiplicative, signal dependent Gaussian noise and Poisson noise. In this case, the covariance matrix does not have any absolute meaning as to the uncertainties of the various parameters. One could, however, in principle derive estimates of the parameter variances by writing the likelihood function for the measurements with this type of noise. This type of analytical solution is not practical, however, because of the complicated nature of the noise processes. Even the simple propagation of errors formula cannot be used in estimating the change in a parameter caused by measurement errors because an analytic expression for the parameters as a function of the measurements does not exist. For 250 sample measurement realizations with the above noise distributions, the parameter distributions are shown in Figs. 3.15-3.19 in both histogram and scatter plot form. These figures show the variability

of the estimated parameters caused by variability in the measurement data. In each figure, the appropriate parameter is plotted against the value of χ^2 obtained from the estimation. In addition, the corresponding histogram of the appropriate parameter is shown. The nominal parameter values were ($a = 2.40$, $b = 1.50$, $x_o = 0.00$, $y_o = 4.16$, $\theta_o = 0.32$) and were obtained from an initial estimate of a simulated noisy data set having true parameters ($a = 2.50$, $b = 1.50$, $x_o = 0.00$, $y_o = 4.00$, $\theta_o = 0.30$). Signal dependent multiplicative noise $f(i)u(i)$ was added to the data, where $u(i)$ was taken from an NI(0,0.05) distribution. The relation between the observed value, $p(i)$, and the true value, $f(i)$ is given by

$$p(i) = f(i) + f(i) \cdot u(i)^{\frac{1}{3}}, \tag{3.53}$$

This type of process is useful in modeling the film grain noise associated with a film detector (Kuan et al. 1985). The value, $p(i)$ was then used in a Poisson distribution with mean $p(i)$ to generate the simulated measurement. The distribution of the Poisson process is given by

$$Q_k = \frac{\{\lambda p(i)\}^k e^{-\lambda p(i)}}{k!}, \tag{3.54}$$

where Q_k is the probability of the emission of k photons in a specified time interval and $p(i)$ is the average number of photons emitted in that interval (Macovski 1983). A scaling factor, λ, of 0.2 was used in the Poisson process to control the noise level. A standard random number generator was used to pick variates from the process (Press et al. 1988).

The nominal value for χ^2 was 35.5 which is well within the distribution of χ^2 shown in Fig. 3.20 (as it should be). The 95% confidence intervals were computed

by bounding the plots to include 238 of the parameter values while excluding 12 or 6 on each side. The confidence intervals are:

$$a = (2.15, 2.65)$$

$$b = (1.49, 1.51)$$

$$x_o = (-0.01, 0.008)$$

$$y_o = (3.75, 4.55)$$

$$\theta_o = (0.27, 0.38)$$

3.5 Numerical Difficulties

There are two basic difficulties associated with the numerical estimation of the elliptical parameters. They are the selection of initial values for the parameters and the inconsistency between the region of support and the measurement data. As with most nonlinear iterative methods, initial value selection is crucial to the performance. If the initial values are not selected sufficiently close to the solution, the routine may not converge or it may converge to some other undesirable locally optimum value. Fortunately, with x-ray projections, initial parameter values can be estimated based on knowledge of the inspection geometry as well as measurement pre-processing. The inspection geometry determines which parameters values are impossible or unimportant. For example, if the extent of the part under test in the y direction is 10 cm to 15 cm, it would be foolish to choose and initial value of y_o to be 20 cm. In addition, knowledge of the expected flaw sizes can help constrain the initial values of a and b. This type of knowledge can also be used to constrain the

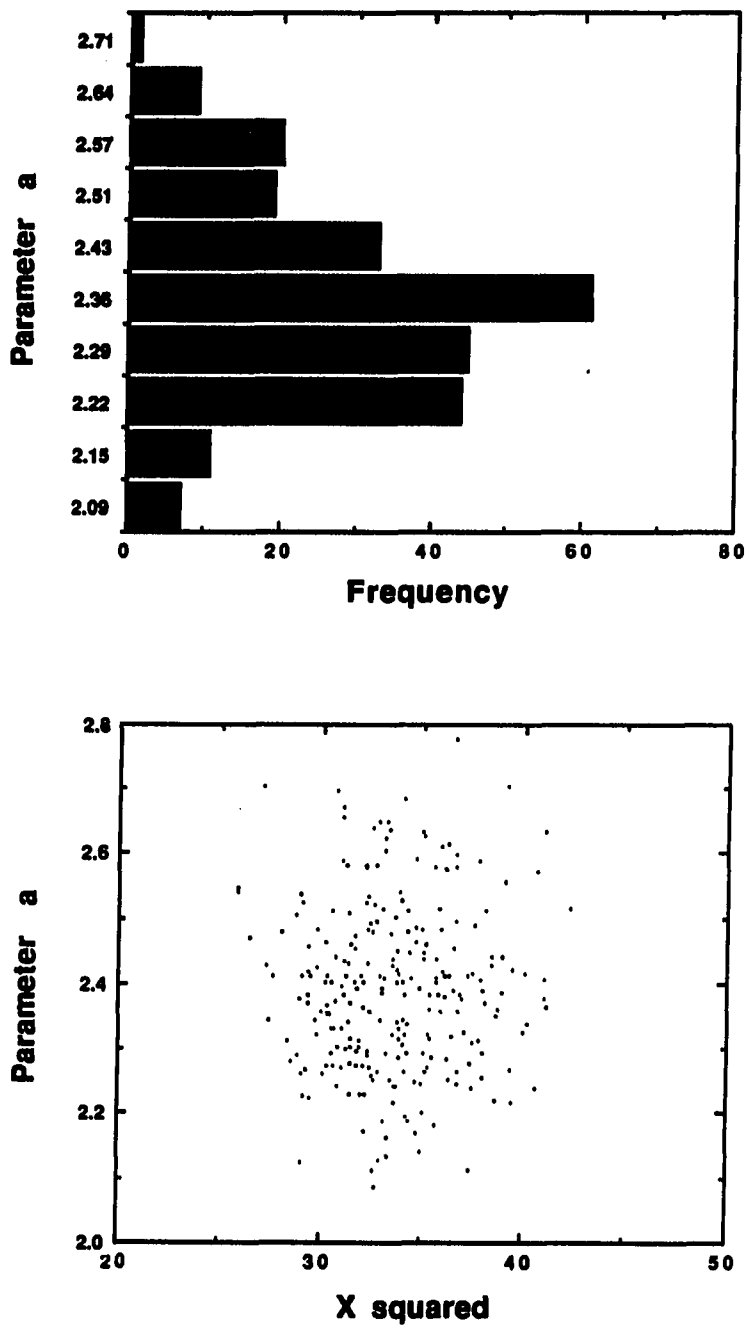

Figure 3.15: Histogram and scatter plot of a from 250 sample realizations

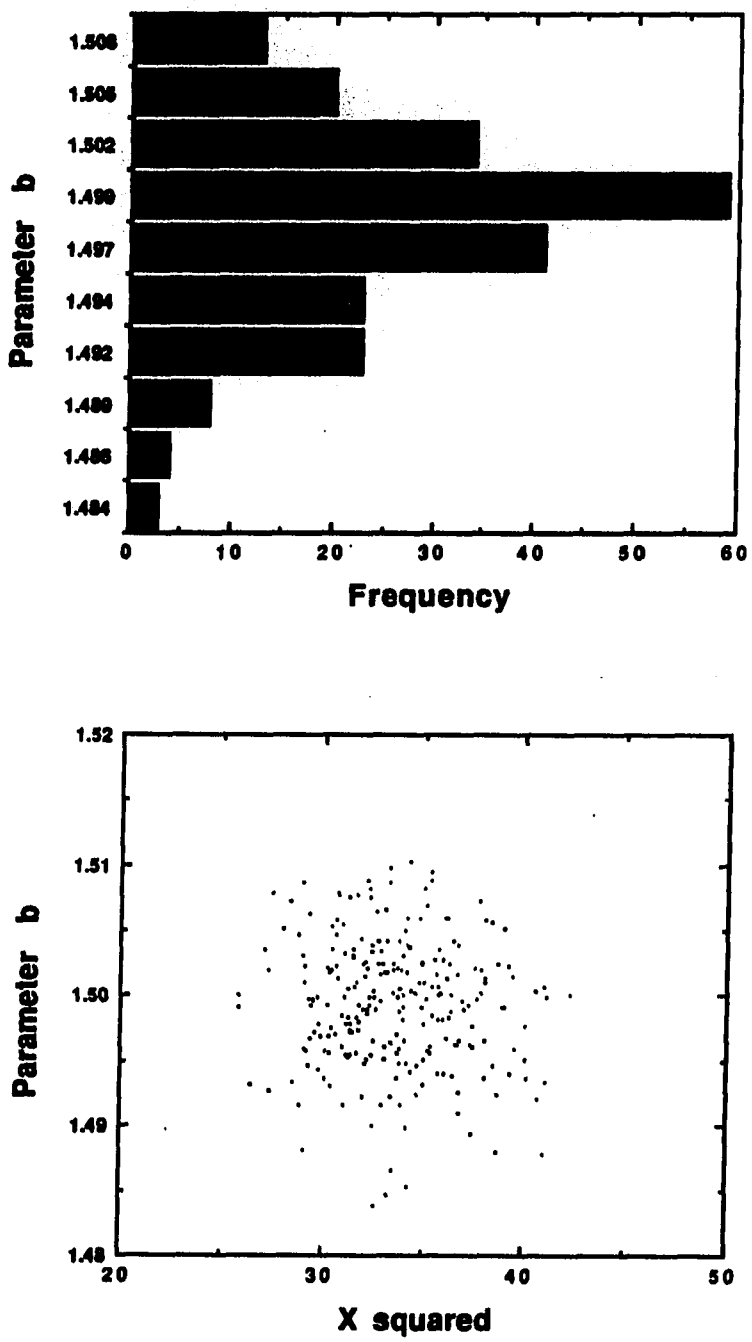

Figure 3.16: Histogram and scatter plot of b from 250 sample realizations

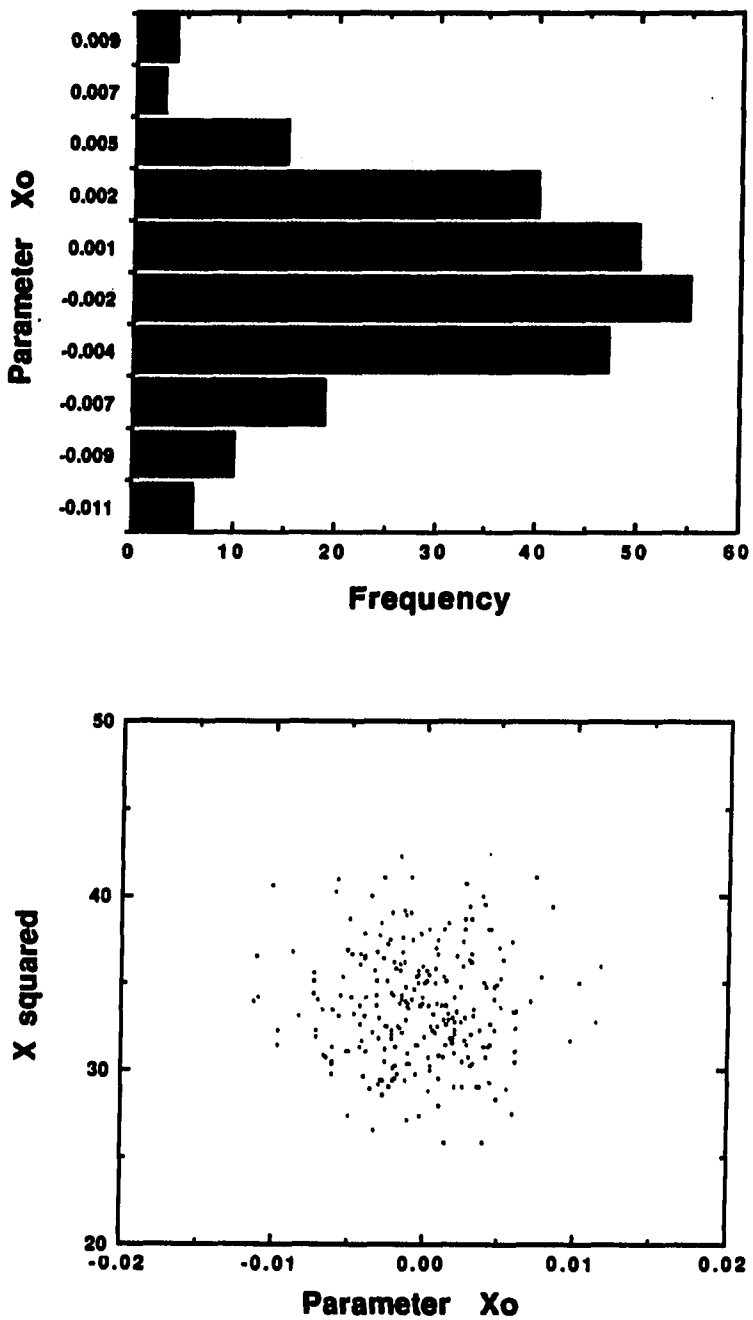

Figure 3.17: Histogram and scatter plot of x_o from 250 sample realizations

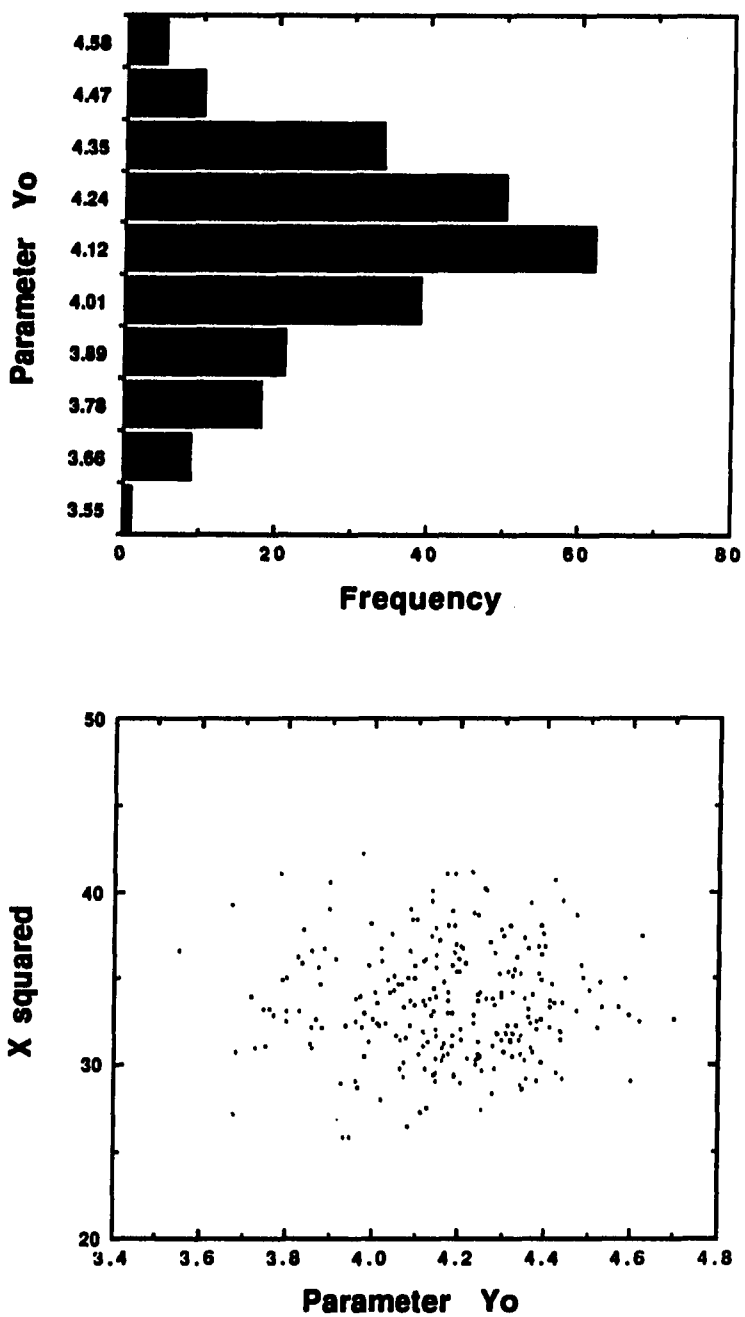

Figure 3.18: Histogram and scatter plot of y_o from 250 sample realizations

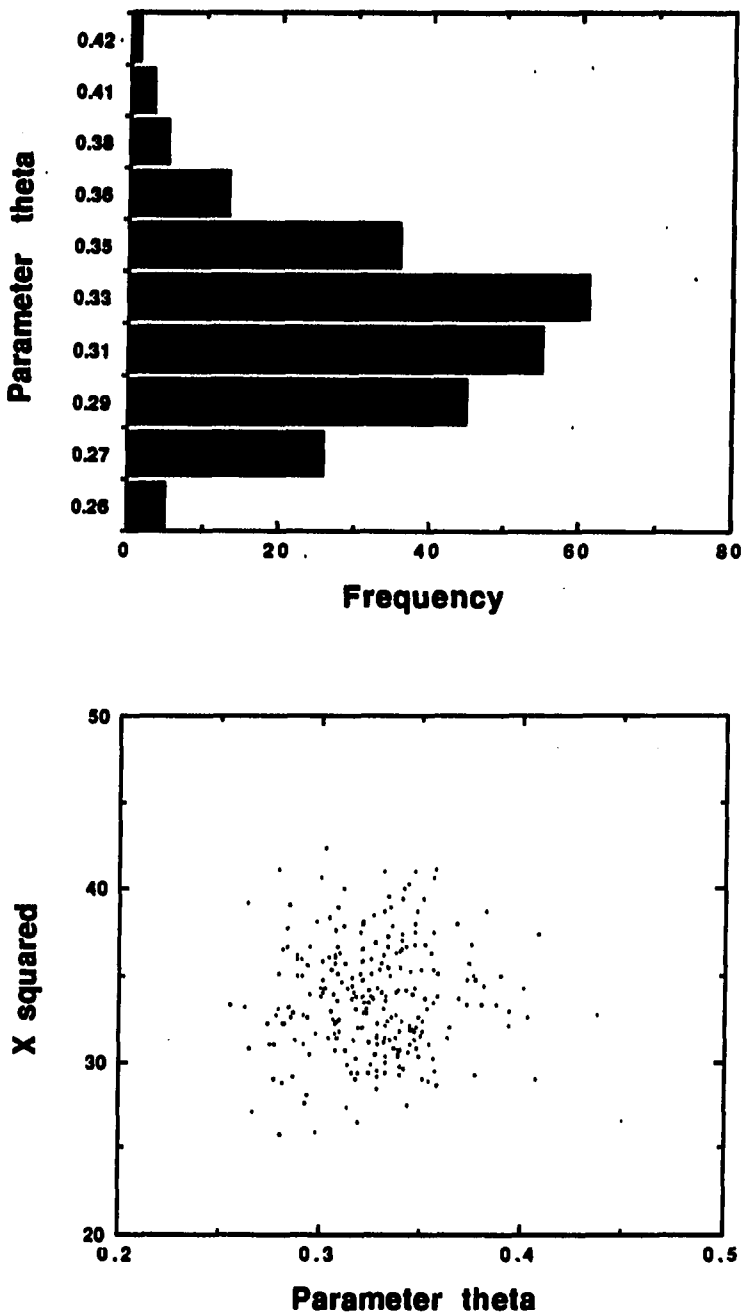

Figure 3.19: Histogram and scatter plot of θ_0 from 250 sample realizations

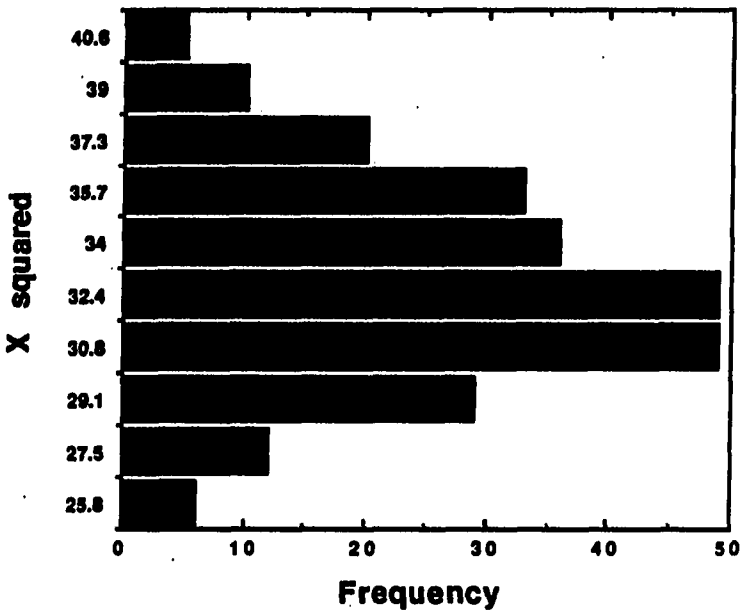

Figure 3.20: Distribution of the merit function for 250 sample realizations

parameters during the iteration process.

A good method for initial value selection is the use of measurement data preprocessing. This involves examining the measured projection data to gain insight into the parameter values. In particular, stereographic analysis can be used to determine the rough location and size of the flaw. This requires at least one extra projection but the information gained is extremely valuable. The approximate location is calculated by stereographically reconstructing the approximate centroid of the flaw. With volumetric flaws, there is more susceptibility to correspondence errors, but approximate results are acceptable for use in the reconstruction algorithm. Once an approximate location is known, an approximate magnification can be computed as

$$m = \frac{D}{y_o}, \tag{3.55}$$

where D is the source-detector distance and y_o is the flaw-to-source distance. The estimated initial value for one of the principal axes lengths is thus

$$\hat{a} = \frac{t_{max} - t_{min}}{m}, \tag{3.56}$$

where t_{max} and t_{min} are the boundary coordinates of the flaw on the detector. The other principal axis length is estimated using the measured projection values. The computation of the projection values from the detector signal will be discussed in Chapter 5.

The second major problem associated with numerically estimating the parameters is the potential inconsistency between the region of support for the current parameter iteration and the measurement data. The region of support is defined as the region of the detector that the projection model exists for a given set of parameters. This becomes clear when we examine the forward projection model given by Eq. (3.30). For a fixed set of parameters, there exists a bounded region (t_{min}, t_{max}) such that $g(t,\theta)$ is real. Outside this region $g(t,\theta)$ is imaginary, but in practice it is set to zero to be consistent with the physical meaning (i.e., the projection of the ellipse along rays not intersecting the ellipse is zero). We formally define the region of support for the ith set of parameters as

$$S_i = \{t : \ t_{i\ min} \leq t \leq t_{i\ max}\}. \tag{3.57}$$

We define the measurement region as

$$S_m = \{t : \ t_{m\ min} \leq t \leq t_{m\ max}\} \tag{3.58}$$

where $t_{m\ min}$ and $t_{m\ max}$ are the maximum and minimum t values used in the measurement data. S_m is not associated with any particular parameter value because it is a fixed region defined by the measurement process.

The problem arises when $S_m \cap S_i \neq S_m$. This means that every element in S_m is not defined for every element in S_i, creating a problem in the numerical evaluation of the model at points in S_m. This inconsistency can occur at the start of the iteration process from the initial values, or it can occur during the iteration process as the parameter vector changes. The problem has been sidestepped by setting the model equal to zero at these points. Even though the model does not mathematically predict zero at these points, it works well as evidenced by the convergence in the simulation of Fig. 3.14. In the case of this simulation, the region of support for the initial parameter values is (-1.5,5) which does not contain all measurement points.

Finally, some comments should be made about the computational requirements of the reconstruction algorithm. The reconstruction software has been implemented on a Stellar GS-1025 graphics supercomputer using the C programming language. It is rated at a peak performance rate of 40 MFLOPS when the code is vectorized. When the program is run using 200 measurement points with no vectorization, each iteration takes approximately 10 seconds of CPU time. When run using optimized math functions, each iteration takes approximately 2 seconds of CPU time.

4. 3-D VOLUMETRIC FLAW RECONSTRUCTION

In the previous chapter, we considered reconstruction of a 2-D elliptical flaw model. This was done as a precursor to 3-D reconstruction to gain insight into the geometry and numerical difficulties associated with the much more complicated 3-D problem. It will also ultimately be used as a component of the 3-D reconstruction. In 3-D reconstruction, we model the volumetric flaw boundary as an ellipsoidal surface. We take basically the same approach as the 2-D reconstruction; we formulate an analytical forward projection model and attempt to invert the model from the measurement data.

The ellipsoidal prototype flaw model is given by

$$f(x,y,z) = \begin{cases} 1 & \frac{x^2}{A^2} + \frac{y^2}{B^2} + \frac{z^2}{C^2} \\ 0 & \text{elsewhere} \end{cases} , \tag{4.1}$$

where A, B, and C are the semi-principal axes lengths. The forward projection model for the ellipsoidal flaw is derived using the 3-D Radon transform. The Radon transform of the prototype ellipsoid is considerably more complicated than that of the ellipse due to the third dimension, but it is computed basically in the same way as the 2-D case.

We initially define the measurement plane in which the x-ray projections are measured as the x-z plane of a (x,y,z) right-hand Cartesian coordinate system. This

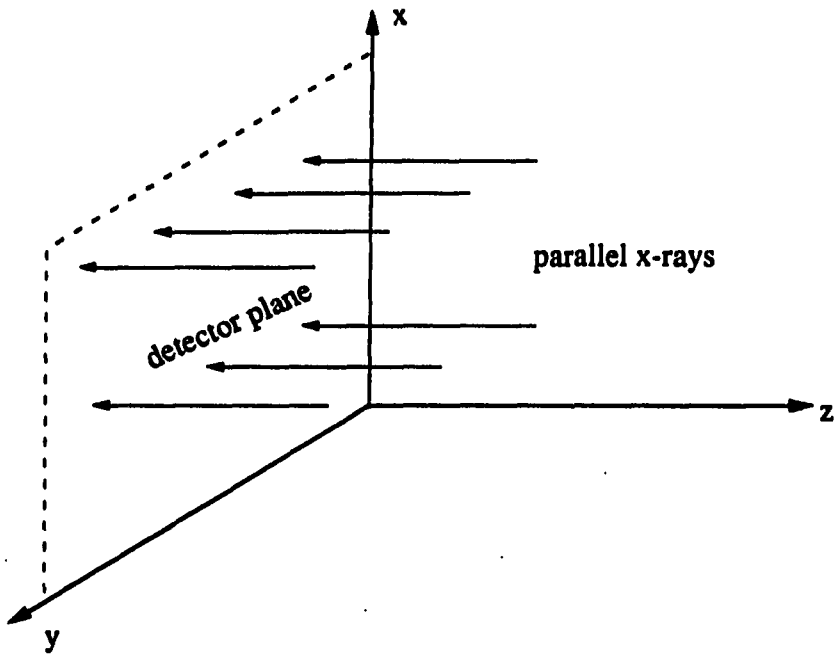

Figure 4.1: Illustration of parallel-beam measurement system

is illustrated in Fig. 4.1. We also assume parallel beam x-rays impinging normally to the detector plane. The line of the x-ray impinging on point (x_o,z_o) on the detector plane can be described by the intersection of the two planes

$$x = x_o \tag{4.2}$$

$$y = y_o. \tag{4.3}$$

We now allow the detector plane to be arbitrarily oriented by performing three rotations of the coordinate system. The first is a counterclockwise rotation, θ, about the z axis yielding the (t', s', z) axes. The second is a counterclockwise rotation, γ, about the t' axis yielding the (t', s, r') axes. The third is a counterclockwise rotation,

ψ, about the s axis yielding the (t, s, r) axes. The corresponding measurement plane in the rotated system is the t-r plane. The transformation of coordinates for each rotation can be written as follows:

$$\begin{bmatrix} t' \\ s' \\ z \end{bmatrix} = \begin{bmatrix} \cos\theta & \sin\theta & 0 \\ -\sin\theta & \cos\theta & 0 \\ 0 & 0 & 1 \end{bmatrix} \begin{bmatrix} x \\ y \\ z \end{bmatrix} \tag{4.4}$$

$$\begin{bmatrix} t' \\ s \\ r' \end{bmatrix} = \begin{bmatrix} 1 & 0 & 1 \\ 0 & \cos\gamma & \sin\gamma \\ 0 & -\sin\gamma & \cos\gamma \end{bmatrix} \begin{bmatrix} t' \\ s' \\ z \end{bmatrix} \tag{4.5}$$

$$\begin{bmatrix} t \\ s \\ r \end{bmatrix} = \begin{bmatrix} \cos\psi & 0 & \sin\psi \\ 0 & 1 & 0 \\ -\sin\psi & 0 & \cos\psi \end{bmatrix} \begin{bmatrix} t' \\ s \\ r' \end{bmatrix} \tag{4.6}$$

The composite transformation can be written as

$$\begin{bmatrix} t \\ s \\ r \end{bmatrix} = \begin{bmatrix} a_{11} & a_{12} & a_{13} \\ a_{21} & a_{22} & a_{23} \\ a_{31} & a_{32} & a_{33} \end{bmatrix} \begin{bmatrix} x \\ y \\ z \end{bmatrix}, \tag{4.7}$$

where

$$a_{11} = \cos\psi\cos\theta + \sin\psi\sin\gamma\sin\theta \tag{4.8}$$

$$a_{12} = \cos\psi\sin\theta - \sin\psi\sin\gamma\cos\theta \tag{4.9}$$

$$a_{13} = \sin\psi\cos\gamma \tag{4.10}$$

$$a_{21} = -\cos\gamma\sin\theta \tag{4.11}$$

$$a_{22} = \cos\gamma\cos\theta \tag{4.12}$$

$$a_{23} = \sin\gamma \tag{4.13}$$

$$a_{31} = -\sin\psi\cos\theta + \cos\psi\sin\gamma\sin\theta \tag{4.14}$$

$$a_{32} = -\sin\psi\sin\theta - \cos\psi\sin\gamma\cos\theta \tag{4.15}$$

$$a_{33} = \cos\psi\cos\gamma \tag{4.16}$$

Figure 4.2 illustrates the re-oriented detector plane absent the ψ rotation for simplicity. An arbitrarily oriented plane can actually be uniquely described by the first two orientation angles, as the ψ rotation is simply a rotation of the measurement plane about its normal. This third angle has been introduced, however, to assist in the derivation of the rotation and translation properties of the 3-D Radon transform in the next section.

We describe an x-ray line impinging normal to the re-oriented detector plane at point (t_o,r_o) by the intersection of the two planes

$$r = r_o \tag{4.17}$$

$$t = t_o. \tag{4.18}$$

These are written in terms of the original coordinates (x,y,z) by applying the composite transformation of Eq. (4.7).

$$r_o = a_{11}x + a_{12}y + a_{13}z \tag{4.19}$$

$$t_o = a_{31}x + a_{32}y + a_{33}z. \tag{4.20}$$

The projection of the prototype ellipsoidal model onto the t-r detector plane is computed by solving for the intersection of the x-ray line with the prototypical ellipsoidal surface equation given by

$$\frac{x^2}{A^2} + \frac{y^2}{B^2} + \frac{z^2}{C^2} = 1. \tag{4.21}$$

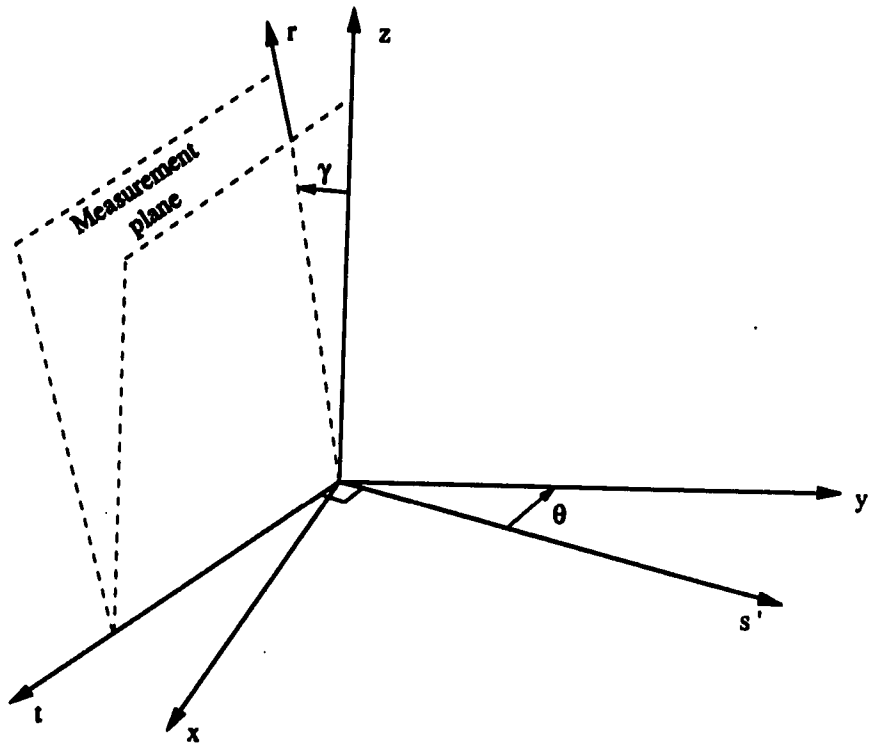

Figure 4.2: Orientation of the detector plane

The intersection points are computed by solving Eqs. (4.19), (4.20) and (4.21) simultaneously for x, y, and z. We may not require the solution of all three coordinates because the distance between intersection points can be computed from any one of the coordinates as it is the projection of the length onto the coordinate axis. The solution in terms of x yields the following quadratic equation:

$$x^2\left(\frac{1}{A^2}+\frac{T^2P^2}{B^2}+\frac{R^2}{C^2}\right)+x\left(\frac{2P^2ST}{B^2}-\frac{2QR}{C^2}\right)+\left(\frac{P^2S^2}{B^2}+\frac{Q^2}{C^2}-1\right)=0 \quad (4.22)$$

where

$$P = \left(\frac{a_{13}}{a_{13}a_{32}-a_{33}a_{12}}\right) \quad (4.23)$$

$$S = \left(r_o-\frac{a_{33}t_o}{a_{13}}\right) \quad (4.24)$$

$$T = \left(\frac{a_{33}a_{11}}{a_{13}}-a_{31}\right) \quad (4.25)$$

$$Q = \frac{1}{a_{13}}\left\{t_o-\left(\frac{a_{12}a_{13}}{a_{13}a_{32}-a_{33}a_{12}}\right)\left(r_o-\frac{a_{33}t_o}{a_{13}}\right)\right\} \quad (4.26)$$

$$R = \frac{1}{a_{13}}\left\{\left(\frac{a_{12}a_{13}}{a_{13}a_{32}-a_{33}a_{12}}\right)\left(\frac{a_{33}a_{11}}{a_{13}}-a_{31}\right)+a_{11}\right\} \quad (4.27)$$

The projection of the x-ray length onto the x-axis is

$$d_x = x_2 - x_1$$

$$= \frac{\sqrt{\left(\frac{2P^2ST}{B^2} - \frac{2QR}{C^2}\right)^2 - 4\left(\frac{1}{A^2} + \frac{T^2P^2}{B^2} + \frac{R^2}{C^2}\right)\left(\frac{P^2S^2}{B^2} + \frac{Q^2}{C^2} - 1\right)}}{\left(\frac{1}{A^2} + \frac{T^2P^2}{B^2} + \frac{R^2}{C^2}\right)}, \tag{4.28}$$

where x_1 and x_2 are the two real solutions of Eq. (4.22). The length of the x-ray within the prototype ellipsoid, yielding the forward prototype projection model (Radon transform) for parallel beam geometry is thus,

$$p(t_o, r_o; A, B, C, \theta, \gamma, \psi) = \begin{cases} \frac{d_x}{\cos\gamma \sin\theta} & , \sqrt{\cdot} \text{ real} \\ 0 & , \sqrt{\cdot} \text{ imaginary} \end{cases} . \tag{4.29}$$

Under certain detector plane orientations, the quantity $x_2 - x_1$ may be very small. Under these circumstances, the projection model can be derived in terms of $y_2 - y_1$ or $z_2 - z_1$. The derivation is very similar to above and yields equations of the same form.

4.1 Translational Property of the 3-D Radon Transform

In order to allow the arbitrary location of the ellipsoidal flaw model, the translation property of the 3-D Radon transform must be derived. We begin by writing the general 3-D Radon transform of an object, $f(x, y, z)$, as

$$P_{\theta,\gamma,\psi}(t, r) = \int_{-\infty}^{\infty}\int_{-\infty}^{\infty}\int_{-\infty}^{\infty} f(x, y, z)\delta(\aleph_1 - \aleph_2)dxdydz, \tag{4.30}$$

where $(\aleph_1 - \aleph_2) = 0$ defines the path of the x-ray line. From before, the x-ray path is described by the intersection of the two planes

$$t_o - (a_{11}x + a_{12}y + a_{13}z) = 0 \tag{4.31}$$

$$r_o - (a_{31}x + a_{32}y + a_{33}z) = 0. \tag{4.32}$$

Let

$$\aleph_1 = t_o - (a_{11}x + a_{12}y + a_{13}z) \tag{4.33}$$

and

$$\aleph_2 = r_o - (a_{31}x + a_{32}y + a_{33}z). \tag{4.34}$$

Then

$$\begin{aligned} P_{\theta,\gamma,\psi}(t,r) &= \int_{-\infty}^{\infty}\int_{-\infty}^{\infty}\int_{-\infty}^{\infty} f(x,y,z)\cdot \\ &\quad \delta(t - a_{11}x - a_{12}y - a_{13}z - r + a_{31}x + a_{32}y + a_{33}z)dxdydz. \end{aligned} \tag{4.35}$$

We now shift the object function by (x_o,y_o,z_o) resulting in

$$\begin{aligned} P^s_{\theta,\gamma,\psi}(t,r) &= \int_{-\infty}^{\infty}\int_{-\infty}^{\infty}\int_{-\infty}^{\infty} f(x - x_o, y - y_o, z - z_o)\cdot \\ &\quad \delta(t - a_{11}x - a_{12}y - a_{13}z - r + a_{31}x + a_{32}y + a_{33}z)dxdydz. \end{aligned} \tag{4.36}$$

Letting $u = x - x_o$, $v = y - y_o$ and $w = z - z_o$, (4.36) becomes

$$\begin{aligned} P^s_{\theta,\gamma,\psi}(t,r) &= \int_{-\infty}^{\infty}\int_{-\infty}^{\infty}\int_{-\infty}^{\infty} f(u,v,w)\cdot \\ &\quad \delta(t - a_{11}(u + x_o) - a_{12}(v + y_o) - a_{13}(w + z_o) - \\ &\quad r + a_{31}(u + x_o) + a_{32}(v + y_o) + a_{33}(w + z_o))dudvdw. \end{aligned} \tag{4.37}$$

Comparing $P^s_{\theta,\gamma,\psi}(t,r)$ with $P_{\theta,\gamma,\psi}(t,r)$, we arrive at the translation property of the 3-D Radon transform:

Translation Property:

Let P be the Radon transform of an object function, $f(x,y,z)$. Then the Radon transform, P^s of a shifted object function, $f(x - x_o, y - y_o, z - z_o)$, is

$$P^s(t,r) = P(t - a_{11}x_o - a_{12}y_o - a_{13}z_o\ ,\ r + a_{31}x_o + a_{32}y_o + a_{33}z_o)$$

where (t,r) are the detector coordinates and a_{ij} are defined by Eqs. (4.8)-(4.16).

4.2 Rotational Property of the 3-D Radon Transform

The rotational property of the 3-D Radon transform is derived to allow for the arbitrary orientation of an object function. We define the orientation angles of the object function, θ_o, γ_o, and ψ_o exactly as the orientation angles of the detector plane. The rotation property is derived in a manner similar to the 2-D case by writing the unrotated transform in polar coordinates. The rotation of the object can then be applied in the transform followed by the substitution of variables, $\phi = \theta - \theta_o$, $\xi = \gamma - \gamma_o$ and $\eta = \psi - \psi_o$. This yields the rotation property for the 3-D Radon transform.

Rotation Property:

Let $P(t,r)$ be the 3-D Radon transform of an object function, $f(x,y,z)$. The Radon transform, $P^r(t,r)$ of a rotated object function, $f^r(x,y,z)$ is

$$P^r(t,r) = P(t,r)\Big|_{\theta=\theta-\theta_o,\gamma=\gamma-\gamma_o,\psi=\psi-\psi_o}.$$

At this point notice that the angle ψ was required for the detector orientation in order to accommodate the ψ_o rotation of the object function. It was also implicitly required in the translation property. It is interesting to point out that a rotation of the object is equivalent to an opposite rotation of the detector plane by the same amount.

It is important to consider the order of application of the translation and rotation properties as it was in the 2-D case. In most instances we wish to apply the rotation property first because the rotation defined is about the coordinate origin. The trans-

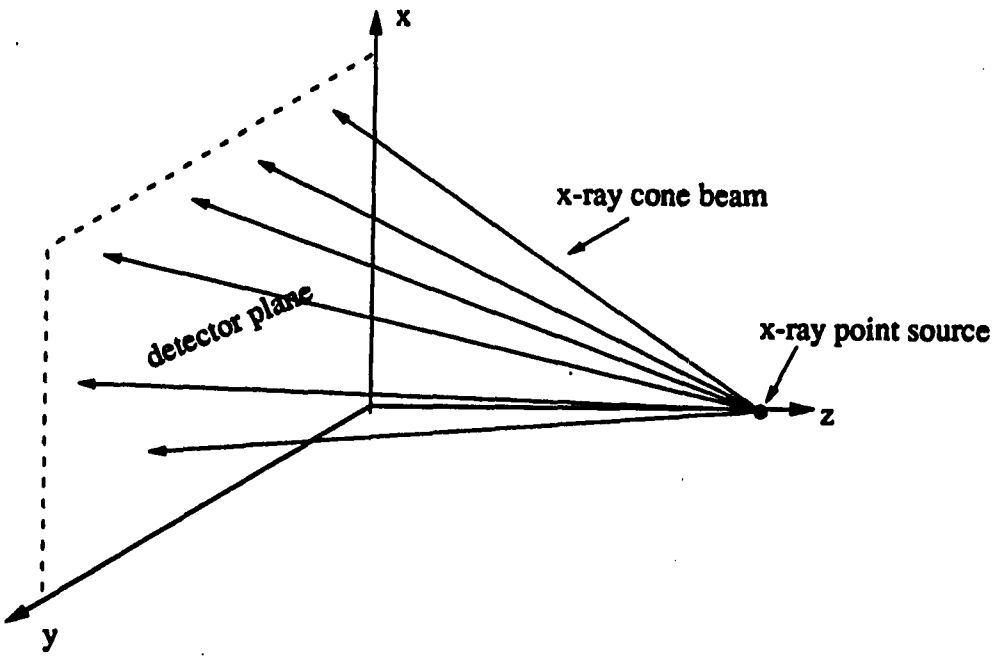

Figure 4.3: Cone-beam x-ray source geometry

lation property can then be used to translate the re-oriented object to the desired location. The translation and rotation properties are applied to the forward prototype projection model by replacing t, r, θ, γ and ψ in Eq. (4.29) by the quantities defined in the above properties.

4.3 Cone-Beam Conversion

The derivation of the forward projection model so far has assumed a parallel beam x-ray source geometry. In this section, we derive the transformation to convert this geometry to the cone-beam geometry of a microfocus x-ray source. In a cone-beam geometry, all x-rays emanate as straight lines from a point as shown in Fig. 4.3.

We define a single x-ray line out of a cone-beam source as a cone-ray. For each cone-ray, an alternative detector orientation is computed such that the cone-ray is normal to the detector. The parallel-beam Radon transform is used with this alternative detector orientation to compute the forward projection generated with that cone-ray. Consider the cone-ray shown in Fig. 4.4. The reorientation of the (t,r) detector plane to the (t',r') plane causes the cone-ray to be normal to it at point (t'_o, r'_o). The coordinates (t'_o, r'_o) are related to the reorientation angles, α and ζ, which in turn are related to the original detector coordinates, (t_o,r_o), and the source-detector distance. The detector reorientation angles are given by

$$\alpha = \tan^{-1}\left(\frac{t_o}{D}\right) \tag{4.38}$$

$$\zeta = \tan^{-1}\left(\frac{r_o}{\sqrt{t_o^2 + D^2}}\right). \tag{4.39}$$

where D is the perpendicular source-detector distance and (t_o,r_o) are the coordinates of the original detector position of the cone-ray of interest. We thus have the new detector orientation angles for use in the Radon transform.

$$\theta_{new} = \theta_{old} + \alpha \tag{4.40}$$

$$\gamma_{new} = \gamma_{old} + \zeta. \tag{4.41}$$

The new detector coordinates are given by

$$t'_o = t_o \cos\zeta \tag{4.42}$$

$$r'_o = \frac{r_o t'_o}{\tan\zeta\sqrt{t_o^2 + d^2}}. \tag{4.43}$$

Note that each cone-ray has its own alternative detector orientation and location for use in the parallel-beam Radon transform.

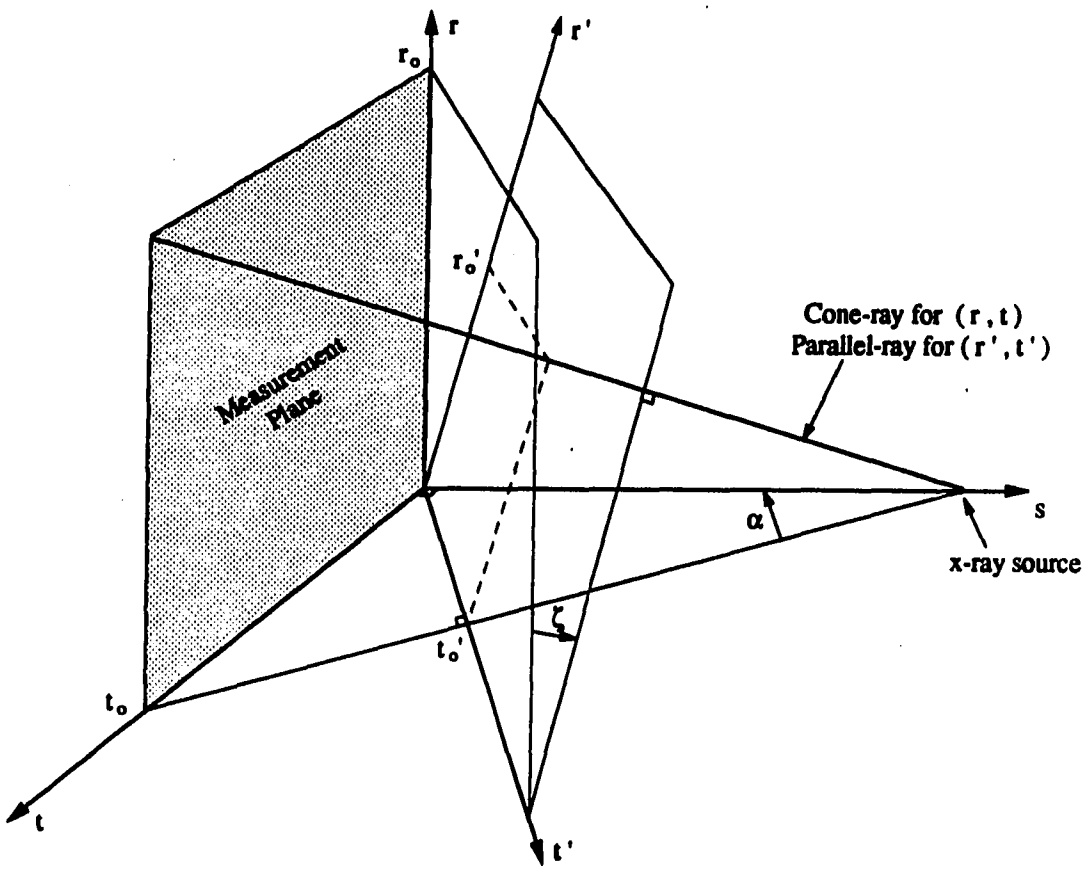

Figure 4.4: Illustration of the conversion to cone-beam geometry

Some example projections produced by the model are shown in Fig. 4.5. Each projection was generated by an ellipsoid having the parameters (A=4.00, B=2.00, C=2.00, θ=1.57, γ=0.00, ψ=0.00). The first projection was with the ellipsoid centered at x_O=10.0, y_O=10.0, z_O=60.0. The other projections were generated by shifting the ellipsoid to x_O=10.0, y_O=20.0 and x_O=20.0, y_O=20.0. The projection values have been scaled linearly to the range 0-255 so that they can be displayed as a gray-scale image. Notice the effects of magnification as the ellipsoidal flaw is shifted away from the source.

4.4 3-D Inversion Problem

The forward projection model for a three-axes ellipsoid with arbitrary location and orientation for a cone-beam x-ray source has been derived by applying the 3-D rotation and translation properties as well as the cone-beam transformation to the forward projection model for the prototype ellipsoid. The goal of 3-D reconstruction is to use the projection model along with x-ray measurement data to estimate the ellipsoidal model parameters. Originally, it was intended to use the same estimation approach taken in the 2-D reconstruction of Chapter 3. This would have involved using a nonlinear optimization routine to minimize the squared error between the measurements and the projections of some best fit ellipsoidal model. In the 2-D case, this was a problem in 5 dimensions which was demonstrated to be solvable when enough prior information is known about the flaw. For the 3-D case, the problem has 9 dimensions and is considerably more complicated geometrically. From a numerical standpoint, the linearization associated with nonlinear optimization methods is complicated by the large number of partial derivatives and implicit functions. In

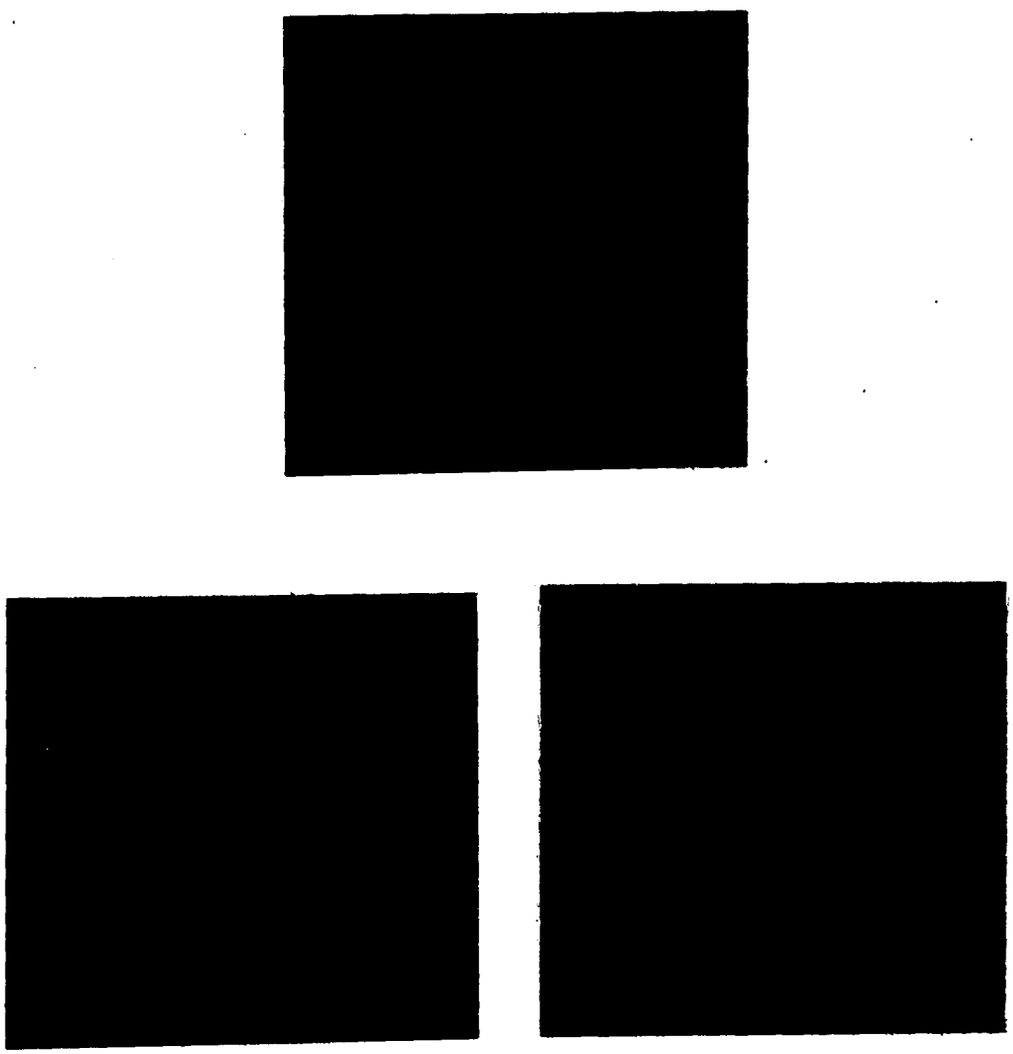

Figure 4.5: Example projections produced by the 3-D ellipsoidal model

addition, the amount of measurement data required is very large because the measurement space is two dimensional. For a typical flaw, there may be as many as 10,000 measurement points to cover a flaw area of 100 x 100 pixels. Considering the CPU time requirement for each iteration and the number of iterations required for the 2-D case, it appeared that the reconstruction time for an iterative solution in the 3-D case would be unreasonable for practical application. In addition, the task of minimizing a function in a nine dimensional space is formidable at best. For these reasons it was decided that the 3-D reconstruction would be broken into several simpler 2-D problems. The 3-D forward projection model is still useful in generating the test data for simulations, however, it isn't used in the inverse reconstruction method.

The idea of performing 3-D reconstruction of an ellipsoid by breaking the problem into smaller 2-D reconstructions centers around the fact that any slice through an ellipsoid forms an ellipse (Gellert et al. 1975). This fact means that the projections along any line in the detector plane can be used with the 2-D forward elliptical projection model of Chapter 3 to reconstruct a cross section of an ellipsoid. The flaw is thus modeled as a series of elliptical slices rather than an entire ellipse. This type of reconstruction is potentially more accurate than ellipsoidal reconstructions because a nonellipsoidal flaw might be better modeled by a series of elliptical slices. The procedure for reconstructing the elliptical slices is as follows:

1. Obtain at least two stereographic projections.
2. Estimate initial values for elliptical parameters in region of slice.
3. Select slice in the detector plane for reconstruction.
4. Reconstruct elliptical slice in local coordinate system.

5. Convert ellipse locus to global coordinate system.

6. Display result.

7. Repeat process for more elliptical slices.

The slice in the image plane is defined by its intercept with the t axis (x axis if $\theta = \psi = 0$) and its angle with respect to the perpendicular to t. The plane containing the slice line and the x-ray source is called the *fan-plane*. The local coordinate system for the fan-plane is defined by the slice line and the line containing the t axis intercept that is perpendicular to the slice line. The ellipse is reconstructed by first converting the measurement data ordinates to the local coordinate system and then performing the 2-D reconstruction as outlined in Chapter 3. Figure 4.6 illustrates a slice in the detector plane with its associated fan-plane and local coordinate system (l,m). The locus of points on the ellipse in the local coordinate system are converted to the global (t,r,s) coordinate system through two rotational transformations and one translational transformation.

First, the m axis is rotated by β about the l axis where β is defined by

$$\beta = \tan^{-1}\left(\frac{D}{t_i}\right). \tag{4.44}$$

Next, the l axis is rotated by η about the m axis. These two rotations align the (l,m) plane with the (r,s) plane. The (l,m) coordinate system is then translated by $-t_i$ to complete the transformation. The composite rotation transformation is

$$\begin{bmatrix} s \\ r \\ t' \end{bmatrix} = \begin{bmatrix} \cos\beta & 0 & \sin\beta \\ -\sin\beta\sin\eta & \cos\eta & \cos\beta\sin\eta \\ -\sin\beta\cos\eta & -\sin\eta & \cos\beta\cos\eta \end{bmatrix} \begin{bmatrix} m \\ l \\ 0 \end{bmatrix}. \tag{4.45}$$

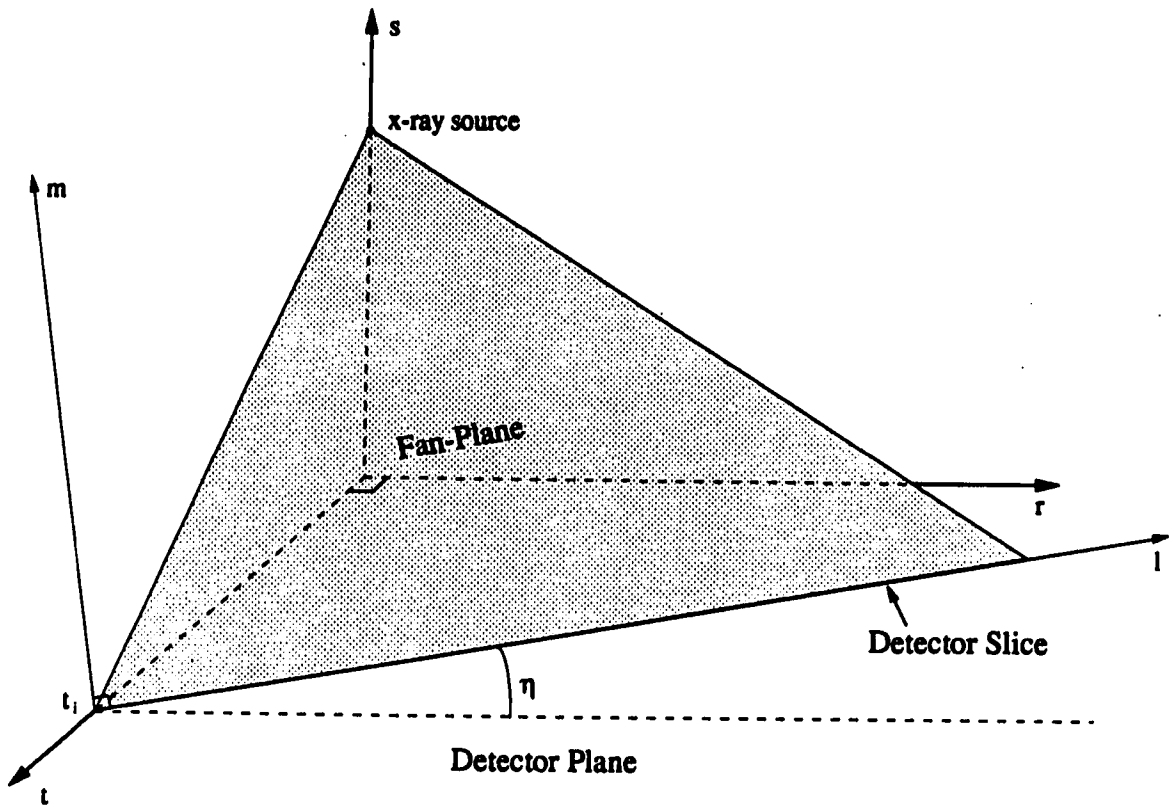

Figure 4.6: Illustration of fan-beam slice and local coordinate system

Finally, the t_l coordinate must be translated:

$$t = t' - t_i. \tag{4.46}$$

This reconstruction technique has been implemented and applied to simulated projection data of an ellipsoid. The set of simulated data was generated using the 3-D forward projection model defined earlier. A cone-beam projection of an ellipsoid having parameters (A = 6.0, B = 12.0, C = 6.0, θ_o = 0.0, γ_o = 0.0, ψ_o = 0.0, x_o = 32.0, y_o = 32.0, z_o = 32.0) is shown in Fig. 4.7. The source-detector distance is 64.0. Slices in the detector plane were taken along lines having the form

$$(\frac{x_i}{L} + \frac{y_i}{M}) = 1 \tag{4.47}$$

with L and M taking on the values (100,100), (120,120), (140,140), (160,160). The locus of ellipses reconstructed from the four slices after conversion to the global coordinate system are shown in Fig. 4.8. They correspond almost exactly to planar cuts through the ellipsoidal model used to generate the simulation. In this simulation, no noise was added to the measurement data and therefore, no confidence intervals were computed. The technique was implemented on noisy data obtained through radiography of fabricated test samples in the following chapter.

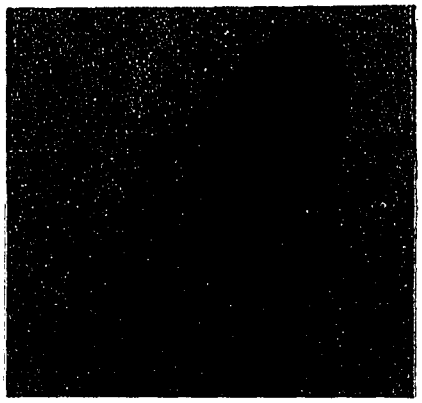

Figure 4.7: Projection of simulated ellipsoid used in the reconstruction

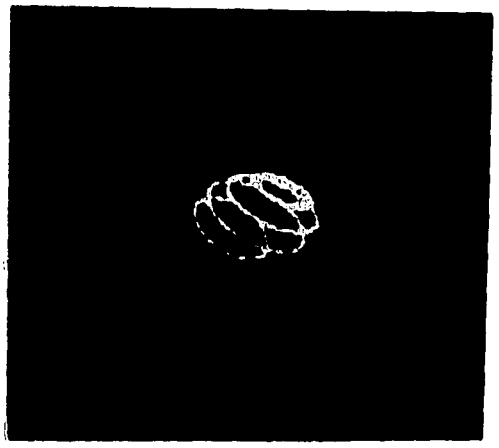

Figure 4.8: Display of reconstructed slices

5. PRACTICAL ISSUES AND EXPERIMENTAL RESULTS

5.1 Background

In this chapter, we discuss some of the practical issues of reconstructing the flaw model along with experimental results using fabricated samples. Of primary concern to obtaining good experimental results are the detector model and practical limitations.

5.2 Detector Model and the Projection Values

Thus far, we have assumed that projection values were always available for measurement in performing the reconstruction. The projection model used in this dissertation assumes a homogeneous flaw and produces values that are directly proportional to the distance the x-ray has traveled through the flaw. We can never directly measure this quantity as the detector attempts to measure a quantity related to the incoming x-ray intensity. The incoming x-ray intensity is very closely related to the projection value or ray-sum. For a homogeneous object, the number of photons arriving at the detector is (Kak and Slaney, 1988)

$$N = N_o e^{-\mu x}, \tag{5.1}$$

where μ is the material absorption coefficient, x is the length of the x-ray path, and N_O is the number of incident photons. Thus, the projection quantity used in the model, x, is given by

$$x = \frac{1}{\mu} \ln\left(\frac{N_O}{N}\right). \tag{5.2}$$

For the general case of an arbitrary object having a spatial dependent attenuation coefficient, $\mu(x,y)$, the relationship between incident and detected photons is

$$N = N_O \exp\left[-\int_{x-ray} \mu(x,y)ds\right]. \tag{5.3}$$

Thus, the ray-sum or Radon transform is

$$\int_{x-ray} \mu(x,y)ds = \ln\left(\frac{N_O}{N}\right). \tag{5.4}$$

In practice, what we are really measuring is a homogeneous flaw inside a homogeneous material. Thus, the ray-sum will have a contribution due to the flaw as well as the matrix material. Presumably we know beforehand the shape and absorption characteristics of the matrix material. If we also know the absorption characteristics of the flaw, then the projection due to the flaw alone can be computed. Consider the rectangular inclusion within a slab of material shown in Fig. 5.1. The number of photons at the detector is given by

$$N_d = N_O \exp - [(x_1 - x_2)\mu_O + x_2\mu_1]. \tag{5.5}$$

where μ_O is the matrix material absorption coefficient, μ_1 is the inclusion absorption coefficient, x_1 is the distance through the material, and x_2 is the distance through the inclusion.

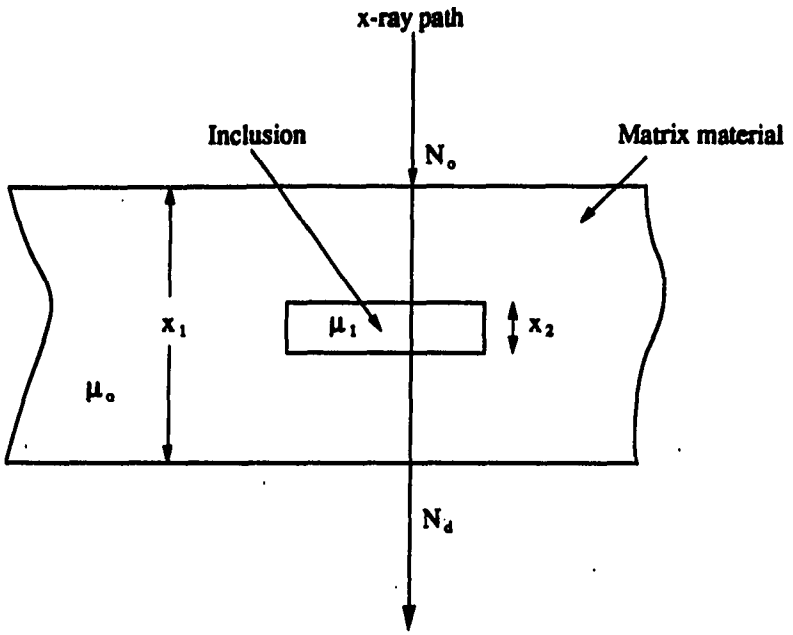

Figure 5.1: Rectangular inclusion within a slab of material

The distance through the inclusion is thus,

$$x_2 = \frac{\ln \frac{N_o}{N_d} - x_1 \mu_o}{\mu_1 - \mu_o}. \tag{5.6}$$

Typically, the number of photons is counted with a scintillation detector that is held fixed while the object under test is scanned through the x-ray beam. The detector collimates the x-ray beam and thus counts the incoming photons over a very small area. By scanning the object through the beam and recording the counts at each scan position, an image is built up that effectively yields the x-ray photon intensity versus position. The measured photon counts are corrected using an efficiency factor of the scintillation detector. The problem with this type of measurement is that it is very time consuming because the step size of the object scan must be small to obtain adequate spatial resolution. In addition, the counting time at each scan position

must be long enough to obtain good counting statistics.

A faster method for calculating the distance traveled within the flaw uses a real-time image intensifying detector with a calibration curve. With this method, a calibration is performed using a test sample whose distance profile is known a priori. The test sample is radiographed with the intensifying detector to create a calibration curve for ray-sum distance versus detector output signal. The calibration is only valid, however, for future radiographs of the same material with the same x-ray voltage and current settings. Measurements made from an unknown part composed of the same material can then be made in terms of equivalent distances through the material. This technique has the advantage of being extremely fast and convenient to implement. A full 2-D radiograph is obtained in near real-time and is easily transferred directly to a computer for calibration, processing or reconstruction.

This method was implemented with an aluminum calibration wedge for use in the model reconstruction of fabricated aluminum flaw samples. A radiograph of the wedge was made by afixing it to the face of the image intensifier and performing 128 frame averages with an x-ray voltage setting of 58.6 keV. A photograph of the radiograph, taken from the screen of a Stellar computer display is shown in Fig. 5.2. The wedge thickness varies linearly from 0.25 $\pm$ 0.005 inches at the top of the image to 0.14 $\pm$ 0.005 inches at the point where the horizontal marker protrudes from the wedge. Figure 5.3 shows the profile of the wedge between the thickness extremes. The vertical axis is the detector output, which is constrained between 0 and 255. The detector signal is the digitized output of a television camera that is focused on the phosphor plate inside the image intensifier. The television signal is digitized to 8 bits with a frame grabber video digitizing board inside a PC. The horizontal axis is

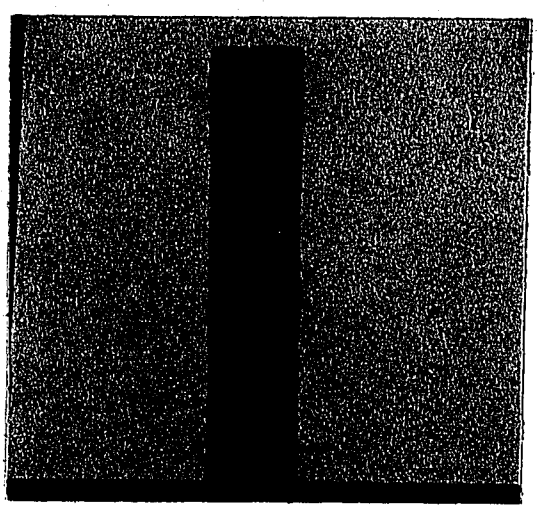

Figure 5.2: Real-time radiograph of an aluminum calibration wedge

the aluminum thickness, obtained by interpolating linearly between the two thickness extremes.

In order to obtain quantitative distance measurement from an unknown aluminum sample, a calibration curve must be generated from the profile data of Fig. 5.3. One such curve was generated by fitting a quadratic function to the data using ordinary least-squares. Figure 5.4 shows a plot of the profile data along with the fitted quadratic function. The function is

$$I = 100.8 + 1254.9x - 5865.2x^2, \tag{5.7}$$

where I is the intensifier grey scale output and x is the material thickness in inches. The correlation coefficient for the fit is 0.99. The quadratic formula can be used to compute equivalent distance values from measured intensifier data using aluminum

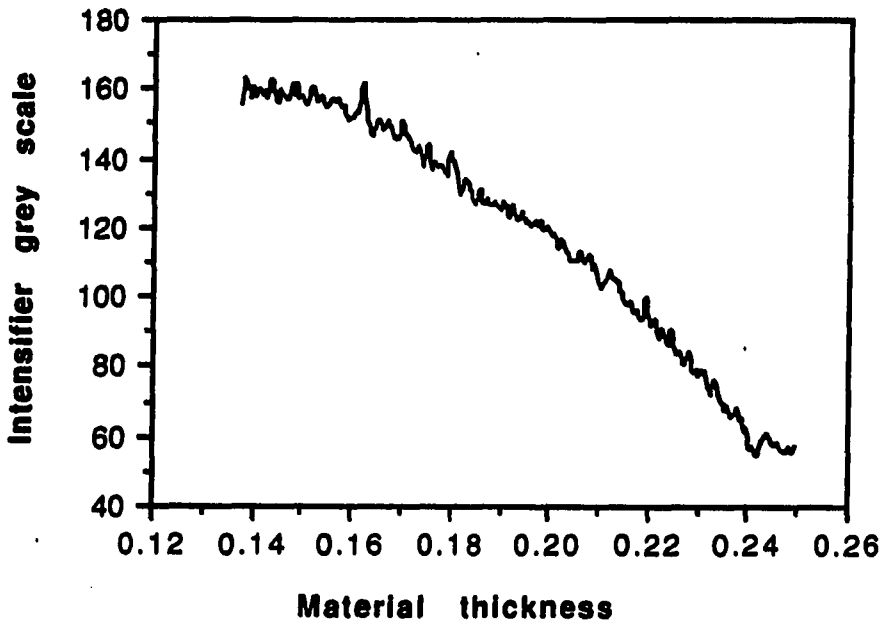

Figure 5.3: Profile across radiograph of aluminum wedge

materials and the same x-ray voltage and current settings.

An exponential fit was not used for several reasons. First, the detector output is not proportional to x-ray intensity. Second, there are nonlinearities in the intensity response near the upper and lower limits of the dynamic range. In addition, the profile shown in Fig. 5.3 has flattened tails near the edges.

An alternative calibration curve is a linear fit. The best fit line for the profile across the wedge using ordinary least squares is

$$I = 315.1 - 1019.1x. \tag{5.8}$$

A plot of the fitted line with the measured profile is shown in Fig. 5.5. The correlation coefficient in this case is 0.97. This fitted line follows the data well near the middle of the profile but tends to deviate more near the edges.

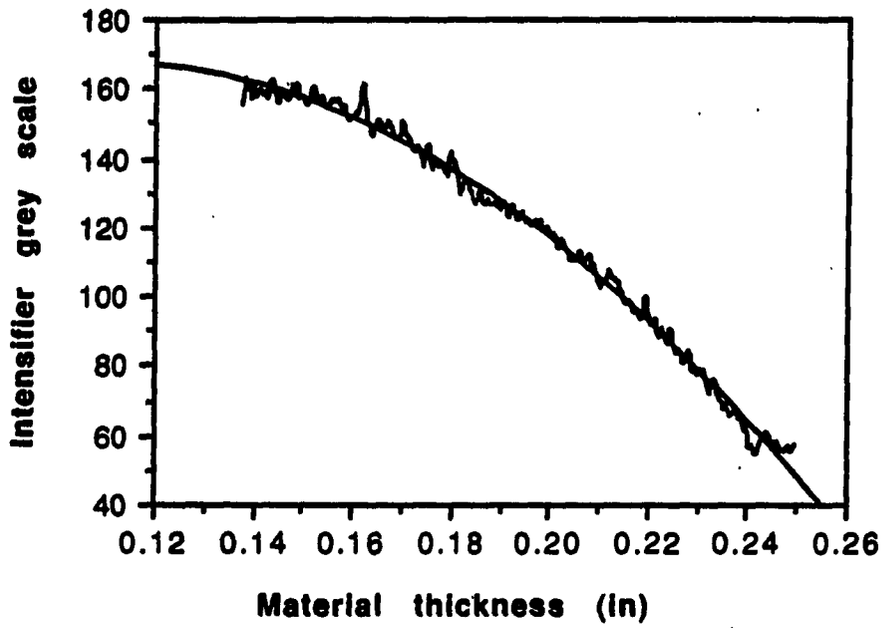

Figure 5.4: Profile of aluminum wedge with best fit quadratic function

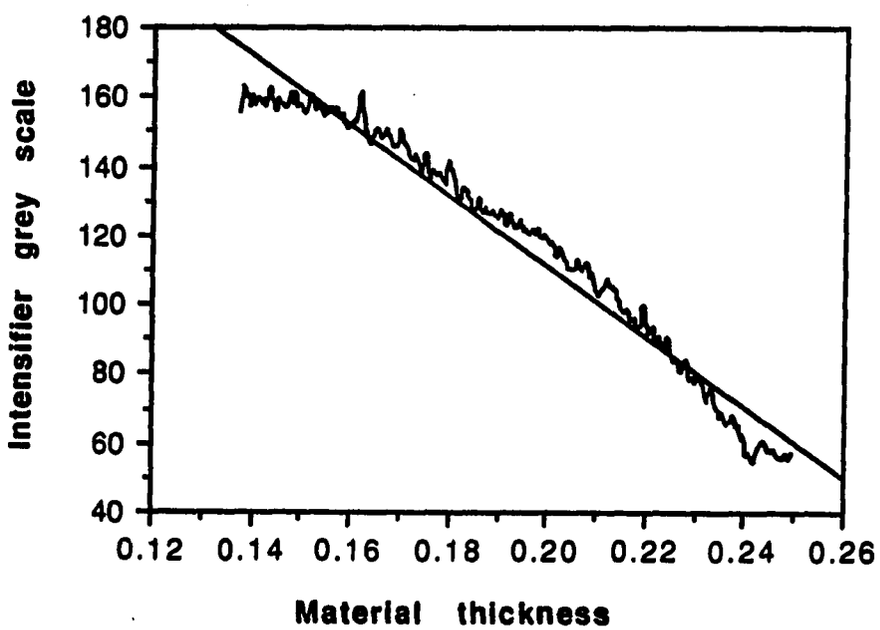

Figure 5.5: Profile of aluminum slice with best fit linear function

It is known that the output response of the detector as a function of position is not constant. Hence, the apparent nonlinearities at the edges could be explained in terms of the spatial response of the detector as well as nonlinearities in the intensity response. In any case, the modeling of the detector response for an image intensifier is a complete project in itself and we will use the simple calibration method described here without further analysis. For this work, it was decided to use the linear fit calibration in converting the measured intensities from the image intensifier to ray-sum distances because the resultant distance profiles tended to follow the actual profile of the sample better. When the quadratic calibration function was used, the profile tended to square off at the edges, while the linear calibration curve produced profiles which resembled the original slice shape better. In addition, the sample was located near the center of the detector where the spatial nonlinearities of the detector response are small. A plot of a slice through a real-time radiograph of an ellipsoid shaped sample is shown in Fig. 5.6. The horizontal axis is the detector position and the vertical axis is the detector output signal.

Plots of the data after being calibrated through Eqs. (5.7) and (5.8) are shown in Figs. 5.7 and 5.8, respectively. In these plots, the vertical axis is now the distance in inches projected through the aluminum sample. Notice that the linear calibration follows the shape of the original slice profile slightly better than the quadratic calibration. One might argue that the true profile of the sample *is* squared off at the edges, but in this case it is not as the sample is known to be an ellipsoid.

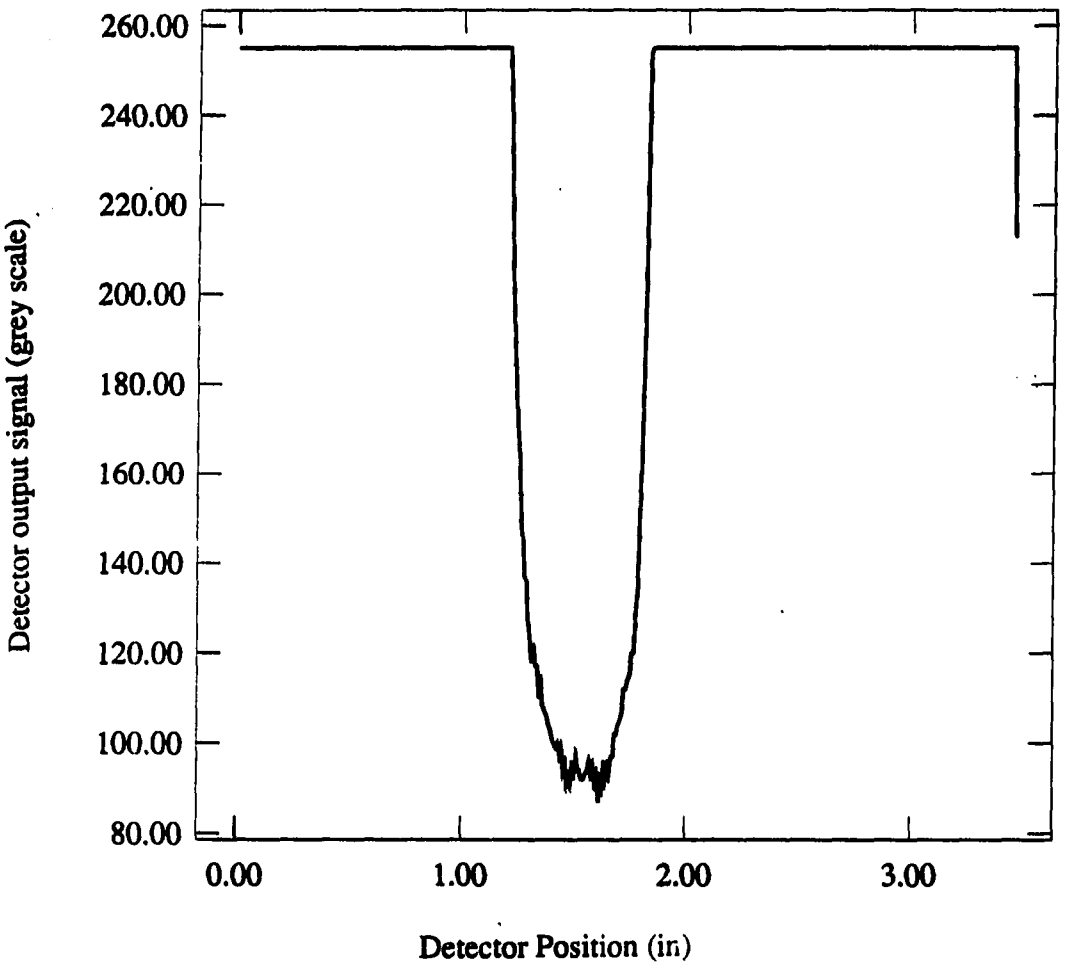

Figure 5.6: Slice of real-time radiograph of an aluminum sphere

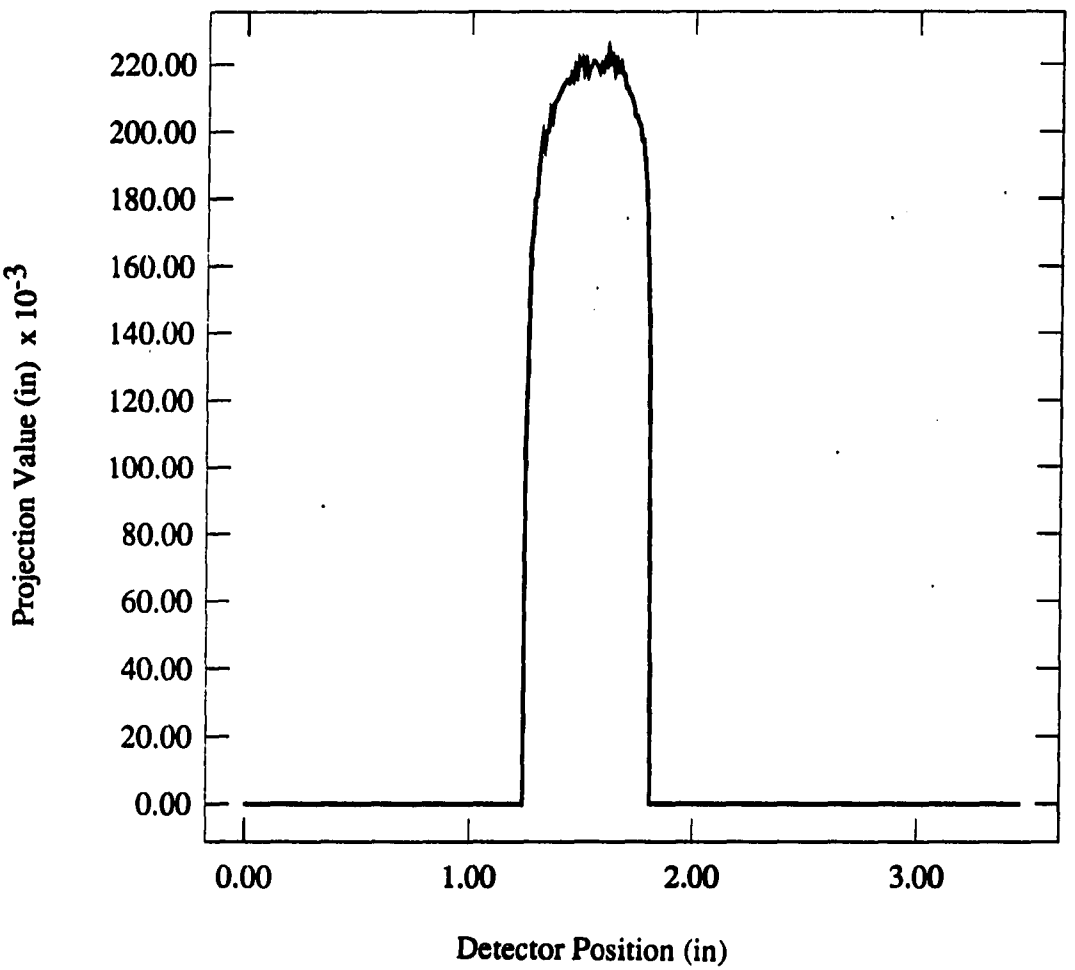

Figure 5.7: Calibrated slice through aluminum sphere (quadratic function)

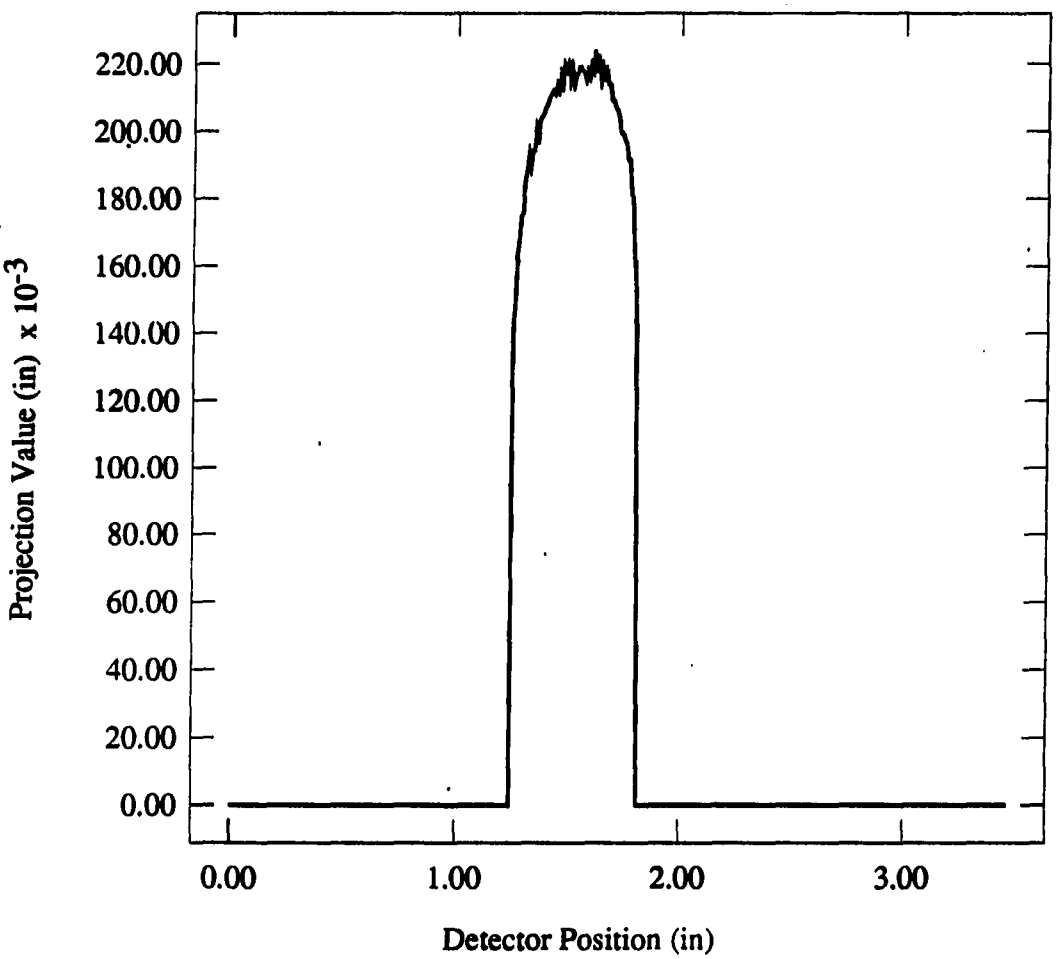

Figure 5.8: Calibrated slice through aluminum sphere (linear function)

5.3 Experimental Results - Fabricated Samples

In this section, results of the application of the methods of Chapters 3 and 4 to several fabricated aluminum test samples are presented. The test samples include two roughly ellipsoidal samples, a cylindrical sample, and a spherical sample. A photograph of the collection of samples is shown in Fig. 5.9. One of the ellipsoidal samples is closer to a capsule shape while the other is closer to a barrel shape. This collection is a fairly wide representation of some of the possible shapes of void-like flaws. The radiography of these samples was performed by placing them in free space, allowing for the easier computation of the projection distances. Although this situation is unrealistic in a true inspection setting, it is useful for validation of the modeling method. In addition to the model parameter estimation, stereology concepts are employed to estimate the sample volumes.

5.3.1 Aluminum Ellipsoids

The three ellipsoidal aluminum samples used here include two ellipsoids of revolution and one spheroid. The ellipsoids of revolution have approximate semi-principal axes lengths, A=0.25 $\pm$ 0.005 inches and B=C=0.13 $\pm$ 0.005 inches. The spheroid has a diameter of 0.25 $\pm$ 0.005 inches. These values were obtained through caliper measurements of the samples. The the two ellipsoids of revolution were fabricated by machining the ends of a cylindrical aluminum rod on a lathe until they were approximately ellipsoidal. One of the samples is shaped much like a medicine capsule and the other is shaped like a barrel with rounded ends. Thus, the machined samples do not represent true ellipsoids and the measured principal axis lengths are simply the measured length and width of the samples.

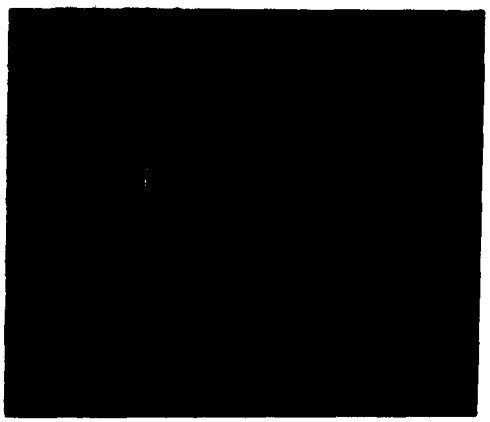

Figure 5.9: Photograph of aluminum test samples

Three radiographs of each sample were produced using the Ridge microfocus x-ray machine and the real-time image intensifier. The radiographs of each sample were made at one reference position and at two translated positions (horizontally 1.0 inches and 1.5 inches). The translation was performed by placing the samples atop a loop of cellophane tape on an automatic x-y-z positioner. A schematic diagram of the experimental setup os shown in Fig. 5.10. Photographs of real-time radiographs of each sample at the 1.0 inch translation are shown in Figs. 5.11-5.13. The background of each radiograph is saturated since the samples were not surrounded by any attenuating material.

The various parameters used in the radiography were

$$x-\text{ray voltage} = 58.6 \text{ keV}$$

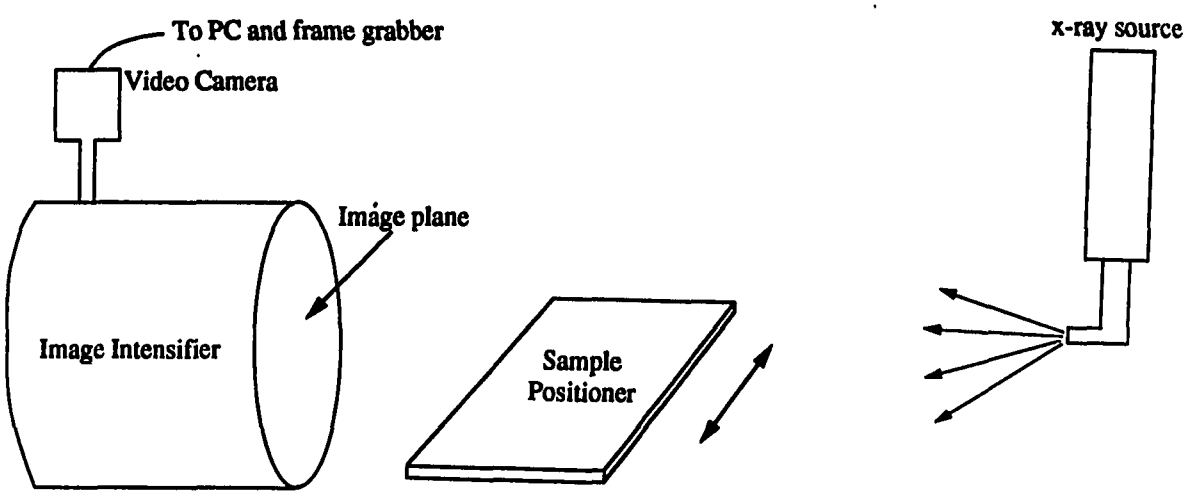

Figure 5.10: Schematic diagram of experimental setup

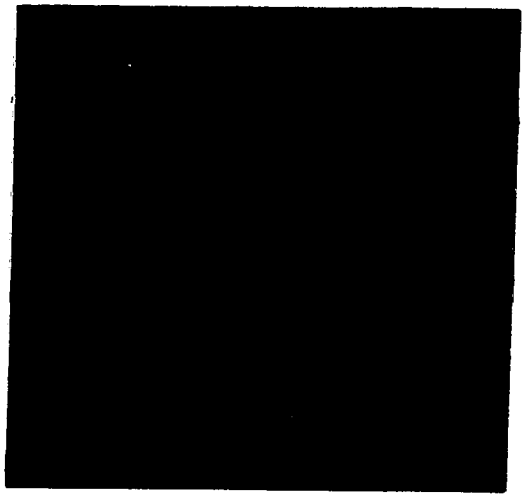

Figure 5.11: Real-time radiograph of ellipsoid 1 (capsule)

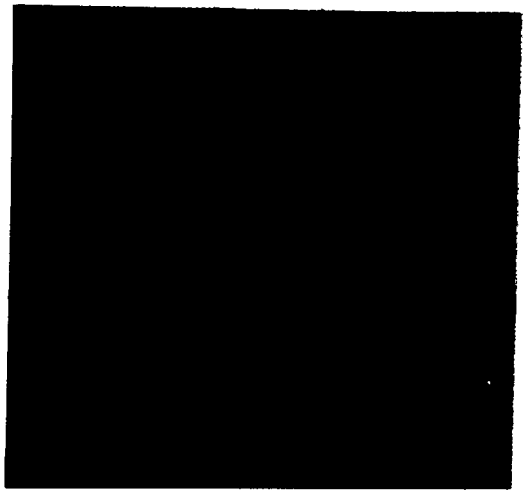

Figure 5.12: Real-time radiograph of ellipsoid 2 (barrel)

Figure 5.13: Real-time radiograph of spheroid

source to detector distance = 54.0 in $\pm$ 0.2

sample to detector distance = 15.5 in $\pm$ 0.2

coordinate origin on radiograph : x = 92 pixels; y = 187 pixels

The x direction is horizontal and the y direction is vertical with the 0,0 pixel being defined by the upper left hand corner. In each radiograph, three slices were selected for model estimation. The slices used in this estimation are defined differently from those of Chapter 4. In this case, all of the slices initiate at the coordinate origin (92,187) in the image and continue radially to the edge of the image as defined by an angle, θ with respect to the horizontal. The angle, θ is positive clockwise from the horizontal. Thus, three slices of each radiograph were taken at the following angles:

ellipsoid 1 : θ = 0.14, 0.20, 0.27 radians

ellipsoid 2 : θ = 0.11, 0.18, 0.27 radians

spheroid : θ = 0.16, 0.23, 0.29 radians

The slices of the various samples are shown in Figs. 5.14-5.16. The horizontal axis is the detector position and the vertical axis is the digitized intensifier output. Each figure shows the three slices through the sample at the specified angles plotted together. The detector position has been calibrated to inches, measured on a line to the coordinate origin.

Notice how the skewness, width and intensity of the various slices changes as the slicing angle changes. The corresponding slices of projected distance through the aluminum versus detector position using the linear calibration curve of Eq. (5.8) are shown in Figs. 5.17-5.19. The slice data are now in the appropriate format for use as measurement data in the estimation procedure of Chapters 3 and 4.

In applying the estimation procedure of Chapter 3, the zero data on either side of the projection in each slice was removed and initial values were estimated for the elliptical parameters. The initial values were estimated using the stereographic reconstruction method of Chapter 2. In particular, initial values for the locations were estimated by reconstructing the location of the approximate centroid of the ellipsoid 1 sample. The two images used for the location computation were the reference image and the image with a 1.0 inch sample shift. Using the approximate centroids in the left and right images as feature points yielded a z-coordinate of approximately 15.7 inches and a radial offset of approximately 0.8 inches. The radial offset is defined as the distance along the slice line from the coordinate origin. The z-coordinate value is used as y_o and the radial offset is used as x_o in the 2-D reconstruction scheme.

The approximate magnification is thus, $m = D/(D - y_o) = 54.0/38.3 = 1.4$. The magnification was then used to estimate the elliptical semi-principal axis length,

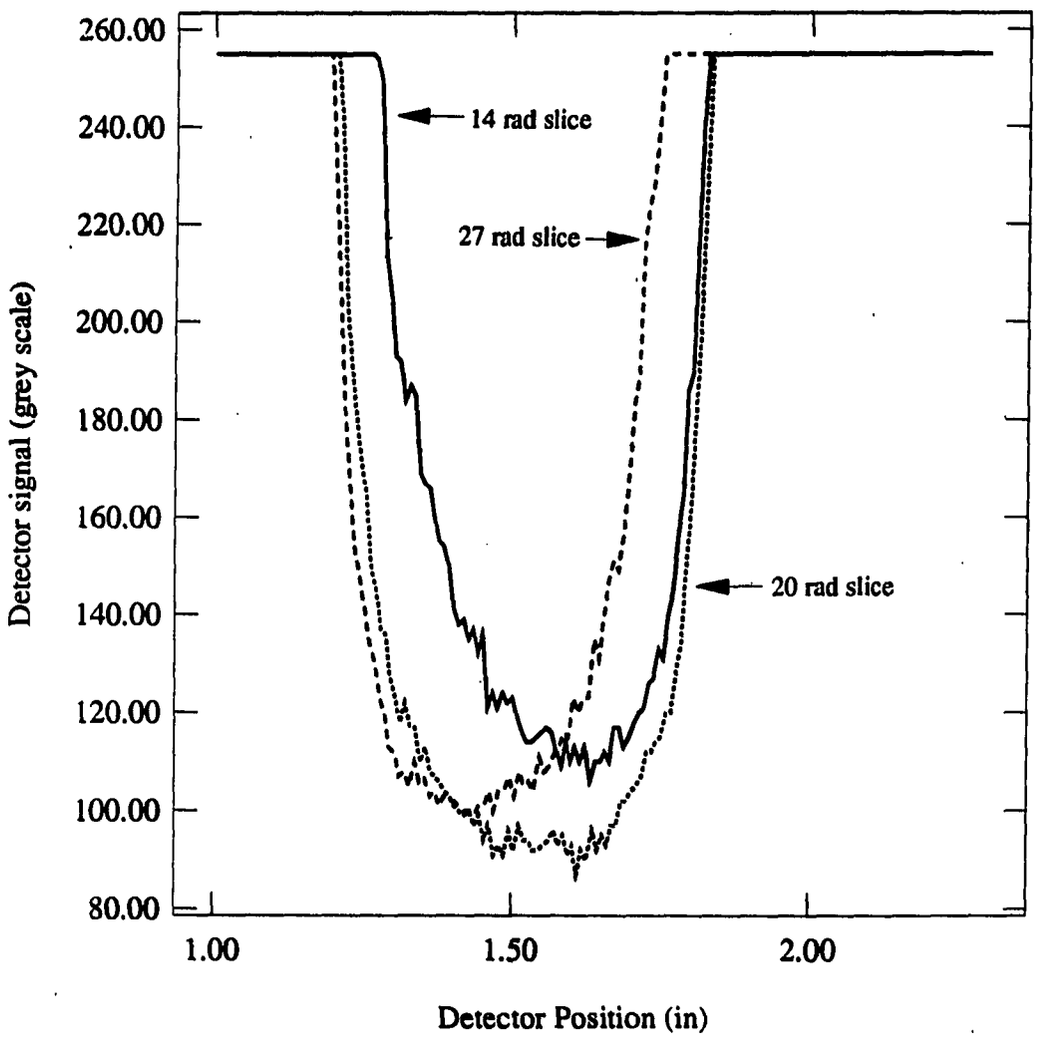

Figure 5.14: Slices of real-time radiograph of aluminum ellipsoid 1

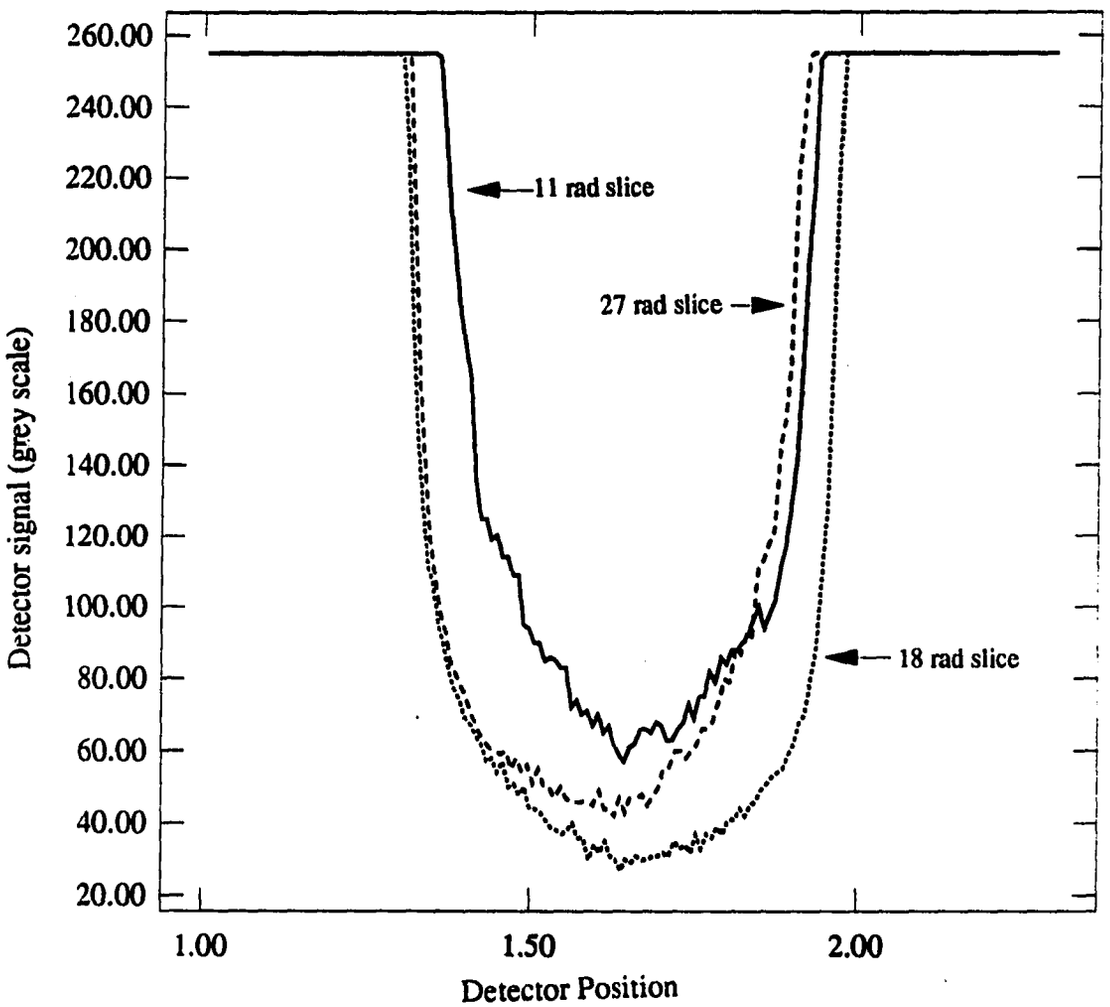

Figure 5.15: Slices of real-time radiograph of aluminum ellipsoid 2

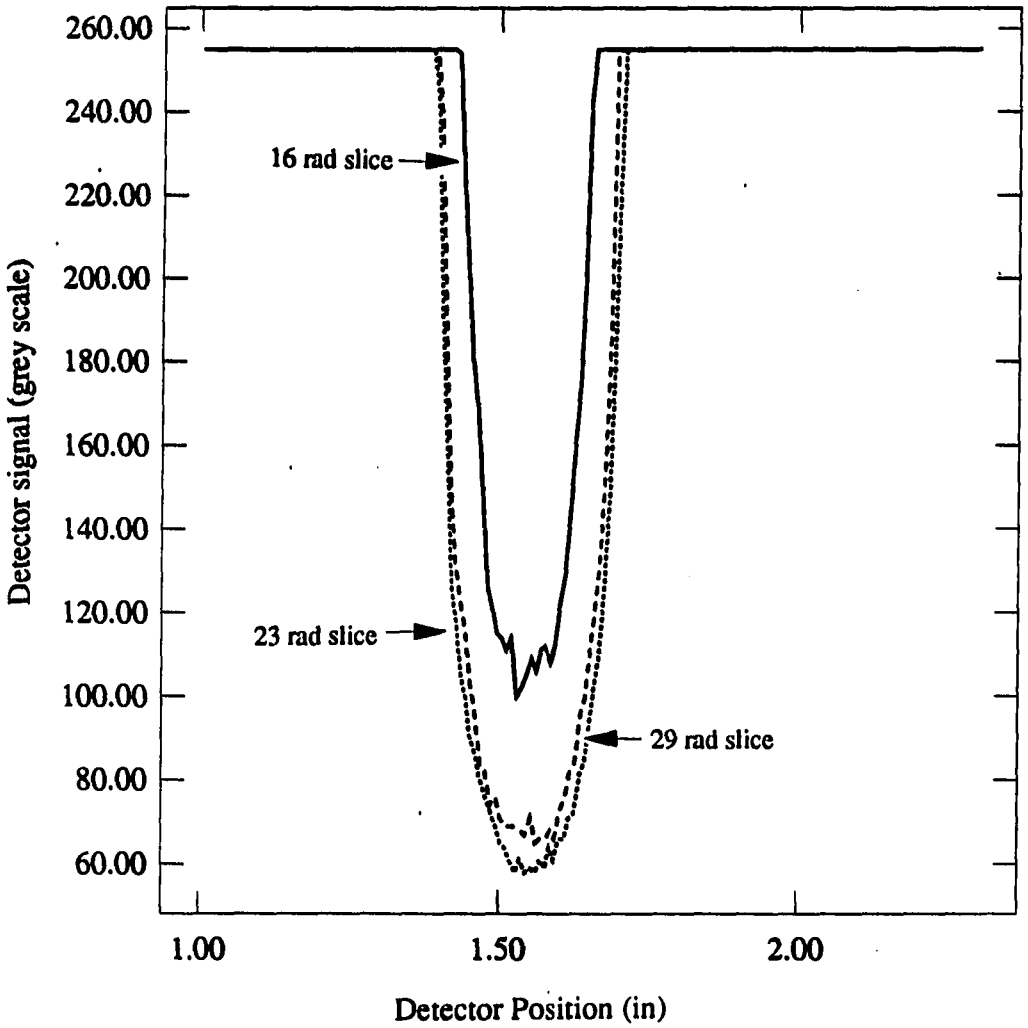

Figure 5.16: Slices of real-time radiograph of aluminum spheroid

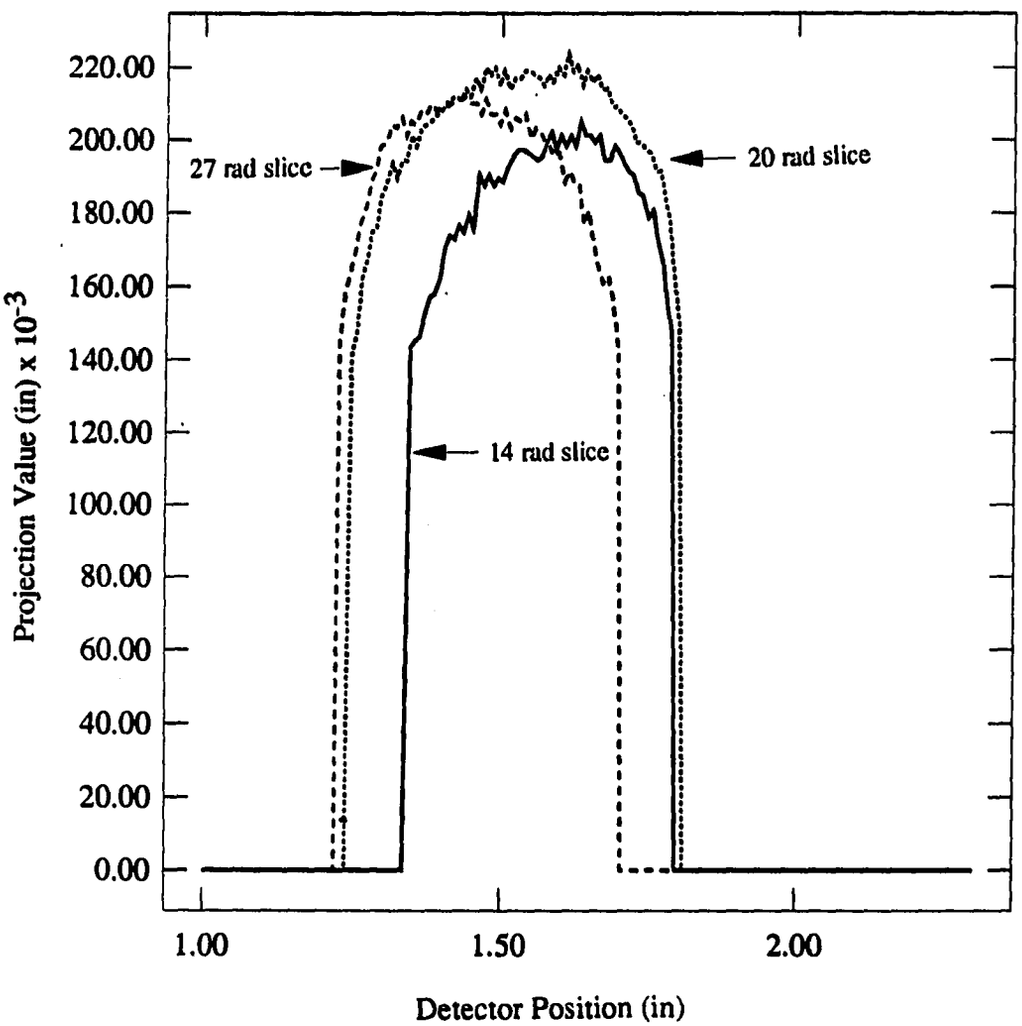

Figure 5.17: Calibrated slice data from radiograph of ellipsoid 1

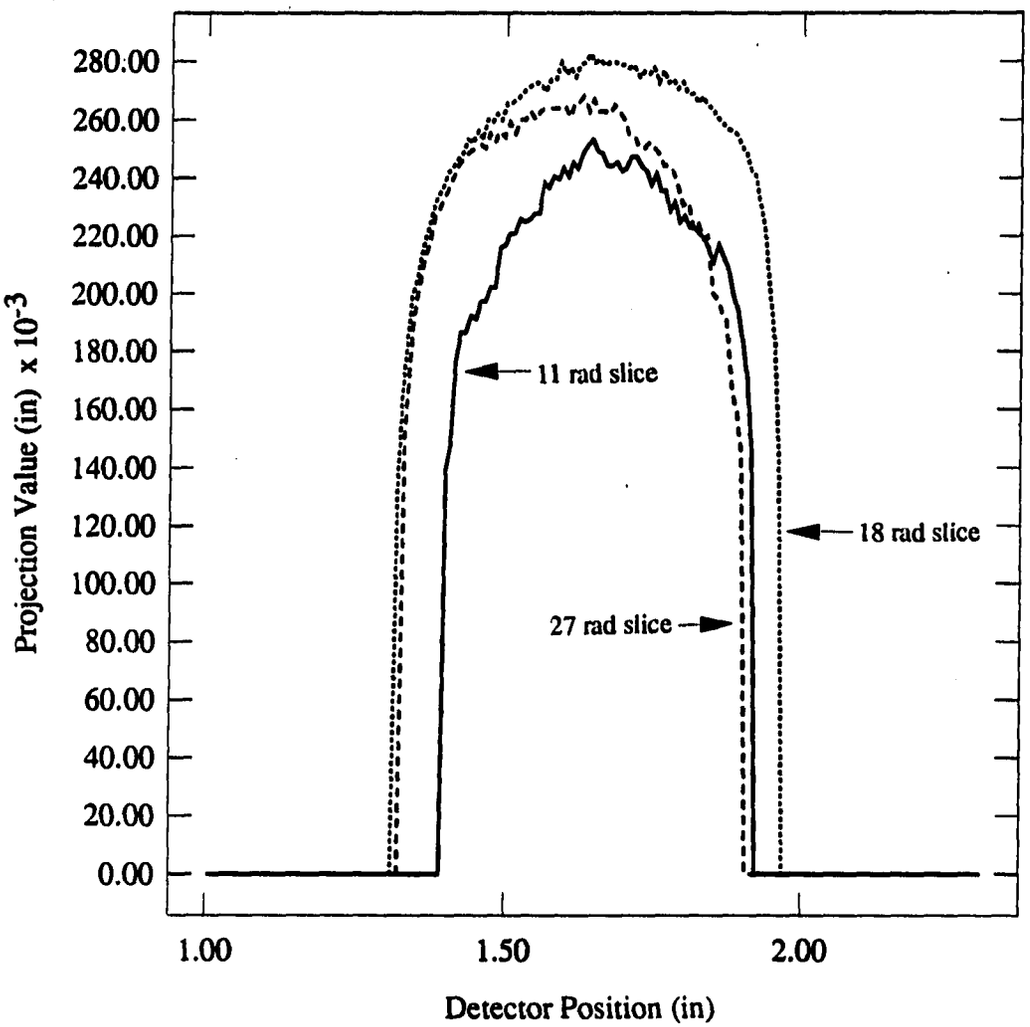

Figure 5.18: Calibrated slice data from radiograph of ellipsoid 2

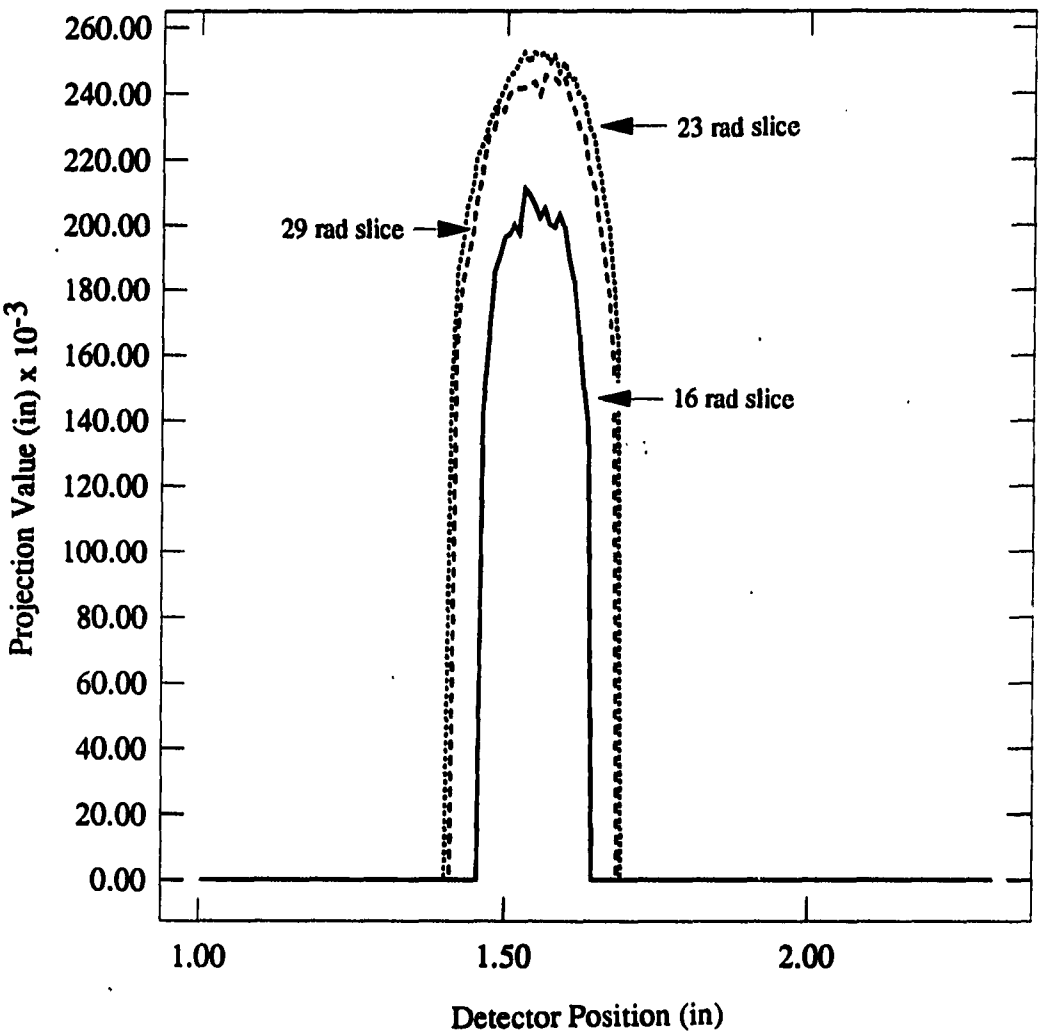

Figure 5.19: Calibrated slice data from radiograph of spheroid

a, as

$$a \approx 0.5\left(\frac{\text{extent of projection in image}}{m}\right) = \frac{1.8-1.3}{1.4} = 0.18 \text{ inches.} \qquad (5.9)$$

The extent of the projection in the image was obtained from the slice through the capsule sample at $\theta = 0.20$ radians The semi-principal axis length, b was estimated roughly as one half the maximum thickness of the sample. For the ellipsoid 1 sample with slice angle, θ=0.20 radians, this was approximately 0.12 inches. The initial value for the ellipse orientation was selected to be 0.0 radians arbitrarily.

This initial value estimation procedure was only applied once for the set of samples and slices since we do not require extremely accurate starting values in the estimation process. In the case of the aluminum sphere, however, the initial estimate of a was reduced by one half to reflect the decrease in the extent of the projection.

The Marquardt estimation procedure described in Chapter 3 was applied to three slices through each sample. The estimation summary is shown below for each reconstruction. All units of all lengths are inches and the units of angles are radians.

Ellipsoid 1 :

Slice $\theta = 0.14$: a = 0.17 b = 0.11 x_o = 1.12 y_o = 16.3 θ = 0.00 χ^2 = 2.1

Slice $\theta = 0.20$: a = 0.28 b = 0.10 x_o = 1.11 y_o = 16.0 θ = 0.00 χ^2 = 2.9

Slice $\theta = 0.27$: a = 0.19 b = 0.11 x_o = 1.10 y_o = 15.4 θ = 0.40 χ^2 = 2.3

Ellipsoid 2 :

Slice $\theta = 0.11$: a = 0.23 b = 0.11 x_o = 1.13 y_o = 15.8 θ = −0.92 χ^2 = 2.4

Slice $\theta = 0.18$: a = 0.30 b = 0.12 $x_o = 1.10$ $y_o = 16.3$ $\theta = -0.69$ $\chi^2 = 4.2$

Slice $\theta = 0.27$: a = 0.27 b = 0.11 $x_o = 1.14$ $y_o = 16.1$ $\theta = 0.77$ $\chi^2 = 2.8$

Spheroid :

Slice $\theta = 0.16$: a = 0.11 b = 0.07 $x_o = 1.12$ $y_o = 16.1$ $\theta = 1.60$ $\chi^2 = 0.58$

Slice $\theta = 0.23$: a = 0.14 b = 0.10 $x_o = 1.12$ $y_o = 16.3$ $\theta = 1.92$ $\chi^2 = 1.00$

Slice $\theta = 0.29$: a = 0.13 b = 0.10 $x_o = 1.11$ $y_o = 16.5$ $\theta = 1.72$ $\chi^2 = 1.20$

Error bounds are not given on the reconstructed values because of the unknown systematic error of the model fit.

The number of iterations used in the estimation was quite small ranging from 15 to 30. The number of measurement points in the slices ranged from approximately 40 to 80.

The results of the reconstruction appear reasonable. The estimated values are difficult to compare to the true values because of the non-ideal samples. The trends, however are correct in that the middle slice exhibits the largest value for a, and the y_o values are close to the measured value (15.5 $\pm$ 0.2 inches). In selecting the slice angles, the middle angle was chosen to cover roughly the largest extent of the projection. The outer two angles were selected to slice across more of the edge of the sample. The spherical sample data shows the best model fit as indicated by the lower values of χ^2. This is to be expected since the sample was almost perfectly spherical, and a sphere is a special case of an ellipsoid.

Plots comparing the fitted model to the measured projection data for the center slice of the three samples are shown in Figs. 5.20-5.22. In each case, the solid

line represents the measured projection data after calibration and the dashed line represents the projection of the fitted ellipse. Notice that the fit is fairly good in all cases although not perfect.

Much of the error between the fit and measurements is due to modeling error as opposed to measurement error. In this case, the modeling error is primarily caused by the non-ideal nature of the ellipsoidal samples as well as the error in calibration of the detector signal. For this reason, the Monte-Carlo method for determining confidence intervals on the parameters is of limited value. The Monte-Carlo method can show, however, that the model does not fit the data. Once this is known, confidence intervals obtained from the distribution of the estimated parameters are not meaningful. The distributions of the estimated parameters can be useful, however, in gaining knowledge of how sensitive the estimation is to random measurement noise.

Although the model does not technically fit the measurement data, it is still useful as an equivalent measure of the process. We can observe from Figs. 5.19-5.21 that the model does fit *reasonably well.* The term *reasonably well* is difficult to define since it is very qualitative. We see that the fit basically follows the trend of the measurements with no catastrophic deviations. It is difficult, however, to define quantitatively how well the model fits the data in any absolute sense. Comparing the nominal χ^2 value obtained from the initial estimation to the distribution of χ^2 generated from Monte-Carlo simulation will show it to be on the tail of the distribution. The question is, how far out on the tail must χ^2 be before we reject the model? One answer to this question is to develop an independent measure of *ellipsoidalness* from the measurement data. A possible measure of this is to model the boundary of the projection as a elliptical chain code (Basart 1990). A chain code is a code which

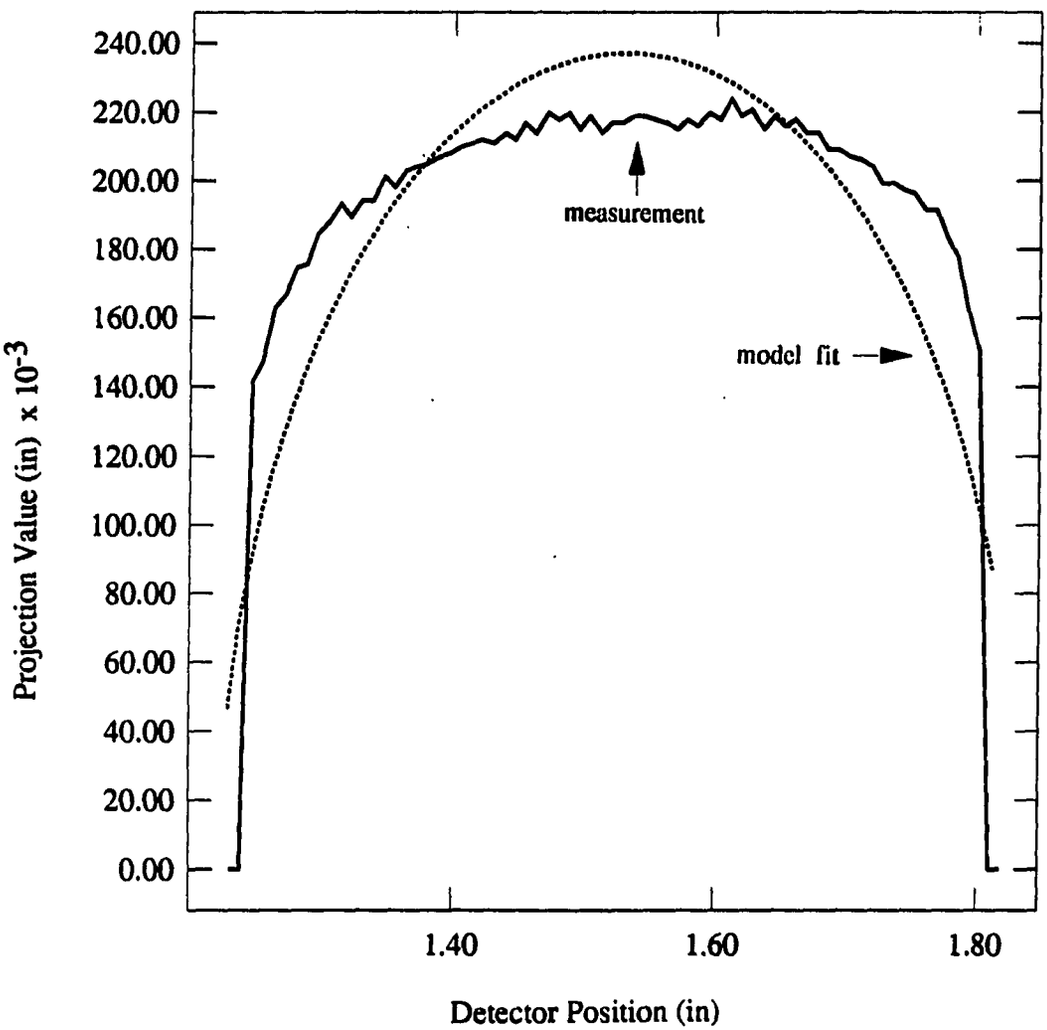

Figure 5.20: Comparison of model fit with measurements for ellipsoid 1

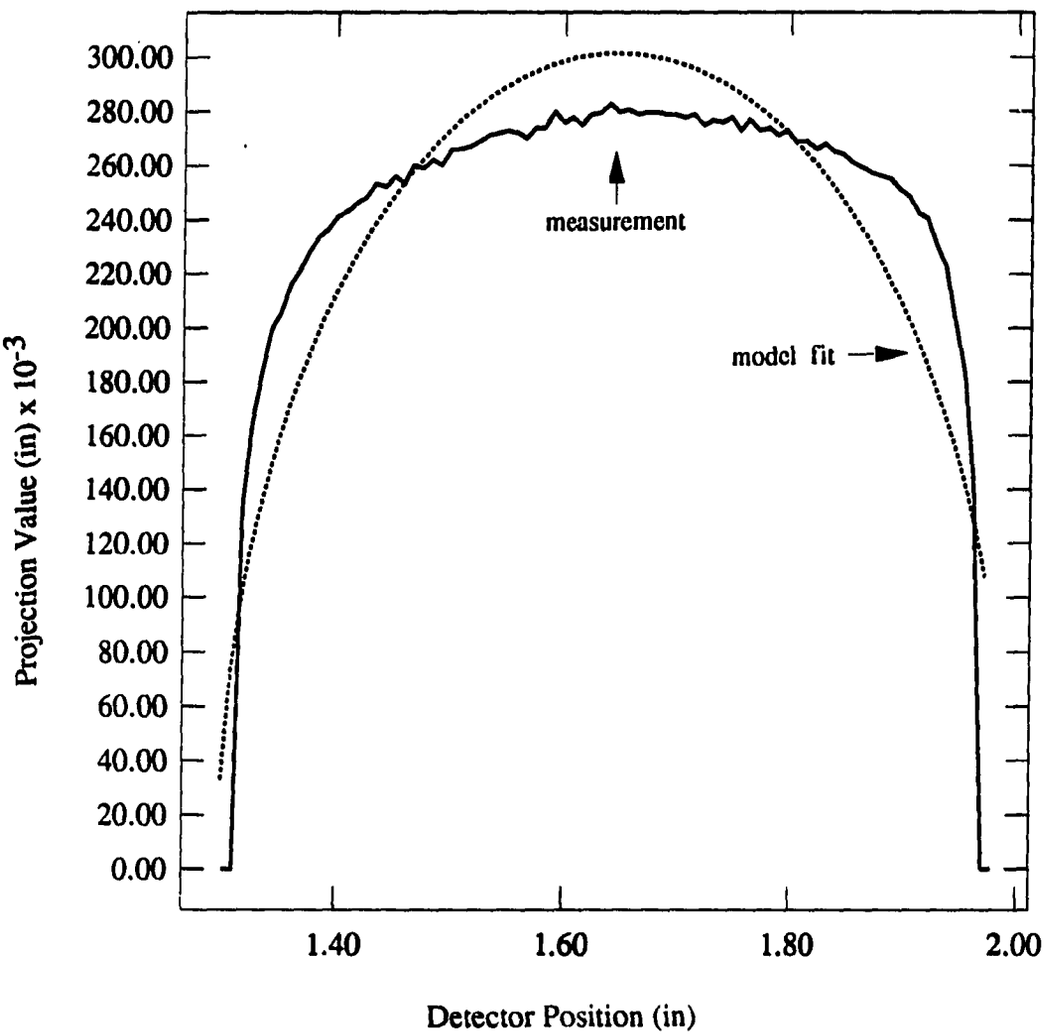

Figure 5.21: Comparison of model fit with measurements for ellipsoid 2

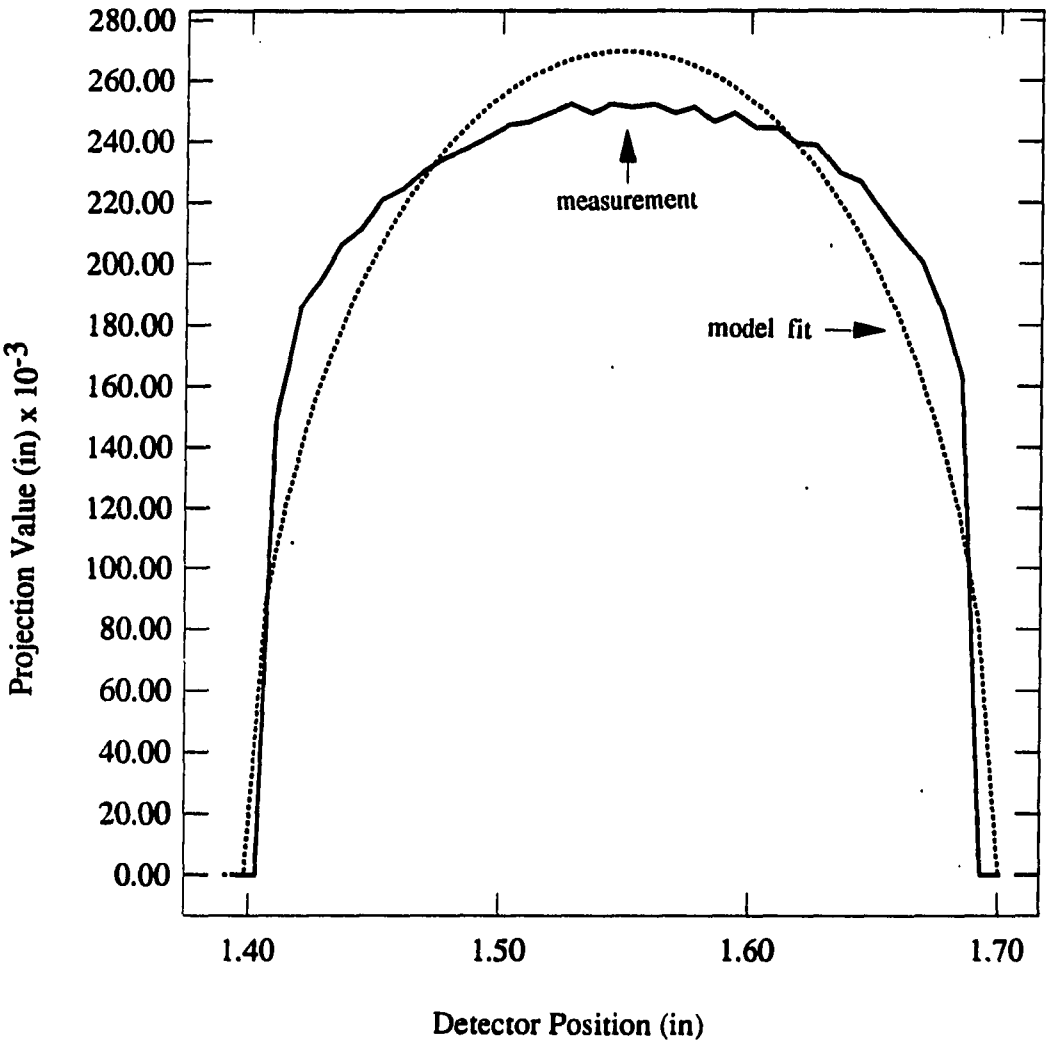

Figure 5.22: Comparison of model fit with measurements for spheroid

defines the direction of travel around some feature (Ballard and Brown 1982). The ideal elliptical chain code could then be compared with the chain code for the boundary of the measurements yielding some measure of model goodness. Another possible measure is to generate a distribution of χ^2 values for a wide set of measurement data whose variability comes from shape alterations (triangles, rectangles, parabolas, etc.) rather than measurement noise. A threshold of χ^2 could be set which would define the limit of acceptability for the model. Another approach is to simply observe the model fit and make a qualitative judgement as to its acceptability.

A Monte-Carlo simulation was performed using the reconstruction of the center slice of ellipsoid 1. Measurement simulations for 204 realizations of the parameters (a= 0.28 b=0.09 x_o=1.1 y_o=16.0 θ = 0.0). The realizations were made by using the noiseless projection data from the above parameters in the Poisson process defined by Eq. (3.54). In this simulation, the mean was the current projection value, and the value of λ was selected to be 0.002 by comparison of the measured noise level to the noise level produced by the simulation. The Poisson process was used because it has been shown that the noise of the x-ray generation combined with the noise due to the photon interaction with matter obeys a Poisson distribution (Macovski 1983). There is also a correlated noise process associated with the image intensifier detector which was not modeled. The distribution of χ^2 from the simulations is shown in Fig. 5.23. Notice that the value of χ^2 (2.91), is out on the tail of the distribution. In fact, it does not even appear to be part of the distribution.

This indicates that the modeling error is not explainable in terms of measurement error alone. In this case we accept the model anyway because the fit looks qualitatively reasonable. In addition, the value 2.91 is not all that far from the dis-

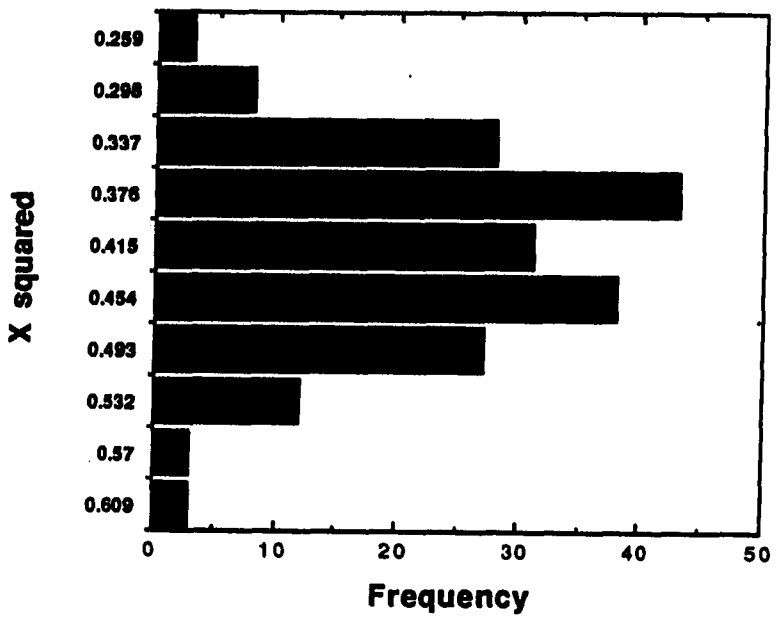

Figure 5.23: Distribution of χ^2 generated by Monte-Carlo simulation

tribution. If the value of χ^2 turned out to be 206.2, we would be tempted to question the model more. As stated earlier, the Monte-Carlo simulation used to generate the distributions of the estimated parameters is useful in determining how sensitive the model is to random fluctuations in the measurement process. In particular, for a typical photon counting noise process, we may wish to know the effect of signal-to- noise ratio on the estimation. It is useful to see if a parameter might change by 100% or more simply because of sensitivity of the model to a small measurement fluctuation.

The distributions of the estimated parameters presented in the form of scatter plots are shown in Figs. 5.24-5.28. The horizontal axis of each plot is the value of χ^2 and the vertical axis is the appropriate parameter.

Notice that in each distribution, the parameter values are scattered fairly nar-

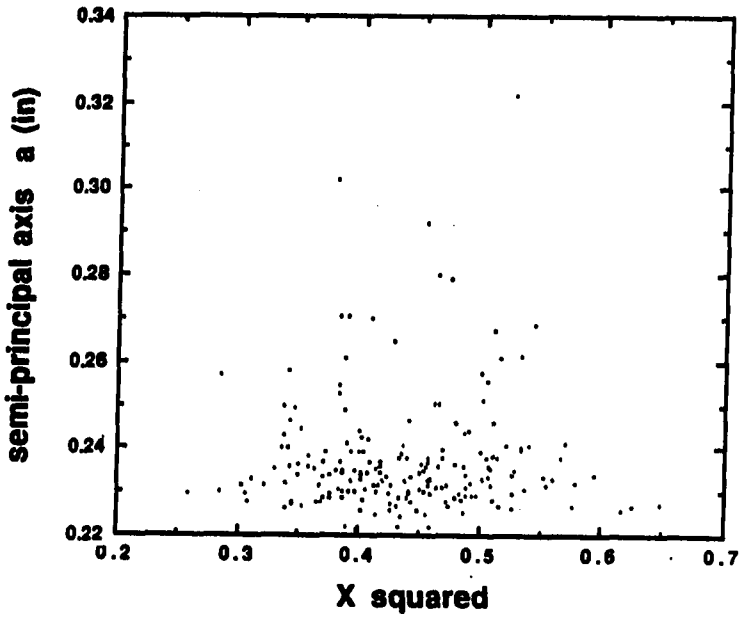

Figure 5.24: Scatter plot of a vs. χ^2 for 204 sample realizations

rowly around the nominal values. The distribution of y_o varies from approximately 15.8 to 16.4 inches. Thus the variability in the estimated y location of the elliptical slice due to measurement variability alone is about 0.6 inches. In some cases, this variability is acceptable. in other cases, it is not. If we are searching for locations of 0.05 inch diameter flaws inside a slab of material having a thickness of 1 inch the result would clearly be unacceptable. The variability can be reduced by reducing the source-to-detector distance. A 0.6 inch variability in a 54 inch source-to- detector distance is about 1%, which is actually very good. The best approach is to keep the source-detector distance as small as possible to keep the absolute variability of the estimated parameters as small as possible.

The distribution of the parameters a and b vary from approximately 0.22 in.

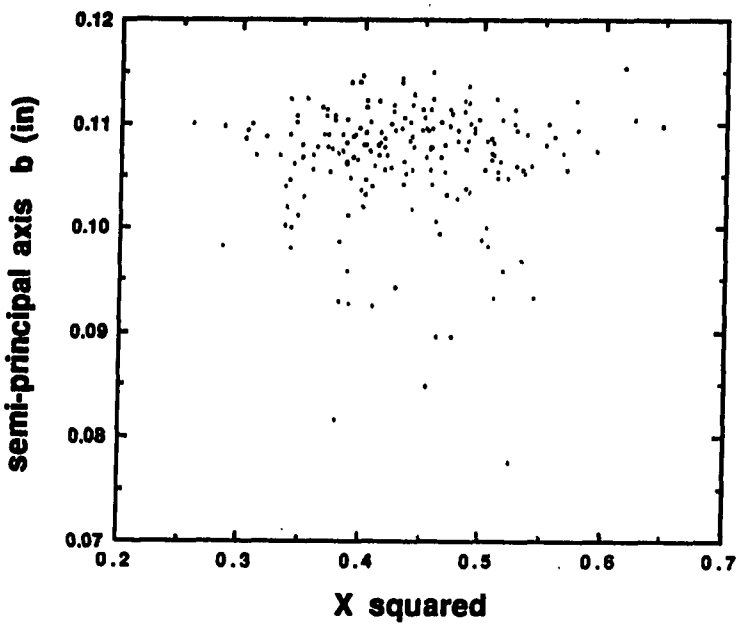

Figure 5.25: Scatter plot of b vs. χ^2 for 204 sample realizations

to 0.32 in. and 0.08 in. to 0.12 in., respectively. These variabilities appear to be reasonable given that the true values are approximately 0.25 in. and 0.13 in. In all cases except for b, the estimated parameters from the measurement data fall well within the distributions of the corresponding parameters in the Monte-Carlo simulation. Although the calculated value of b does not fall within the distribution, it is very close and the variability is small enough to deem the result acceptable. This is extremely encouraging, given the fact that the χ^2 value does not fall within its distribution. The distribution of θ is bi-modal due to the fact that all values between $\pi/2$ and π are not computed as negative angles. If we subtract π from all angles in the upper cluster of points, the distribution will be uni-modal about zero.

It would be useful to display the resulting elliptical slice reconstructions in a

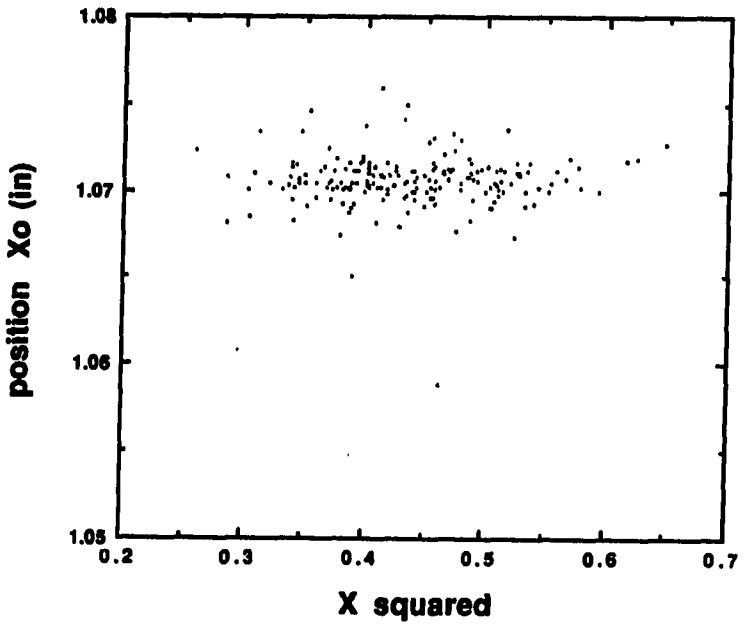

Figure 5.26: Scatter plot of x_o vs. χ^2 for 204 sample realizations

form similar to that of the simulated reconstructions at the end of Chapter 4. Unfortunately, this is not possible to perform in the scale of the measurement coordinate system. The method of display in Chapter 4 required a 3-D discrete grid of intensities in which the brightness at each grid location was controlled by a number in an array. The relatively large range of possible locations in the source-detector direction (54 inches) does not allow for adequate spatial resolution to display flaw structures on the order of 0.1 inch without an extremely large array size. At present, the 3-D array size is limited to 128x128x128 for display in this manner. In the future, however, a rendering program could be used to render an equivalent ellipse or ellipsoid as an approximate polygon and could display the result in any coordinate system.

An alternative measure of flaw shape and volume is to make an assumption as to

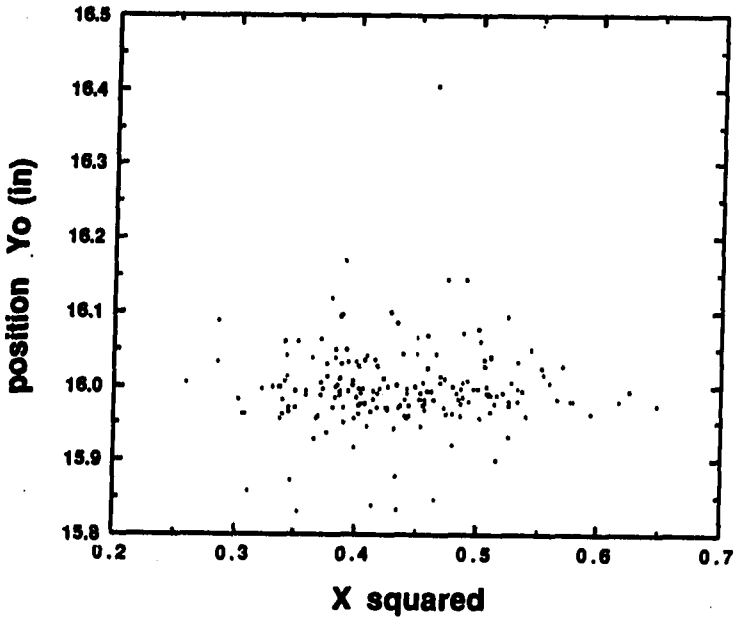

Figure 5.27: Scatter plot of y_o vs. χ^2 for 204 sample realizations

its shape and estimate the shape parameters which will define some three-dimensional quality, such as volume, from the spatial features of the projection. This is the basic idea of *stereology*. In *stereology*, however, there is the assumption of a distribution of objects to be quantified. This distribution tends to make the errors cancel out when dealing with the estimation of quantities such as total volume occupied by a distribution of objects. In our case, we do not have such a distribution. We simply must make an assumption, estimate the measurement errors and attempt to relate this to the error in the estimated quantity. For the objects under test in this chapter, it is reasonable to make assumptions that the object is ellipsoidal. We can estimate the semi-principal axes lengths from measurements of the lengths across the projection and the magnification. We can then estimate the volume by either

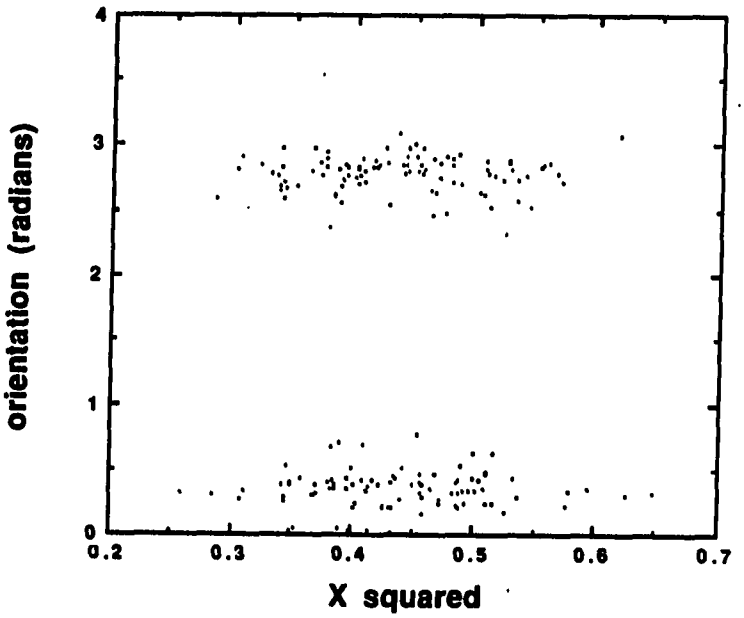

Figure 5.28: Scatter plot of θ vs. χ^2 for 204 sample realizations

assuming an ellipsoid of revolution or using the detector intensity to determine a third principal axis length. If we assume an ellipsoid of revolution, the volume estimation requires only spatial measurements of two principal axes lengths from the projection. However, this assumption is more susceptible to modeling errors since we may be viewing a three axis ellipsoid. Thus, if calibrated distance measurements for the projections are available, it is advantageous to use these measurements to estimate the third principal axis. Modeling errors can also occur due to the orientation of the object under test. If an ellipsoid has nonzero orientation with respect to the measurement system coordinate axes, the projected principal axes lengths will appear foreshortened. This foreshortening will cause an error to occur in the principal axes and volume computations. However, the use of the calibrated projection distance

measurements from the detector signal can help reduce this error by bringing in information about the thickness of the ellipsoid.

This type of modeling and volume analysis has been performed on each of the three samples discussed earlier. The magnified principal axes lengths were measured in the images by observing the pixel locations of the leftmost, rightmost, uppermost, and lowermost points of the projected samples. The centroids of the features were defined by the midpoint between these four extremes. The coordinates of the centroids in the images were converted to absolute distance measurements on the detector plane using the using the distance calibration factors given by

$$k_x = 0.0081 \text{ inches per pixel}$$

$$k_y = 0.0068 \text{ inches per pixel.}$$

These factors were obtained from the calibration disk discussed in Chapter 2. Next, the locations of the sample were estimated using the centroid coordinates in the images and the total least squares estimator of Chapter 2. The estimated locations in terms of distance from the detector were

$$\text{Ellipsoid 1}: \quad \text{d} = 15.3 \text{ in.} \pm 0.8$$

$$\text{Ellipsoid 2}: \quad \text{d} = 15.0 \text{ in.} \pm 0.8$$

$$\text{Spheroid} \quad : \quad \text{d} = 15.3 \text{ in.} \pm 0.8$$

The corresponding estimated magnifications of each sample using Eq. (1.1) were

$$m_{\text{ellipsoid 1}} = 1.40 \pm 0.06$$

$$m_{\text{ellipsoid 2}} = 1.38 \pm 0.06$$

$$m_{\text{spheroid}} = 1.40 \pm 0.06.$$

The lengths and widths across each projection for the various samples were

Ellipsoid 1 :

x : 83 pixels ± 2 = 0.676 in ± 0.016

y : 47 pixels ± 2 = 0.319 in ± 0.014

Ellipsoid 2 :

x : 85 pixels ± 2 = 0.693 in ± 0.016

y : 58 pixels ± 2 = 0.394 in ± 0.014

Spheroid :

x : 43 pixels ± 2 = 0.350 in ± 0.016

y : 52 pixels ± 2 = 0.353 in ± 0.014

The estimated principal axes lengths for each case after correction for magnification, using

$$\text{axis length} = \frac{\text{projected axis length}}{m}, \tag{5.10}$$

was thus,

Ellipsoid 1 : $A = 0.24$ in ± 0.03 $B = 0.12$ in ± 0.02

Ellipsoid 2 : $A = 0.25$ in ± 0.04 $B = 0.14$ in ± 0.02

Spheroid : $A = 0.13$ in ± 0.02 $B = 0.13$ in ± 0.02,

where A and B are the horizontal and vertical semi-principal axes lengths, respectively. The uncertainties in each case were computed by determining upper and lower bounds for the computed quantities from the upper and lower bounds on the quantities used in the formulas. Estimates of the third semi-principal axis length along

the x-ray line of sight were obtained from the calibration function of Eq. (5.8). The grey scale detector output at the centroid locations for each sample were

$$\begin{aligned}
&\text{Ellipsoid 1 : Detector output at } (109, 227) = 75 \\
&\text{Ellipsoid 2 : Detector output at } (125, 227) = 23 \\
&\text{Spheroid : Detector output at } (114, 234) = 31,
\end{aligned}$$

yielding estimates of

$$\begin{aligned}
&\text{Ellipsoid 1 : } C = 0.12 \text{ in } \pm 0.01 \\
&\text{Ellipsoid 2 : } C = 0.15 \text{ in } \pm 0.01 \\
&\text{Spheroid : } C = 0.14 \text{ in } \pm 0.01.
\end{aligned}$$

The uncertainties on C were computed from the local standard deviation of detector signal near the centroid. In each case, the local standard deviation was approximately three. The errors caused by calibration have been ignored here.

The volume of the ellipsoidal model can now be computed as (Beyer 1981)

$$V = \frac{4}{3}\pi ABC \tag{5.11}$$

Computing the volumes from the semi-principal axes estimates above yields

$$\begin{aligned}
&\text{Ellipsoid 1 : } V = 0.0145 \text{ in}^3 \pm 0.0061 \\
&\text{Ellipsoid 2 : } V = 0.0213 \text{ in}^3 \pm 0.0097 \\
&\text{Spheroid : } V = 0.0099 \text{ in}^3 \pm 0.0042.
\end{aligned}$$

The true volumes of each sample are

$$\text{Ellipsoid 1 : } V_{\text{true}} = 0.0191 \text{ in}^3 \pm 0.0001$$

$$\text{Ellipsoid 2}: \quad V_{true} = 0.0258 \text{ in}^3 \pm 0.0002$$

$$\text{Spheroid} \quad : \quad V_{true} = 0.0085 \text{ in}^3 \pm 0.0001.$$

The true volumes were measured by weighing them with a precision scale and using the density of aluminum. The density value used for aluminum was 2.70 g/cm^3 $\pm$0.01 The scale was accurate to $\pm$ 0.0002 g. Thus, the uncertainty on the measurements was practically zero compared to the uncertainty on the estimates. The measured masses of the samples were

$$\text{Ellipsoid 1}: \quad m = 0.8460 \text{ g} \pm 0.0002$$

$$\text{Ellipsoid 2}: \quad m = 1.1443 \text{ g} \pm 0.0002$$

$$\text{Spheriod}: \quad m = 0.3747 \text{ g} \pm 0.0002.$$

Notice that the computed volumes are fairly close to the true volumes (within the predicted uncertainties). In an actual inspection setting, the volume measurement is usually not as useful as the separate axes measurements for an ellipsoidal model. Typically, the criterion for maximum allowable flaw size in a part is specified in terms of a length, diameter or thickness.

5.3.2 Aluminum Cylinder

The analysis procedures of the previous section were implemented identically on an aluminum cylindrical sample. The purpose of the cylindrical sample was to test the procedures on a sample that was not as close to being ellipsoidal. The cylinder had a diameter of 0.25 $\pm$0.005 inches and a length of 0.25 $\pm$0.005 inches. Three radiographs of the cylinder were produced under identical circumstances as

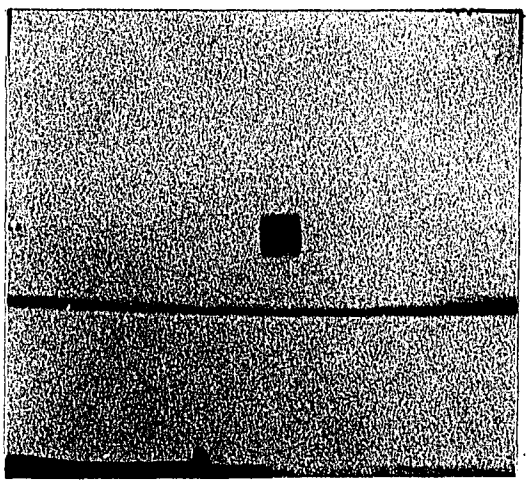

Figure 5.29: Real-time radiograph of aluminum cylindrical sample

the ellipsoidal samples. A photograph of the real-time radiograph of the cylindrical sample at a shift of 1.0 inch is shown in Fig. 5.29. Again, the background is saturated because the sample has been placed in free space with no surrounding attenuating material.

Plots of three slices through the radiograph at angles 0.18, 0.23 and 0.30 radians are shown in Fig. 5.30. In this figure, the vertical axis is the detector output signal and the horizontal axis is the detector position. Notice the skewed nature of the slices caused by the discontinuity of the cylinder at its ends. The corresponding slices after calibration using Eq. (5.8) are shown in Fig. 5.31.

These slices were used in the elliptical model estimation routine as described in the previous section yielding the following results.

Slice $\theta = 0.18$ a = 0.12 b = 0.11 $x_o = 1.1$ $y_o = 15.9$ $\theta_o = 3.30$ $\chi^2 = 2.3$

Slice $\theta = 0.23$ a = 0.12 b = 0.13 $x_o = 1.1$ $y_o = 16.2$ $\theta_o = 1.07$ $\chi^2 = 2.7$

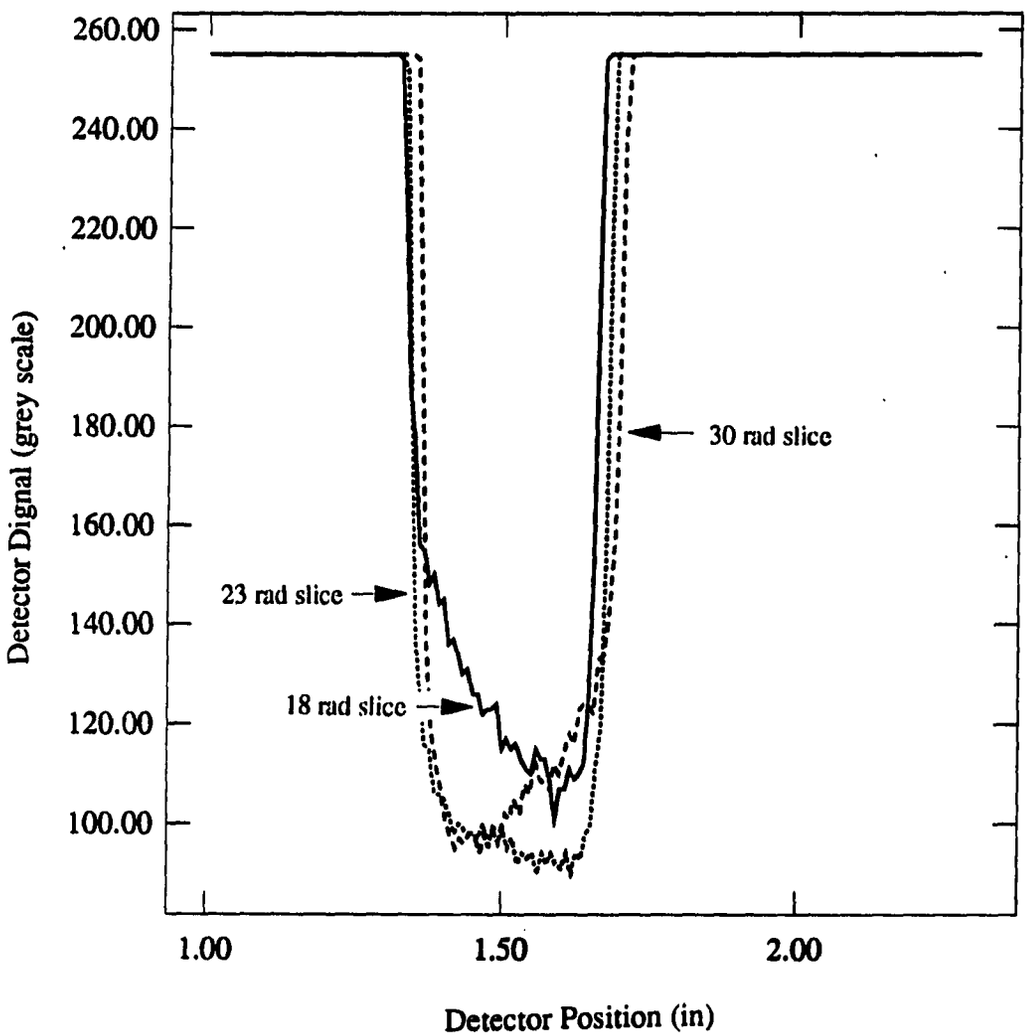

Figure 5.30: Slices through real-time radiograph of aluminum cylindrical sample

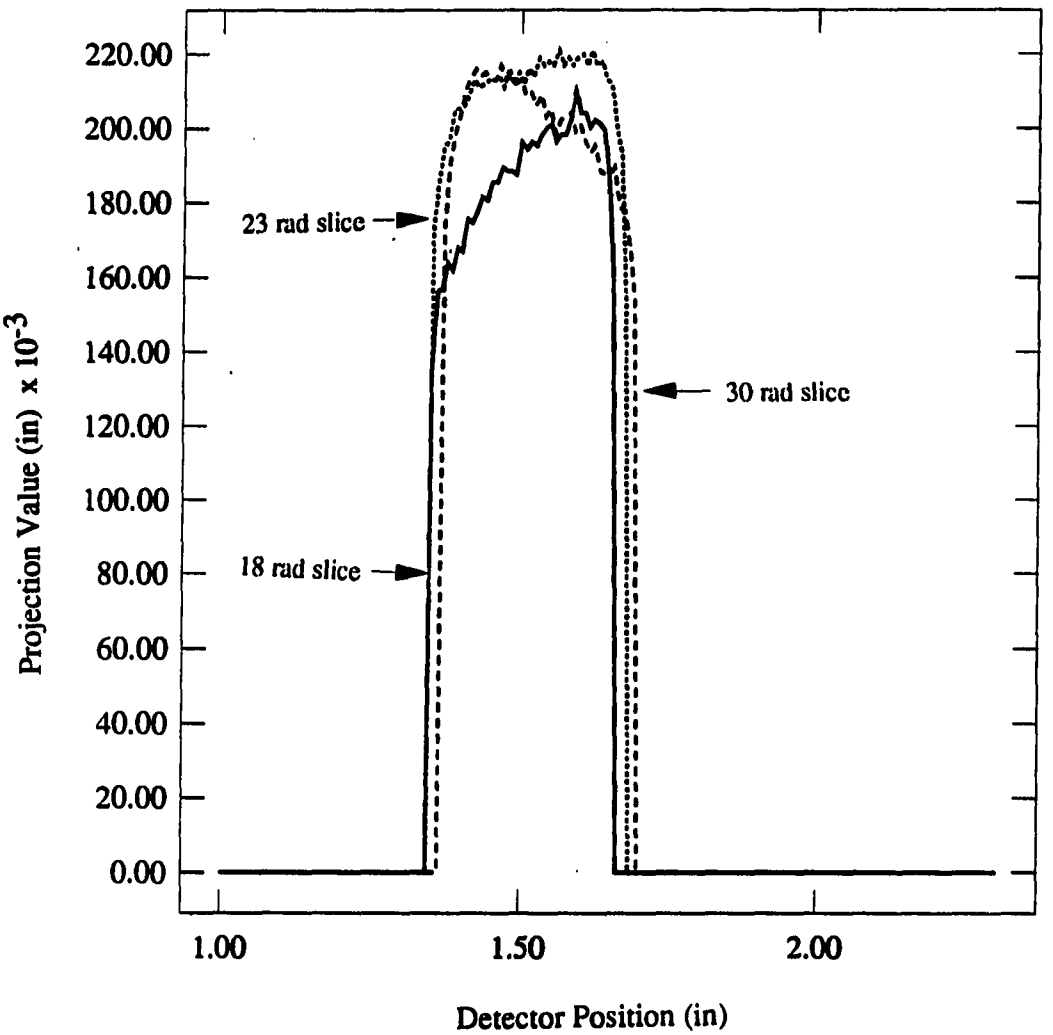

Figure 5.31: Calibrated slices through aluminum cylindrical sample

Slice $\theta = 0.30$ a = 0.15 b = 0.10 $x_o = 1.1$ $y_o = 16.4$ $\theta_o = 0.88$ $\chi^2 = 2.6$

(Note: Length units are inches and angle units are radians.) Initial values were obtained in the same manner described above. Again, the results are reasonable, with the fitted principal axes being near the true value of the radius of the cylinder (0.125 in). The location, parameter, y_o has overestimated the true value (15.5 in) in each case, however, this could be attributed to modeling error and calibration error. A plot of the fit for the slice, θ=0.23 is shown in Fig. 5.31. Notice that the fitted projection does not follow the measurement data as well as the previous samples. For this situation, it is useful to obtain estimates directly from the shape of the projection and the estimated magnification.

The measured length and breadth of the projection of the cylinder are

$$\text{length} = 44 \text{ pixels } \pm 2 \;=\; 0.359 \text{ in } \pm 0.016$$

$$\text{breadth} = 47 \text{ pixels } \pm 2 \;=\; 0.319 \text{ in } \pm 0.014.$$

The estimated distance from the detector, using stereographic reconstruction of the approximate centroid is

$$y_o \;=\; 15.3 \text{ in } \pm 0.8,$$

yielding an estimated magnification of

$$m \;=\; 1.41 \;\pm 0.04.$$

Correcting the length and breadth estimations for the magnification yields

$$\text{Sample length} \;=\; 0.26 \text{ in } \pm 0.02$$

$$\text{Sample breadth} \;=\; 0.23 \text{ in } \pm 0.02$$

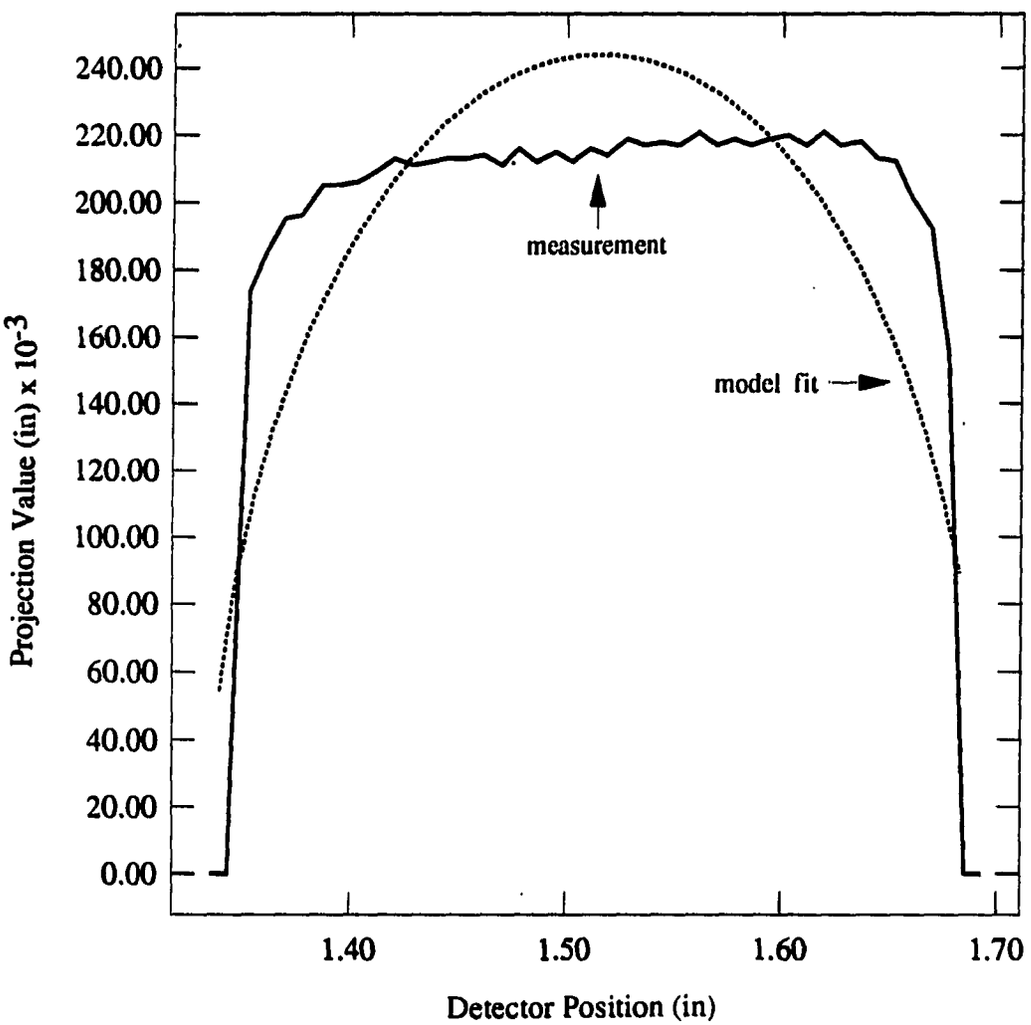

Figure 5.32: Fit of elliptical model to cylindrical slice data

The grey-scale detector signal at the sample centroid was 76, yielding a thickness estimate of 0.23 inches ± 0.01. Again, this estimate was obtained from the calibration formula of Eq. (5.8). The uncertainty was computed from the local standard deviation of the detector signal near the centroid.

These estimates compare well with the true values. We can use them in a volume computation for an equivalent ellipsoid or cylinder. The equivalent ellipsoidal volume is given by

$$V_e = \frac{1}{6}\pi \cdot \text{length} \cdot \text{breadth} \cdot \text{thickness}, \tag{5.12}$$

yielding the result, $V_e = 0.0072$ in^3 ± 0.001. The equivalent cylindrical volume is given by

$$V_c = \frac{\pi}{4} \cdot \text{breadth}^2 \cdot \text{length}, \tag{5.13}$$

yielding the result, $V_c = 0.011$ in^3 ± 0.003. The measured volume of the cylindrical sample was 0.0125 in^3 $\pm$ 0.0001. Notice that the computed cylindrical volume is much closer to the true volume (12%error as opposed to 42%).

In the next section, we discuss the various trade-offs and limitations associated with the elliptical slice modeling and the stereology-based modeling methods.

5.4 Practical Limitations and Discussion

There are many practical limitations associated with the modeling and estimation procedures used in this chapter. Among these limitations include the detector calibration accuracy, measurement accuracy, orientation dependency of the projections, and estimation time.

The detector intensity calibration is extremely important to obtaining good estimation results from the elliptical slice model. The calibration process converts the

actual detector signal into x-ray projection distances. These distances are used for the measurement data in the estimation procedure for modeling the data as elliptical slices. The integrity of this data strongly affects the result of the estimation. In the test cases used in this dissertation, the calibration was relatively easy to perform as the sample was in free space with no surrounding material. When there is surrounding material, an assumption must be made about the flaw material composition. This type of calibration also assumes that there are no occluding flaws. In cases where there are occluding flaws, the orientation of the sample must be changed. It would be useful in future research to study the image formation process of the real-time image intensifying detector in order to develop better models for use in the calibration.

Measurement accuracy is of prime importance to obtaining accurate results in both the elliptical slice estimation and the stereological modeling. In particular, the accuracy of measurements of the feature coordinates and distances on the detector have the largest effect on the accuracy of the results. This measurement accuracy becomes even more important when the source-detector separation distance is large. For this reason, great care and precision must be used while performing the radiography so that the propagation of measurement errors does not dominate the quantities being estimated. A key to determining the practical limitations caused by measurement inaccuracies is to use Eqs. (2.40) and (2.43)-(2.47) for the particular inspection geometry, thus determining how the errors propagate through to the estimates.

The dependency of the projected sample on its orientation create a limitation in terms of both modeling and detectability. In theory, the elliptical slice modeling procedure can account for a wide variety of ellipsoidal shapes of different orientations. A situation can occur, however where the ellipsoidal thickness along the direction of

the x-ray path is not sufficient to generate a detectable signal. In other cases, the orientation may be such that the dynamic range of the detector is exceeded. A possible solution to this problem is to re-orient or shift the sample such that the detector signal is acceptable. When estimating the ellipsoidal parameters from the shape measurements and magnification, as in the stereological modeling, it is wise to make at least two projections (which are required anyway) to see if any dramatic foreshortening of the flaw axes is taking place.

Finally, one of the limitations associated with estimating model parameters is time. This is also one of the trade-offs between the elliptical slice model estimation and the stereological modeling. Performing the elliptical slice estimation requires that a series of calibrated slices be extracted from the digitized radiograph followed by an iterative estimation process for each slice. This method can be time consuming compared to stereological modeling. The information gained, however is more detailed and is potentially more accurate. The question is, does the increase in information and potential accuracy justify the time and expense? This is a difficult question to answer and is addressed in the following chapter.

6. SUMMARY AND CONCLUSIONS

The goal of this dissertation has been to develop and implement techniques to determine size and location information about flaws from x-ray inspection with a small number of views. The motivation behind this goal has been to overcome limits of inspectability when the geometry of the inspection is such that data collection from many angles is impossible or impractical. In addition, the reduction in cost and time associated with acquiring and processing a fewer number of projections has been another motivation. To this end, techniques have been developed which reconstruct or estimate a model of the flaw rather than reconstruct the actual flaw.

The types of flaws under consideration in this dissertation have been crack-like flaws, or flaws which have a wandering or meandering nature with easily identifiable characteristic points, and volumetric flaws, which have relatively smooth boundaries and have an anomalous absence or presence of material. The philosophy behind the reconstruction of these types of flaws has been to model them by a geometric shape and derive equations which produce the x-ray projection of the model. These equations are then used with measured projection data to estimate best-fit model parameters.

In the case of crack-like flaws, the geometric model has been a discrete point or a series of points that when connected, yield a piecewise linear curve. This type

of model is justified because a crack is generally viewed as an extremely localized feature that tends to wander around. When stereographic projections are made, it is easier to identify corresponding points between the two images. These (and other) corresponding points are used with a linear model of the stereo point-projecting process to estimate the 3-D locations of the points. The locations of the points are estimated using a least-squares or total least-squares estimator. The linear model is formulated in such a way as to allow the use of more than two projections and to allow the estimation of as many points as desired. The projection model has also been used to derive expressions relating the errors in the estimated parameters to the measurement errors. These equations are extremely useful in giving the NDE practitioner confidence in his/her results..

The estimation procedure has been applied to several inspection scenarios ranging from fabricated test samples in the laboratory to industrial railroad frogs in the field. The results of the procedure on the laboratory samples have been encouraging with the results being correct within the bounds of experimental error. The results in the case of the railroad frogs are still inconclusive. At this time, new radiographs of a frog after failure have been produced. Destructive sectioning is planned to compare the true flaw locations to the estimated locations. This correlation will provide a more conclusive answer as to the applicability of this technique to situations in the field. The success of the procedure as it is applied to laboratory samples indicates that a positive correlation is likely.

In the case of volumetric flaws, two modeling approaches have been used. The first approach models the flaw as an ellipsoid having arbitrary principal axes lengths, orientation angles and location. Slices of the ellipsoid (ellipses) are reconstructed

from measured projection data along straight lines in the detector plane. Originally, it was intended that a full 3-D ellipsoid would be reconstructed from the full set of data in the measurement plane. This turned out to be an extremely difficult prospect, therefore, the problem was broken into several, simpler 2-D elliptical slice reconstructions. Instead of an optimization problem in 9 dimensions, the problem was reduced to a series of optimization problems in 5 dimensions.

The second approach to modeling volumetric flaws has been to use concepts from stereology in which the flaw is modeled as a geometric solid such as an ellipsoid, cylinder, cone, etc. The model parameters are then estimated from the *shape* of the projections. This type of modeling is more susceptible to orientation dependent errors since it does not necessarily use the thickness information along the line of sight of the x-ray. However, when one uses the thickness information, the model can be adjusted to reflect the true shape. For instance, if one originally assumes an ellipsoid of revolution ($A \neq B=C$) for the model of a flaw, and discovers that the thickness (2C) of the ellipsoid is not equal to 2B, then the ellipsoid model can be changed to a three-axes ellipsoid, resulting in a much more accurate description. The use of stereology modeling also makes the error analysis easier. All of the model parameters must be corrected for magnification, which is determined from the stereographic projection methods of Chapter 2. The error analysis procedures developed there can be directly carried over to determining approximate error bounds for the model parameters. It is difficult, however to determine the modeling error. Much work has been done previously in generating modeling error bounds when the error is caused by the mismodeling of known figures by other known figures (Russ 1986). Related work has generated error bounds for various models caused by mismodeling as a result of

orientation errors.

Both modeling methods have been implemented and applied to several fabricated aluminum test samples. The results of the reconstruction of 3 slices through each sample has yielded results which are acceptably close to the true values. We define acceptable here as within 5% of the true location (with respect to the source-detector separation distance) and within 20% of the true model shape parameters. It is difficult to measure the true parameter values because the samples are very small, and the samples are not ideal in terms of the model anyway. The θ parameter is especially difficult to interpret because the two semi-principal axes lengths are nearly equal in most cases. Bounds on the estimation error due to random measurement fluctuations (Poisson noise) have been determined for one case through a Monte-Carlo simulation. The main problem with this type of error analysis is that it does not take into account the modeling error, and it is extremely laborious to implement for each reconstruction. We cannot say that a certain parameter has a certain confidence interval, because the model that parameter is a part of, may not fit the data at all. Still, the parameter distributions are useful in determining the sensitivity of the estimation to small fluctuations in the measurements.

The stereolgy-based modeling methods have also been implemented on the test samples with very good results. In particular, the shape parameters for the ellipsoid and cylinder models are very close to the measured values (within estimated uncertainties). Although the samples were radiographed with no foreshortening of the axes, this method appears extremely attractive for describing flaw characteristics.

The trade-offs between the two volumetric flaw modeling methods are speed and information. The elliptical slice modeling method provides more detailed information

in terms of the best-fit elliptical parameters through some slice of a flaw. If a large number of slices is used, the entire flaw can be covered and a composite shape can be rendered. The problem with this approach is that it takes time. It is questionable if the typical NDE practitioner can utilize all of this information. On the other hand, scientists in the field may eventually require more and more detailed information about a flaw when CT techniques are not possible. The composite method can potentially serve this need. The question of model accuracy also plays a key role in determining the method's applicability to real inspection data. Some threshold of model goodness should be invented to specify when to throw out the model. It seems at this point that the method gives you more information than you need to know. Most practitioners don't care how well the flaw data fits an ellipsoid as long as they know approximately where the flaw is and how big it is. Given these statements, the stereology method appears to be very attractive for computing the important flaw measures while avoiding complexities associated with nonlinear optimization and detector calibration.

The elliptical slice modeling method should still be pursued as a research tool that can continue to be refined as more and more quantitative information is required from the inspection. There are many areas of research that must be investigated to continue this refinement. Of particular importance is a study of the real-time detector model. Because the real-time detector is the most attractive means of acquiring an image quickly, its use should be incorporated in this work. Another area that should be investigated is the inspection of complicated part geometries. Joe Gray, and others (Gray and Inanc 1989) have developed an x-ray simulation program that models the x-ray generation process, the x-ray interaction with a complicated part

geometry, and the image formation process. This type of software could be used to allow the ellipsoidal model to be embedded in some complicated part. Finally, it would be useful to attempt the use of a 3-D ellipsoidal model with a fewer number of parameters. Reduction of the number of allowed orientation angles and principal axes lengths may allow the nonlinear optimization process to be practical for the full 3-D shape.

7. BIBLIOGRAPHY

Aloimonos, J.Y. and Hervé, J.Y. 1990. *Correspondenceless stereo and motion: planar surfaces.* IEEE Transactions on Pattern Analysis and Machine Intelligence, 12:504-510.

Andersen, A. 1989. *Algebraic reconstruction in CT from limited views.* IEEE Transactions on Medical Imaging, 8:50-55.

Bain, L.J. and Engelhardt, M. 1987. *Introduction to Probability and Mathematical Statistics.* PWS Publishers, Boston, MA.

Ballard, D.H. and Brown, C.M. 1982. *Computer Vision* Prentice-Hall, Englewood Cliffs, NJ.

Basart, J.P. 1990. Private Communication. Department of Electrical Engineering and Computer Engineering, Iowa State University, Ames, IA, 50011.

Bernardi, R.T. 1990. *Digital Radiography of high Z materials.* To appear in Review of Progress in Quantitative Nondestructive Evaluation, D.O. Thompson and D.E. Chimenti, ed. vol. 9, Plenum Press, New York, NY.

Beyer, W.H. 1981. *CRC Standard Mathematical Tables. 26th ed.* CRC Press, Boca Raton, FL.

Branham, R.L., 1989. *A program for total (orthogonal) least squares in compact storage mode.* Computers in Physics, 3:42-46.

Brint, A.T. and Brady, M. 1990. *Stereo matching of curves.* Image and Vision Computing, 8:50-56.

Brown, R.A., Xu, J.D. and Basart, J.P. 1990. *Software design and features for an NDE image processing workstation.* In Review of Progress in Quantitative

Nondestructive Evaluation, D.O. Thompson and D.E. Chimenti, ed. 9a:pp, Plenum Press, New York, NY.

Burte, H.M. and Chimenti, D.E. 1987. *Unified life cycle engineering: An emerging design concept.* In Review of Progress in Quantitative Nondestructive Evaluation, D.O. Thompson and D.E. Chimenti, ed. 6b:1797-1809. Plenum Press, New York, NY.

Day, T. and Muller, J-P. 1989. *Digital elevation model production by stereo-matching spot image-pairs: A comparison of algorithms.* Image and Vision Computing, 7:95-101.

Deans, S.R. 1983. *The Radon Transform and Some of its Applications.* Wiley, New York, NY.

Denton, R.V., Friedlander, B. and Rockmore, A.J. 1979. *Direct Three-dimensional image reconstruction from divergent rays.* IEEE Transactions on Nuclear Science, 26:4695-4703.

Elias, H. and Hyde, D.M. 1983. *A Guide to Practical Stereology.* Karger, New York, NY.

Feldcamp, L.A., Kubinski, D.J. and Jesion, G. 1988. *Application of high magnification to 3-D x-ray computed tomography.* In Review of Progress in Quantitative Nondestructive Evaluation, D.O. Thompson and D.E. Chimenti, ed. 7a:381-388. Plenum Press, New York, NY.

Fuller, W.A. 1987. *Measurement Error Models.* John Wiley & Sons, New York, NY.

Gellert, W., Küstner, H., Hellwich, M. and Kästner, H. 1975. *The VNR Concise Encyclopedia of Mathematics.* Van Nostrand Reinhold, New York, NY.

Gerald, C.F. and Wheatley, P.O. 1984. *Applied Numerical Analysis - Third Edition.* Addison-Wesley, Reading, MA.

Golub, G.H. and Van Loan, C.F. 1979. *Total least squares.* In Smoothing Techniques for Curve Estimation, T. Gasser and M. Rosenblatt, ed., pp 69-96. Springer-Verlag, New York, NY.

Golub, G.H. and Van Loan, C.F. 1980. *An analysis of the total least squares problem.* SIAM Journal of Numerical Analysis, 17:883-893.

Golub, G.H. and Van Loan, C.F. 1989. *Matrix Computations. 2nd ed.* Johns Hopkins University Press, Baltimore, MD.

Gray, J.N. and Inanc, F. 1989. *Three dimensional modeling of projection radiography.* In Review of Progress in Quantitative Nondestructive Evaluation, D.O. Thompson and D.E. Chimenti, ed. 8a:345-350. Plenum Press, New York, NY.

Grimson, W.E. 1981. *From Images to Surfaces.* The MIT Press, Cambridge, MA.

Hack, R.L., Archilpley-Smith, D.K. and Pfeifer, W.H. 1987. *Engineering tomography: a quantitative NDE tool.* In Review of Progress in Quantitative Nondestructive Evaluation, D.O. Thompson and D.E. Chimenti, ed. 6a:401-410. Plenum Press, New York, NY.

Halmshaw, R. 1982. *Industrial Radiology, Theory and Practice.* Applied Science Publishers, Englewood Cliffs, NJ.

Halmshaw, R. 1987. *Non-destructive Testing.* Edward Arnold (Publishers) Ltd., London.

Hanson, K.M. and Wecksung, G.W. 1983. *Bayesian approach to limited-angle reconstuction in computer tomography.* Journal of the Optical Society of America, 73:1501-1509.

Hung, C.K., Chiou, R.N., Shyi, C.N., Lee, J.Y. and Chen, C.H. 1989. *Polyhedron reconstruction using three-view analysis.* Pattern Recognition, 22:231-246.

Kak, A.C. and Slaney, M. 1988. *Principles of Computerized Tomographic Imaging.* IEEE Press, New York, NY.

Kreyszig, E. 1983. *Advanced Engineering Mathematics. 5th ed.* John Wiley and Sons, New York, NY.

Kuan, D.T., Sawchuk, A.A., Strand, T.C. and Chavel, P. 1985. *Adaptive noise-smoothing filter for images with signal-dependent noise.* IEEE Transactions on Pattern Analysis and Machine Intelligence, 7:165-177.

Kudo, H. and Saito, T. 1988. *A tomographic image reconstruction from limited view angle projection data.* Systems and Computers in Japan, 19:56-64.

Macovski, A. 1983. *Medical Imaging Systems.* Prentice-Hall, Englewood Cliffs, NJ.

Marquardt, D.W. 1963. *An algorithm for least squares estimation of nonlinear parameters.* Journal for the Society of Industrial and Applied Mathematics, 11:431-441.

Marr, D., and Poggio, T. 1979. *A computational theory of human stereo vision.* Proceedings of the Royal Society of London, 204:301-328.

McCullough, E.C., Baker, H.L., Houser, O.W. and Reese, D.F. 1974. *An evaluation of the quantitative and radiation features of a scanning x-ray transverse axial tomograph: The EMI scanner.* Radiation Physics, 3:709-715.

McCullough, E.C. 1975. *Photon attenuation in computed tomography.* Medical Physics, 2:307-320.

Mendioni, G. and Nevatia, R. 1985. *Segment-based stereo matching.* Computer Vision, Graphics, and Image Processing, 31:2-18.

Nalcioglu, O. and Cho, Z.H. 1978. *Reconstruction of 3-D objects from cone-beam projections.* Proceedings of the IEEE, 66:1584-1585.

Nondestructive Testing Handbook - Radiography and radiation testing. 1985. P. McIntire ed. American Society for Nondestructive Testing, Columbus, OH.

Oden, B., Bellman, S. and Fries, B. 1958. *Stereo-micro-lymphangiography.* British Journal of Radiology, 31:70-80.

Pankratz, A. 1983. *Forecasting with Univariate Box-Jenkins Models - Concepts and Cases.* John Wiley & Sons, New York, NY.

Park, K.H. and Park, S.B. 1987. *Maximum entropy image reconstruction for an object with opaque obstructions.* IEEE Transactions on Medical Imaging, 6:308-312.

Peng,H. and Stark, H. 1987. *Direct Fourier Reconstruction in fan-beam tomography.* IEEE Transactions on Medical Imaging, 6:209-219.

Pong, T.C., Haralick, R.M. and Shapiro, L.G. 1989. *Matching topographic structures in stereo vision.* Pattern Recognition Letters, 9:127-136.

Press, W.H., Flannery, B.P., Teukolsky, S.A. and Vetterling, W.T. 1988. *Numerical Recipes in C - The Art of Scientific Computing.* Cambridge University Press, New York, NY.

Reimers, P. and Goebbels, J. 1983. *New possibilities of nondestructive evaluation by computed tomography.* Materials Evaluation, 41:732-737.

Russ, J.C. 1986. *Practical Stereology.* Plenum Press, New York, NY.

Sabbagh, L.D. and Sabbagh, H.A. 1983. *Development of a system to invert eddy current data and reconstruct flaws.* In Review of Progress in Quantitative Nondestructive Evaluation, D.O. Thompson and D.E. Chimenti, ed. 2b:1555-1571. Plenum Press, New York, NY.

Sabbagh, H.A. and Sabbagh, L.D. 1984. *Experimental verification of an inverse algorithm for flaw characterization using eddy currents.* In Review of Progress in Quantitative Nondestructive Evaluation, D.O. Thompson and D.E. Chimenti, ed. 3a:615-620. Plenum Press, New York, NY.

Safaeinili, A., Basart, J.P. and Hung, H.S. 1991. *Reconstructing low contrast flaws in limited-view-angle industrial tomograms using prototype flawless images.* Submitted to the Twenty-Fourth Asilomar Conference on Signals, Systems and Computers, Ray Chen, ed. Maple Press, San Jose, CA.

Saxl, I. 1989. *Stereology of Objects with Internal Structure.* Elsevier, New York, NY.

Stern, B.E., and Lewis, D. 1970. *X-Rays.* Pitman Publishing Corp., New York, NY.

Schmerr, L.W., Chiou, C.P. and Sedov, A. 1988. *Equivalent flaw sizing: A unified approach.* In Review of Progress in Quantitative Nondestructive Evaluation, D.O. Thompson and D.E. Chimenti, ed. 7a:453-459. Plenum Press, New York, NY.

Tam, K.C. 1989. *The application of convex hull in industrial computerized tomography.* In Review of Progress in Quantitative Nondestructive Evaluation, D.O. Thompson and D.E. Chimenti, ed. 8a:389-398. Plenum Press, New York, NY.

Tam, K.C., Eberhard, J.W. and Mitchell, K.W. 1989. *Incomplete-data image reconstructions in industrial x-ray computerized tomography.* In Review of Progress in Quantitative Nondestructive Evaluation, D.O. Thompson and D.E. Chimenti, ed. 8a:407-414. Plenum Press, New York, NY.

Vannier, M.W. and Ellingson, W. A. 1988. *Quantitative computed toomography.* In Review of Progress in Quantitative Nondestructive Evaluation, D.O.

Thompson and D.E. Chimenti, ed. 7a:373-380. Plenum Press, New York, NY.

Wadley, H.N.G., Simmons, J.A. and Turner C. 1984. *Predictive modeling of quantitative acoustic emission waveforms.* In Review of Progress in Quantitative Nondestructive Evaluation, D.O. Thompson and D.E. Chimenti, ed. 3b:683-697. Plenum Press, New York, NY.

Wallingford, R.M. and Basart, J.P. 1988. *3-D crack reconstruction in radiographic images using projections obtained from a linear sample shift.* In Conference Record of the Twenty-Second Asilomar Conference on Signals, Systems and Computers, Ray Chen, ed. 1:68-72. Maple Press, San Jose, CA.

Wallingford, R.M. and Basart, J.P. 1989a. *Flaw geometry reconstruction using a limited set of x-ray radiographic projections* . In Review of Progress in Quantitative Nondestructive Evaluation, D.O. Thompson and D.E. Chimenti, ed. 8a:351-358. Plenum Press, New York, NY.

Wallingford, R.M. and Basart, J.P. 1989b. *Model-based volumetric flaw reconstruction from a limited number of radiographic projections* . In Conference Record of the Twenty-Third Asilomar Conference on Signals, Systems and Computers, Ray Chen, ed. 1:522-525. Maple Press, San Jose, CA.

Wallingford, R.M. and Basart, J.P. 1990. *Model-based flaw reconstruction and flaw parameter estimation using a limited set of radiographic projections.* In Review of Progress in Quantitative Nondestructive Evaluation, D.O. Thompson and D.E. Chimenti, ed. 9a:700-707. Plenum Press, New York, NY.

Weinshall, D., 1990. *Qualitative depth from stereo, with applications.* Computer Vision, Graphics, and Image Processing, 49:222-241.

Young, H.D. 1962. *Statistical Treatment of Experimental Data.* McGraw-Hill, New York, NY.